Search for heavy Majorana neutrinos in pp collisions at $\sqrt{s} = 8$ TeV with the ATLAS detector

Joel Klinger

Particle Physics Group
School of Physics and Astronomy
University of Manchester

A thesis submitted to the University of Manchester for the degree of Doctor of Philosophy in the Faculty of Engineering and Physical Sciences

· 2014 ·

Contents

Search for heavy Majorana neutrinos in pp collisions at $\sqrt{s} = 8$ TeV with the ATLAS detector

Joel Klinger

Particle Physics Group
School of Physics and Astronomy
University of Manchester

A thesis submitted to the University of Manchester for the degree of Doctor of Philosophy in the Faculty of Engineering and Physical Sciences

· 2014 ·

Abstract

The discovery of non-zero neutrino masses has introduced a new mass scale into the Standard Model of particle physics that is at least six orders of magnitude below the electron mass. In the absence of a Standard Model mechanism that can explain the origin of the neutrino mass scale, one can consider the possibility that neutrinos are Majorana fermions which would allow right-handed neutrinos to acquire an additional mass term without requiring new interactions. A mixing of the neutrino Majorana mass terms and Standard Model Dirac mass terms generates mass eigenstates corresponding to light neutrinos, which have already been observed, and heavy neutrinos, which have not. This thesis presents a search for same-sign lepton pairs from the decay of heavy Majorana neutrinos produced in $\sqrt{s} = 8$ TeV proton-proton collisions in the ATLAS detector at the CERN Large Hadron Collider, using data corresponding to an integrated luminosity of 20.3 fb^{-1}. No excess of events above the expected background is observed and 95% confidence level upper limits are set on the cross-section times branching ratio with respect to heavy Majorana neutrino masses in the range 100 to 500 GeV. The presented limits are the most stringent direct limits set to date for heavy neutrino masses greater than 100 GeV.

Declaration

No portion of the work referred to in the thesis has been submitted in support of an application for another degree or qualification of this or any other university or other institute of learning.

Copyright statement

'I didn't say I was rich, I said I'd spent a whole lot of money.'
Howling Wolf

Acknowledgments

I would like to thank my supervisor Un-ki Yang for his insightful advice during my PhD. I owe a great deal of thanks to Mark Owen who has supported me for the past few years in everything from simple programming problems to complex analysis studies and my further career. I am grateful to Fred Loebinger for agreeing to supervise me for the final stretch of my PhD and particularly for providing detailed feedback on this thesis and also for being a constant source of advice and coffee-time chat throughout the last few years. I would also like to thank John Almond for helping me to decipher ATLAS jargon and set up the framework which I continued to use after his departure.

I am very grateful for all of the friends that I have made during my PhD, particularly of my girlfriend Laura whose work ethic and loving support have been a positive influence in my life. A mention too for Jon Harrison with whom I have spent some significant time procrastinating by writing a pub quiz, auditioning for Bargain Hunt and running 100 km from Manchester to Sheffield.

I would like to thank my parents and family for their support throughout my academic career. I am almost literally indebted to my brother Dan Klinger, without whose financial support during my undergraduate degree I would certainly have not made it this far.

Finally I dedicate this thesis to my brother Oliver Simcoe-Shelton who sadly passed away during my PhD but whose positive and optimistic spirit continues to be an inspiration to me.

Chapter 1

Introduction

The most widely accepted theory of fundamental interactions is the Standard Model of particle physics (SM) which provides an understanding of the origins of particles and interactions through fundamental symmetries in nature. Although the SM provides a mechanism for mass generation via interaction with the Higgs field, there is currently no explanation for the observed variance of particle masses generated in this way. For example the Higgs mechanism offers no satisfactory explanation for the disparity between the mass of the top-quark (~ 172 GeV) and the electron (~ 0.5 MeV) which spans nearly six orders of magnitude. The discovery of neutrino oscillations in 1998 [1, 2] implied that neutrinos have non-zero masses despite the best measurements of neutrino masses showing that they are below the current experimental resolution. This introduces a new mass scale between the electron mass and the neutrino mass which is at least of the same order of the scale between the electron and top-quark.

As right-handed neutrinos carry no charge it may be shown that if neutrinos are their own anti-particles, so-called Majorana neutrinos, that they may acquire a 'Majorana mass' independently of the 'Dirac mass' generated by the Higgs mechanism. Consequently the observed neutrino mass scale could be generated in a mechanism which mixes the Dirac and Majorana mass terms such that states of the familiar light neutrinos and additional heavy neutrinos are generated. In order to produce light neutrinos with a mass that is consistent with experimental observation one would require Majorana masses,

which are theoretically unrestricted, to be many orders of magnitude above the Dirac mass scale. The corresponding heavy neutrinos in this scenario would be so massive as to be beyond modern experimental reach.

Another procedure for inducing light neutrino masses is through radiative corrections involving a heavy Majorana neutrino. This mechanism is sufficient to explain light neutrino masses, even for a zero Dirac mass. The scale of the light-neutrino masses in this framework is independent of the Majorana mass scale, but depends solely on the difference in the Majorana masses of neutrino species. This means that heavy neutrino masses may be arbitrarily low, although strong experimental limits are already in place for masses $\lesssim 100$ GeV.

This thesis presents a search for heavy Majorana neutrinos produced in $\sqrt{s} = 8$ TeV proton-proton collisions with data collected by the ATLAS detector at Large Hadron Collider (LHC). In this environment a precise understanding of the ATLAS detector and SM processes are crucial to the sensitivity of the search and so this will guide the discussion of this analysis.

1.1 Units

This thesis uses the system of 'natural units' such that:

$$\hbar = c = 1$$

which leads to the relationship between the units of the following quantities, which will be expressed in terms of eV:

$$[\text{energy}] = [\text{momentum}] = [\text{mass}] = [\text{length}]^{-1} = [\text{time}]^{-1}.$$

Units of electric charge will be given in terms of the magnitude of the electron charge $|e|$.

Chapter 2

The Standard Model of particle physics

The Standard Model of particle physics is a chiral Quantum Field Theory (QFT) whose fields transform under a $U(1) \times SU(2) \times SU(3)$ symmetry. The symmetries of the Standard Model give rise to a consistent picture of the fundamental forces (excluding gravity), namely the Electromagnetic (EM), Weak and Strong nuclear forces. SM interactions between particles of matter are mediated by boson exchange - such that momentum is transferred in discrete quanta that preserve causality. A summary of the interaction strength and range of the SM fundamental forces is given in Table 2.1.

Interaction	Range	Relative strength
Strong	1 fm	1
EM	∞	10^{-2}
Weak	$(M_W)^{-1}$	10^{-6}
Gravity	∞	10^{-37}

Table 2.1: A summary of the interaction strengths and ranges of the SM fundamental forces, and gravity which is not described in the SM. M_W is the mass of the $W^{\pm}$ boson.

As a QFT, the notion of individual static interacting particles is abandoned in favour of dynamic interacting fields of which the quanta are interpreted as particles. This framework is required to reconcile the dynamics of fermions

($\frac{1}{2}$-integer spin particles) in the Dirac equation and bosons (integer-spin particles) in the Klein-Gordon equation if one wants to avoid 'negative energy' solutions and violation of causality. Fundamentally these scenarios are solved in a QFT by introducing anti-particle states such that the propagation of a particle between two space-time points is indistinguishable from the propagation of it's anti-particle along the same path, but in the opposite direction [3] (Figure 2.1).

Figure 2.1: Equivalence of particle and anti-particle dynamics, represented by an electron e^- and anti-electron e^+ traversing between space-time points • and ■.

A fundamental principle of particle physics is symmetry. By imposing symmetry principles in a QFT one gets a space of states in which each state is labelled by a quantum number. Furthermore constructing a theory in this way allows all possible physical states to be classified by quantum numbers.

The Poincaré symmetry introduces quantum numbers associated with four-momentum conservation and also spin (or helicity for massless states), which is associated with conserving angular momentum. Due to the spin-statistics theorem all SM particles are either spin-$\frac{1}{2}$ fermions or integer-spin bosons. Fermions are subdivided into quarks and leptons. Quarks have Baryon quantum number ($B = \frac{1}{3}$) as well as discrete charges associated with the EM and Weak Nuclear interactions, which correspond to a chiral $U(1) \times SU(2)$ symmetry, and the Strong Nuclear interaction, which is described by an $SU(3)$ symmetry. Leptons have Lepton quantum number ($L = 1$) as well as charges associated with the EM and Weak interactions. The B and L symmetries originate from a global charge-conserving symmetry such that $B - L$ is a conserved quantity in the SM. Crucially, interactions arise in the SM by enforcing gauge symmetries:

$$\Psi \rightarrow \Psi' = e^{-i\alpha^a T^a}\Psi$$

that preserve the Lagrangian density of a field Ψ where T^a are the generators of the gauge group and α^a are arbitrary parameters that can be interpreted as the coupling strength of the interaction.

Three generations of fermions are identified in the Electroweak (EW) interaction, where each generation consists of one pair of quarks (up-down) and one pair of leptons (lepton-neutrino) and with interactions mediated by the $W^{\pm}$, Z and γ bosons. The W and Z bosons only interact with left-handed fermions (or right-handed anti-fermions) and the γ boson interacts with particles with EM charge. Masses of the fermions and EW gauge bosons are generated by interactions with the H boson. Neutrinos are explicitly massless in the SM construction and therefore only form left-handed states. In Quantum Chromodynamics (QCD) interactions, which are mediated by eight independent gluon species, each of the six quarks identified in the EW interaction are manifested in three orthogonal 'colour' states. A summary of SM particles is presented in Table 2.2.

			Mass Generation		
Fermion	**I_3**	**Q**	1	2	3
Quarks ($B = \frac{1}{3}$)	$\uparrow$	+2/3	$u_L^{R,G,B}$	$c_L^{R,G,B}$	$t_L^{R,G,B}$
	0	+2/3	$u_R^{R,G,B}$	$c_R^{R,G,B}$	$t_R^{R,G,B}$
	0	-1/3	$d_R^{R,G,B}$	$s_R^{R,G,B}$	$b_R^{R,G,B}$
	$\downarrow$	-1/3	$d_L^{R,G,B}$	$s_L^{R,G,B}$	$b_L^{R,G,B}$
Leptons ($L = 1$)	$\uparrow$	-1	e_L	μ_L	τ_L
	0	-1	e_R	μ_R	τ_R
	$\downarrow$	0	ν_L^e	ν_L^μ	ν_L^τ

Bosons
γ
$W^{\pm}$
Z
$g^{i=1...8}$
H

+ anti-particles

Table 2.2: Summary of particles in the SM. The values of Isospin (I_3) describe the 'up' ($\uparrow$) and 'down' ($\downarrow$) states of particles that interact with the EW bosons. $\{R, G, B\}$ refer to the three orthogonal 'colour' states of quarks in QCD.

2.1 Fermions and the EW interaction

The Electroweak (EW) interaction transforms fields under a $U(1) \times SU(2)$ symmetry. The SM $U(1)$ gauge symmetry describes the EM force as a complex phase change mediated by B^0 boson exchange for particles with EM charge Q or Weak isospin I_3. The SM $SU(2)$ group is the lowest-dimension symmetry group under which fields that transform under the fundamental representation (fermions) may exist in one of two distinct states, fields that transform under the adjoint representation (vector bosons) may exist in one of three distinct states, whilst transitions between states preserve probability. The allowed fermionic states in $SU(2)$, J_i can be expressed in terms of the Pauli matrices σ_i:

$$J_i = \tfrac{1}{2}\sigma_i \qquad \text{with} \quad i = 1, 2, 3 \tag{2.1}$$

where the Pauli matrices are defined as:

$$\sigma_1 = \begin{pmatrix} 0 & 1 \\ 1 & 0 \end{pmatrix}, \qquad \sigma_2 = \begin{pmatrix} 0 & -i \\ i & 0 \end{pmatrix}, \qquad \sigma_3 = \begin{pmatrix} 1 & 0 \\ 0 & -1 \end{pmatrix}.$$

It is conventional to choose the eigenvectors of σ_3 to represent the $SU(2)$ fermion states. Doing so we define two isospin (I_3) states, up ($\uparrow$) and down ($\downarrow$), as the eigenvalues in this representation:

$$\begin{aligned} \uparrow \quad &\equiv \quad I_3 = \tfrac{1}{2} \begin{pmatrix} 1 \\ 0 \end{pmatrix} \sigma_3 \\ \downarrow \quad &\equiv \quad I_3 = \tfrac{1}{2} \begin{pmatrix} 0 \\ 1 \end{pmatrix} \sigma_3. \end{aligned} \tag{2.2}$$

Fermions that transform in this framework form isospin pairs (Dirac spinors) with possible states according to $I_3 = \pm\frac{1}{2}$. There are two categories of fermions in the SM framework, quarks and leptons. Quarks exist in up-down I_3 pairs $(q^{\uparrow}, q^{\downarrow})$ and leptons exist in lepton-neutrino I_3 pairs $(l^{\uparrow}, \nu_l^{\downarrow})$. The corresponding electric charge of quark and lepton spinors is given by

$Q(q) = (+\frac{2}{3}, -\frac{1}{3})$ and $Q(l) = (-1, 0)$ respectively. Transitions (or decays) between up-down quark states or l-ν lepton states are mediated by $W^{\pm}$ bosons, which by inspection must have $I_3 = \pm 1$ and $Q = \pm 1$ in order to conserve charge. The $W^{\pm}$ are two components of an I_3 triplet which transforms under the SM $SU(2)$ gauge symmetry. The third component of the triplet is the W^0 boson, which has $Q = 0$ and $I_3 = 0$.

The EW interaction is constructed such that fermions are distinct from their anti-particles, and that EW interactions are invariant for fermion fields Ψ and anti-fermion fields $\bar{\Psi}$ under a $\widehat{CP}$ transformation:

$$\widehat{CP}\ \Psi_L = \bar{\Psi}_R \tag{2.3}$$

$$\widehat{CP}\ \Psi_R = \bar{\Psi}_L \tag{2.4}$$

where $\widehat{CP} \equiv \widehat{C}\widehat{P}$ and the operators $\widehat{C}$ and $\widehat{P}$ are defined as follows:

- $\widehat{C}$ is the charge-conjugation operator, which reverses all the 'internal' quantum numbers of a particle, such as electric charge,
- $\widehat{P}$ is the parity operator, which reverses space coordinates such that left-handed particles become right-handed and vice-versa.

The weak interaction has been measured to only couple to left-handed particles (and right-handed anti-particles) so the SM $SU(2)$ symmetry is constructed as a left-handed symmetry $SU(2)_L$ to reflect this (i.e. right-handed particles are $SU(2)_L$ singlets with $I_3 = 0$). In the $SU(2)_L$ group, left-handed fermion fields Ψ_L rotate as a local gauge transformation:

$$\Psi_L \rightarrow \Psi_L{}' = e^{-\frac{i}{2}\boldsymbol{\sigma}}\Psi_L. \tag{2.5}$$

The B^0 boson of the $U(1)$ symmetry has $Q = 0$ and $I_3 = 0$ but, unlike the W^0, mediates force between hypercharge, $Y = 2(Q - I_3)$. In the $U(1)_Y$ group, fermion fields Ψ with $Y \neq 0$ rotate as a local phase transformation:

$$\Psi \rightarrow \Psi' = e^{-i\omega(x)Y}\Psi. \tag{2.6}$$

The EW Lagrangian L_{EW} is invariant under such rotations presented in

Equations 2.5 and 2.6:

$$\begin{aligned}\mathcal{L}_{\mathrm{EW}} = &-\tfrac{1}{4}\boldsymbol{W_{\mu\nu}}\cdot\boldsymbol{W^{\mu\nu}} - \tfrac{1}{4}B_{\mu\nu}B^{\mu\nu} \\ &+\bar{\Psi}_L\gamma^\mu\left(i\partial_\mu - g\tfrac{1}{2}\boldsymbol{\sigma}\cdot\boldsymbol{W_\mu} - g'\tfrac{1}{2}YB_\mu\right)\Psi_L \\ &+\bar{\Psi}_R\gamma^\mu\left(i\partial_\mu - g'\tfrac{1}{2}YB_\mu\right)\Psi_R \end{aligned} \tag{2.7}$$

where $\boldsymbol{W}$ are the Weak boson fields, B is the EM field, $\Psi_{L(R)}$ are left(right)-handed fermion fields and $g(g')$ are the fermion-gauge boson couplings. The neutral states W^0 and B^0 mix to form states Z and γ, where γ is identified as the massless photon of the EM interaction [4]. The W and Z bosons are massive particles, with masses of approximately 83.0 GeV and 93.8 GeV respectively. They were discovered in 1982 and 1983 by the UA1 and UA2 collaborations [5].

Three 'mass generations' of quarks and leptons have been discovered corresponding to I_3 doublets (and corresponding right-handed singlets) of increasing mass but otherwise identical quantum numbers. Each ↑-type and ↓-type quark and lepton state is assigned a 'flavour' in Table 2.3. Transitions between I_3 states can still occur across generations through W boson exchange, as the observed quark (or lepton) flavour states are formed through mixing fundamental quark (or lepton) mass states, in an analogous way to W^0/B^0 mixing. Quark mixing is described by the Cabibbo-Kobayashi-Maskawa (CKM) matrix [6, 7] and lepton mixing is described by the Pontecorvo-Maki-Nakagawa-Sakata (PMNS) matrix [8].

	Quark flavour		Lepton flavour	
Generation	↑	↓	↑	↓
1	u (up)	d (down)	e (electron)	ν^e (e-neutrino)
2	c (charm)	s (strange)	μ (muon)	ν^μ (μ-neutrino)
3	t (top)	b (bottom)	τ (tau)	ν^τ (τ-neutrino)

Table 2.3: SM fermion flavours as a function of mass generation and I_3 (↑ or ↓)

In a QFT the probability to observe a specific interaction can only be exactly calculated by considering an infinite series of interfering processes of increasing complexity and decreasing probability. If the interaction coupling is small then SM calculations may be performed in a perturbation theory, in which all of the interfering processes are represented by Feynman diagrams [9]. Measurable cross-sections can be calculated by multiplying Feynman diagrams with their Hermitian conjugate, up to a fixed number of coupling terms. Each set of Feynman diagram-conjugate pairs are referred to as Leading Order (LO) (or 'tree-level') for those with the smallest power n of coupling strength α that make a non-zero contribution to the cross-section. Higher-order terms are referred to as Next-to-Leading Order (NLO) for $n+1$ coupling terms and Next-to-Next-to-Leading Order (NNLO) for $n+2$ couplings etc.

In the Feynman diagrams presented in this thesis fermions are depicted by straight lines traversing space-time with arrows representing the flow of charge (Figure 2.1). Electroweak spin-1 bosons (W, Z and γ) are represented by oscillating lines. Allowed 'interaction vertices' are points on Feynman diagrams where fermion and bosons lines meet such that quantum numbers (charge, spin-states) and kinematics (energy, momentum) are conserved.

2.1.1 Electroweak symmetry breaking

In order to preserve the gauge symmetry of the SM Lagrangian it is necessary that particle masses are acquired by some external mechanism. A potential is introduced in which the ground state modifies the Lagrangian of interacting particles in order to generate particle mass terms. The simplest and lowest order form of such a potential $V(\phi_i)$ is written in terms of a set of real scalar (spin-0) fields $\phi_i(x)$:

$$V(\phi_i) = -\tfrac{1}{2}\mu^2(\phi_i)^2 + \tfrac{1}{4}\lambda[(\phi_i)^2]^2 \tag{2.8}$$

where μ and λ are positive parameters. Crucially, the form of V is such that the ground potential is displaced from the symmetric point ($\phi_i = 0$). The symmetry of the interaction Lagrangian within a symmetric potential

V is hidden by the choice of a ground state and oscillations $h(x)$ about these minima are sufficient to generate mass terms in the Lagrangian. The field $h(x)$ is described as the Higgs field whose corresponding quanta are Higgs bosons H. The interacting field must belong to $SU(2) \times U(1)$ multiplets and must consist of four scalar fields ($\phi_{i=1...4}$) in order to generate the W^+, W^- and Z masses whilst the photon remains massless. The simplest choice for this arrangement is described by an $SU(2)$ doublet:

$$\phi = \begin{pmatrix} \phi^+ \\ \phi^0 \end{pmatrix} \qquad \text{with} \qquad \begin{aligned} \phi^+ &\equiv \tfrac{1}{\sqrt{2}}(\phi_1 + i\phi_2) \\ \phi^0 &\equiv \tfrac{1}{\sqrt{2}}(\phi_3 + i\phi_4). \end{aligned} \tag{2.9}$$

In order to generate masses one must pick a minimum value of ϕ, which is expressed in terms of the vacuum expectation value v:

$$\phi^0 \equiv \tfrac{1}{\sqrt{2}} \begin{pmatrix} 0 \\ v \end{pmatrix}. \tag{2.10}$$

An additional term $L_{EW}^{\text{Boson masses}}$ is added to the EW Lagrangian (Equation 2.7) to incorporate massive gauge bosons as observed in nature:

$$L_{EW}^{\text{Boson masses}} = \left| \left(i\partial_\mu - g\tfrac{1}{2}\boldsymbol{\sigma} \cdot \boldsymbol{W_\mu} - g'\tfrac{1}{2} Y B_\mu \right) \phi \right|^2 - V(\phi). \tag{2.11}$$

Fermionic mass terms m_f are also generated by interaction with the Higgs field (except for neutrinos), with couplings to H given by the Yukawa couplings Y_f for fermion f (Equation 2.12) which requires a corresponding term $L_{EW}^{\text{Fermion masses}}$ to be added to the EW Lagrangian:

$$m_f = \frac{Y_f v}{\sqrt{2}} \tag{2.12}$$

$$L_{EW}^{\text{Fermion masses}} = -\left(Y_\uparrow \bar{\Psi}_L \phi \Psi_R + Y_\downarrow \bar{\Psi}_L \phi_c \Psi_R \right). \tag{2.13}$$

Although this mechanism describes the origin of fermion masses, it does not offer an insight into their relative size which span nearly six orders of magnitude from the electron mass at $m_e \approx 0.5$ MeV to the top quark mass at $m_t \approx 172$ GeV. Neutrinos are explicitly massless in the SM such that $Y_\nu = 0$. Since the construction of the SM it has been discovered that neutrinos have

non-zero masses which are below current experimental resolution [1, 2, 10]. In principle one can simply introduce Yukawa couplings for the neutrinos, although this would imply the existence of right-handed neutrinos, which have not been observed. Furthermore this provides no motivation for the neutrino mass scale which is at least a further six orders of magnitude below the electron mass (Figure 2.2). There are mechanisms that can generate light neutrino masses which also require the SM to be extended to include new particles. This will be discussed in Chapter 3.

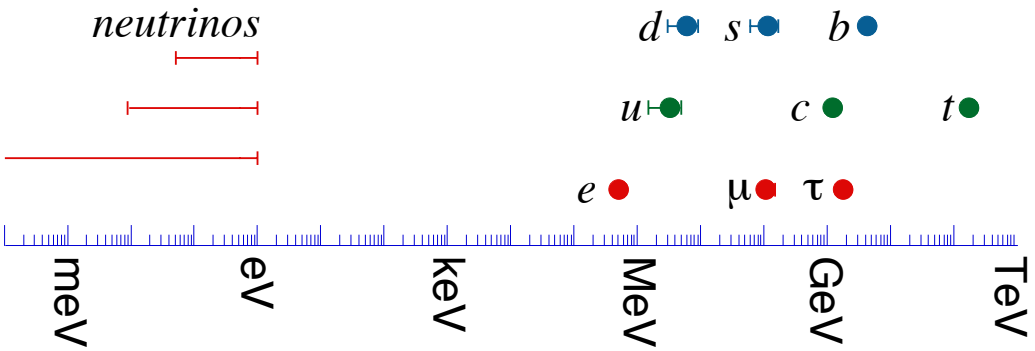

Figure 2.2: Masses of the fermions [11].

2.2 Hadrons and Quantum Chromodynamics

QCD describes the interactions of fields transforming in a $SU(3)_C$ symmetry under the influence of colour charge C. The gauge invariant Lagrangian that describes fermion fields Ψ in this group is given by $\mathcal{L}_{\mathrm{QCD}}$:

$$\begin{aligned} \mathcal{L}_{\mathrm{QCD}} &= \bar{\Psi}(i\gamma^\mu D_\mu)\Psi - \tfrac{1}{4}G^a_{\mu\nu}G^{a\mu\nu} \\ \text{where} \quad D_\mu &= \partial_\mu \mathbf{I} + ig_s T^a G^a_\mu \end{aligned}$$

and G^a are the Gell-Mann matrices that describe the gauge fields of QCD, $\mathbf{I}$ is the unit matrix and g_s is the coupling strength of the interaction. The gauge fields of QCD are physically manifested as gluon bosons. The $SU(3)_C$ group is the lowest-dimension symmetry group under which fields in the fundamental representation (quarks) may exist in one of three distinct colour states whilst transitions between states preserve unitarity. The base states of $SU(3)$ (R, G, B) are defined as the eigenvectors of the eight 3×3 Gell-Mann matrices that describe the possible rotations of quark states in QCD:

$$R = \begin{pmatrix} 1 \\ 0 \\ 0 \end{pmatrix}, \qquad G = \begin{pmatrix} 0 \\ 1 \\ 0 \end{pmatrix}, \qquad B = \begin{pmatrix} 0 \\ 0 \\ 1 \end{pmatrix} \tag{2.14}$$

In this way quarks may exist in one of three colour states (R, G, B) and each anti-quark may exist in one of three anti-colour states ($\bar{R}$, $\bar{G}$, $\bar{B}$). Transitions between colour states are mediated by the exchange of gluons, which are also colour-charged particles. The charge configurations of the eight gluons correspond to each of the Gell-Mann matrices in the following representation:

$$\begin{aligned} &(R\bar{B} + B\bar{R})/\sqrt{2} && -i(R\bar{B} - B\bar{R})/\sqrt{2} \\ &(R\bar{G} + G\bar{R})/\sqrt{2} && -i(R\bar{G} - G\bar{R})/\sqrt{2} \\ &(B\bar{G} + G\bar{B})/\sqrt{2} && -i(B\bar{G} - G\bar{B})/\sqrt{2} \\ &(R\bar{R} - B\bar{B})/\sqrt{2} && (R\bar{R} + B\bar{B} - 2G\bar{G})/\sqrt{6}. \end{aligned}$$

It is observed experimentally that 'coloured' objects do not appear in nature beyond a distance of $\sim$ 1 fm. This property is known as confinement. It

follows from this that only composite QCD objects in colour-neutral states, called hadrons, can be observed experimentally. Hadrons are categorised into baryons, which consist of three fermions with an RGB colour structure, and mesons, which consist of two fermions with a $R\bar{R}$, $G\bar{G}$ or $B\bar{B}$ colour structure. Examples of light hadrons are protons (p), neutrons (n) and pions (π^0, $\pi^\pm$) which have the following quark structure:

$$\begin{aligned} p &= uud \\ n &= udd \\ \left(\pi^0, \pi^+, \pi^-\right) &= \left(\tfrac{1}{\sqrt{2}}(u\bar{u} - d\bar{d}), u\bar{d}, d\bar{u}\right). \end{aligned}$$

The dynamics of partons, which collectively refer to gluons and quarks within a proton, are used to described the initial state of proton-proton collisions. The momentum distribution of a parton within a proton is described by a Parton Distribution Function (PDF) [12–15], $f(x, \mu^2)$, where x is the proton's momentum fraction carried by the parton and μ is an energy scale. PDF information is extracted from data which for this thesis is taken from fits by the CTEQ collaboration [12].

Cross-sections $\sigma_{pp\to X}$ for proton-proton collisions that lead to an arbitrary final state X can be calculated by considering the soft sub-proton physics and hard scatter processes to be separated at an energy (or 'factorisation') scale μ_F. The calculation of $\sigma_{pp\to X}$ is performed in terms of protons p_A and p_B with momentum transfer Q:

$$d\sigma_{p_A,p_B,Q^2} = \sum_{a,b} \int_0^1 dx_a f_a^A(x_a, \mu_F^2) \int_0^1 dx_b f_b^B(x_b, \mu_F^2) d\hat{\sigma}_{ab\to X}. \quad (2.15)$$

where f is the PDF and $\hat{\sigma}_{ab\to X}$ is the cross-section for the partonic initial state a, b to lead to the final state X.

Chapter 3

Neutrino physics

3.1 Evidence for non-zero neutrino masses

In the SM neutrinos are assumed to be massless particles, although there is no theoretical requirement for this. In the past this formulation was assumed on the basis that neutrino masses are directly measured to be consistent with zero, with the the current best limits (at 90% CL) [10]:

$$m_{\bar{\nu_e}} < 2 \text{ eV}, \quad m_{\nu_e} < 225 \text{ eV}, \quad m_{\nu_\mu} < 0.19 \text{ MeV}, \quad m_{\nu_\tau} < 18.2 \text{ MeV}.$$

In 1998 it was discovered that neutrinos can oscillate between flavour states [1, 2] which implies that the flavour states are a mixture of mass states (Figure 3.1). Experiments that have measured neutrino oscillations are able to evaluate the difference of the mass-squared $\Delta m^2_{\alpha\beta,\alpha\neq\beta}$ of neutrino species ν_α, ν_β due to the relation between the two-species oscillation probability $P_{\alpha\beta}$, mixing angle $\theta_{\alpha\beta}$, oscillation distances L and neutrino energy E:

$$P_{\alpha\to\beta,\alpha\neq\beta} = \sin^2(2\theta_{\alpha\beta}) \sin^2\left(\frac{\Delta m^2_{\alpha\beta} L}{4E}\right)$$

which has resulted in the measurements [10]:

$$\Delta m^2_{21} = 7.50^{+0.19}_{-0.2}\ 10^{-5} \text{ eV}^2, \quad |\Delta m^2_{32}| = 2.32^{+0.12}_{-0.08}\ 10^{-3} \text{ eV}^2.$$

This result offers conclusive evidence that neutrinos have non-zero mass.

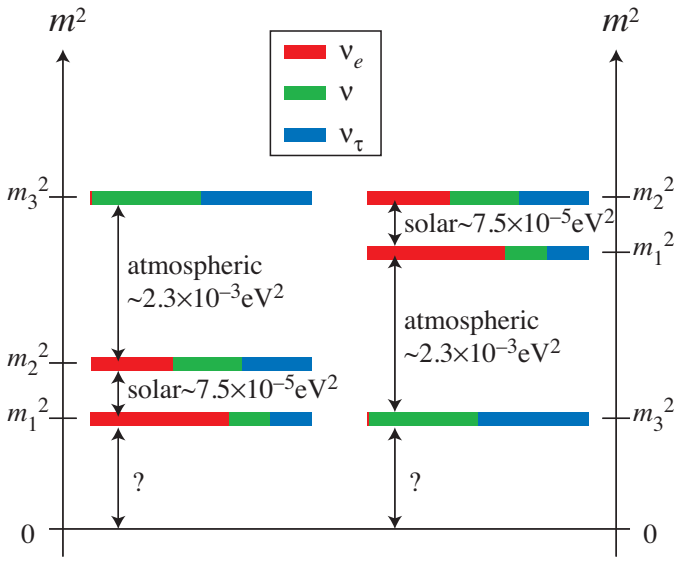

Figure 3.1: Neutrino flavour composition (ν_e, ν_μ, ν_τ) of neutrino mass states with masses (m_1, m_2, m_3). The differences of the mass-squared between the states is presented. The 'solar' and 'atmospheric' mass-squared differences correspond to Δm^2_{21} and Δm^2_{32} respectively. The order of the mass states on the left and right side of the figure are described as the 'Normal' and 'Inverted' hierarchies. These refer to the situation where $\Delta m^2_{32} > 0$ and $\Delta m^2_{32} < 0$ respectively [11].

3.2 Majorana neutrinos

A consequence of the non-zero neutrino mass is the possibility that neutrinos are Majorana fermions, which are indistinguishable from their anti-particles, as opposed to all other Dirac-type fermions which are distinct from their anti-particles. In principle neutrinos should be Majorana in nature if one considers the following argument:

1. Neutrinos are massive fermions and therefore have right-handed components which are $SU(2)_L$ singlets.

2. Neutrinos are electrically neutral leptons therefore their right-handed components are also $U(1)_Y$ singlets.

3. The quantum numbers of SM $SU(2)_L \times U(1)_Y$ lepton singlets are indistinguishable from their anti-particles:

$$\begin{array}{ccc} \nu_R & \equiv & \bar{\nu}_L. \\ (I_3 = 0, Y = 0) & & (I_3 = 0, Y = 0) \end{array} \tag{3.1}$$

Despite this experiments are yet to show that neutrinos are Majorana-type particles. The typical method to test this phenomenon is by searching for evidence of neutrinoless double-beta decay, in which two anti-neutrinos from separate neutron decays annihilate, as illustrated in Figure 3.2. The Majorana nature of neutrinos can also be tested in high energy particle collider experiments by direct production of heavy Majorana neutrinos, which will be discussed in Section 3.7.

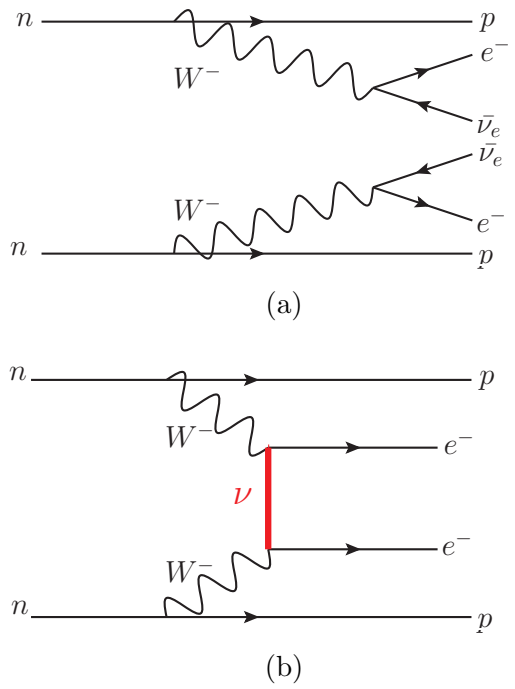

Figure 3.2: Feynman diagrams for the the simultaneous decay of two neutrons ($n = udd$) to two protons ($p = uud$). Figure (a) demonstrates the experimentally observed double beta decay process- resulting in two electrons and two anti-neutrinos in the final state. Figure (b) demonstrates the currently unobserved neutrinoless double beta decay process, which results in two electrons in the final state and the neutrinos have annihilated due to their Majorana nature.

3.3 Neutrino masses and the Type-1 Seesaw Mechanism

Neutrinos in the SM are specifically constructed with zero mass at tree level but this holds to all orders of perturbation theory due the inherent $B - L$ symmetry. This is often referred to as an 'accidental' symmetry as it is not implicit in the SM formulation [16]. If one pursues the necessity for right-handed neutrinos then the neutrinos would be the Majorana-type which explicitly violates L (Figure 3.2b).

A naive introduction of right handed neutrinos ν_R into the SM would only yield an interaction with the Higgs field which requires a Yukawa coupling for each neutrino leading to a Dirac mass:

$$m_D = \frac{Y_\nu v}{\sqrt{2}}$$

where v is the vacuum expectation value of the Higgs field. Although this is an acceptable mechanism for neutrino mass generation, this interaction does not offer an insight into the smallness of the neutrino masses and Yukawa couplings. However, due to the Majorana nature of ν_R, one can additionally introduce a Majorana mass m_R which is free of Yukawa couplings. This does not interfere with gauge symmetries as ν_R states are SM singlets:

$$\tfrac{1}{2} m_R \left(\bar{\nu}_R^C \bar{\nu}_R + \bar{\nu}_R \bar{\nu}_R^C \right) \tag{3.2}$$

where superscript ^{C} indicates charge conjugation. With this in mind the following construction allows the neutrino Yukawa couplings to remain at a 'natural' scale whilst neutrino masses are generated to an order consistent with observation.

Type-1 Seesaw Mechanism

The non-zero neutrino mass offers a potential insight into Beyond the Standard Model (BSM) physics which may provide a mechanism that explains the smallness of neutrino masses. If neutrinos are Majorana particles, then the three-generation matrix of neutrino flavours $\nu = (\nu_L, N_L)$, where

$N_L \equiv (\nu_R)^C$, has a corresponding mass matrix M_ν which contains terms corresponding the Majorana mass matrix M_R in addition to the Dirac mass matrix M_D. The introduction of M_R here is analogous to m_R in Equation 3.2. Hence the matrix M_ν can be written in the basis (ν_L, N_L) in terms of the 3×3 matrices M_D and M_R:

$$M_\nu = \begin{pmatrix} 0 & M_D^T \\ M_D & M_R \end{pmatrix} \tag{3.3}$$

where the zero term indicates that left-handed neutrinos are not endowed Majorana mass terms M_L in this model. Considering the one-flavour case, where the three-generation matrices M_D and M_R are reduced to scalar quantities (denoted by $M \to m$), the diagonalisation of Equation 3.3 yields the mass eigenvalues of ν:

$$m_\nu = \frac{m_R - \sqrt{m_R^2 + 4m_D^2}}{2} \tag{3.4}$$

$$m_N = \frac{m_R + \sqrt{m_R^2 + 4m_D^2}}{2} \tag{3.5}$$

where m_ν corresponds to the mass of the familiar light neutrino and m_N corresponds to a heavy neutrino, which is yet to be discovered. From Equations 3.4 and 3.5 it is evident that as m_N increases m_ν decreases. As such the process is described to as a Type-1 Seesaw Mechanism, where the category 'Type-1' refers specifically to the case of $M_L = 0$. Examining the Seesaw Mechanism for $m_R \gg m_D$:

$$m_\nu \approx -\frac{m_D^2}{m_R}$$
$$m_N \approx m_R.$$

Note that a similar result can be shown in the three-flavour case by diagonalising 3.3 for $M_R \gg M_D$:

$$M_\nu \approx -M_D M_R^{-1} M_D^T$$
$$M_N \approx M_R.$$

Assuming $m_D = m_e$ leads to:

$$m_\nu \ll m_{e,u,d}.$$

Comparing to current experimental limits on light neutrino masses, in order to generate $m_\nu < 1$ eV at tree-level requires that $m_N > 250$ GeV.

3.4 Radiatively induced neutrino masses

As shown in Section 3.3, a Type-1 Seesaw Mechanism can generate light neutrino masses that are consistent with current measurements. Experimentally the caveat for direct heavy neutrino production is that the required collision energy to produce heavy neutrinos is only at the edge of modern capabilities. Furthermore from a theoretical perspective one normally embeds the SM gauge symmetry into a more fundamental theory such as a Left-Right Symmetric Model (LRSM) (Section 3.6) or a Grand Unified Theory (GUT) [17] model which would require new interactions and may raise the energy scale further. Work by A. Pilaftsis in 1991 [18] showed that the masses of light neutrinos ν could be generated by requiring heavy neutrinos N with a mass at the EW scale without requiring new interactions, even for light neutrinos that are massless at the tree level:

$$m_D = \frac{Y_\nu v}{\sqrt{2}} = 0$$

such that the generated light neutrino mass is purely of the Majorana-type. Within this framework it is only the $N - \nu$ interactions via H and Z bosons, shown in Figures 3.3(a,b), that induce a non-zero light neutrino mass. The light neutrino mass-matrix M_ν is given by:

$$\begin{aligned} M_\nu = \quad & [g(m_{N_2}) - g(m_{N_1})] m_{N_2} C_{\nu_i N_2} C_{\nu_j N_2} \\ & + [g(m_{N_3}) - g(m_{N_1})] m_{N_3} C_{\nu_i N_3} C_{\nu_j N_3} \end{aligned} \tag{3.6}$$

where C are the $N - \nu$ couplings and the function g is calculated by considering the interactions in Figure 3.3. Crucially from Equation 3.6 the smallness of the light neutrino masses is reliant on the heavy neutrino mass states being

nearly degenerate, and although the heavy neutrino masses are theoretically unrestricted they may also be arbitrarily small, potentially within reach of modern collider experiments.

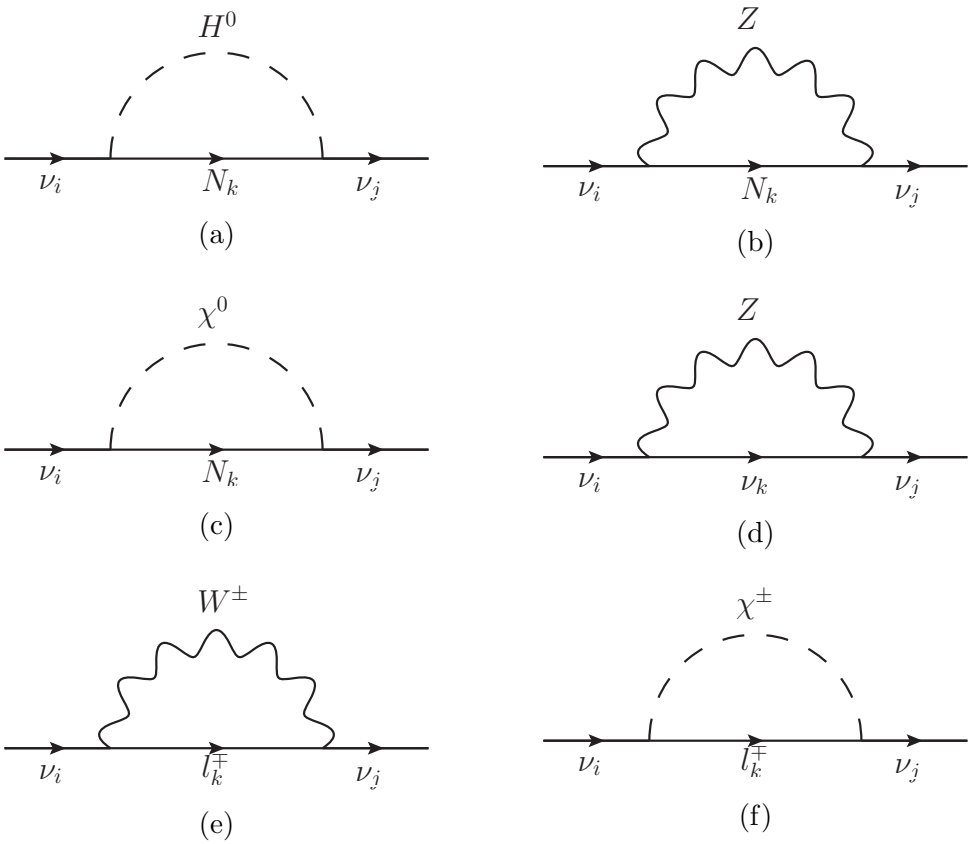

Figure 3.3: Feynman diagrams for interactions responsible for light neutrino mass induction where N are heavy neutrinos. After cancellations, only (a) and (b) contribute. The χ particles are unphysical Goldstone bosons, corresponding to three of the four scalar fields of the Higgs field.

3.5 Heavy neutrino production at a hadron collider

Within the framework of a Type-1 Seesaw Mechanism (Section 3.3) or radiatively induced neutrino masses (Section 3.4) a heavy neutrino may decay via interaction with the Higgs ($N \to \nu H$) or EW bosons ($N \to \nu Z$, $N \to l^{\mp}W^{\pm}$). The branching ratios for these decays are presented in Figure 3.4, with the dominant decay for $m_N < 1$ TeV being $N \to l^{\mp}W^{\pm}$ [19].

The preferred heavy neutrino production mechanism at a pp collider is given by $q\bar{q} \to (W^{\pm})^* \to Nl^{\pm}$, where W^* is an off-shell W boson. As the heavy neutrino is Majorana, lepton number may be violated such that the final state presented in Figure 3.5 may contain pairs of leptons which have electric charge of either opposite-sign (OS) which implies $\Delta L = 0$ or same-sign (SS) with $\Delta L = 2$, in addition to two jets from the W decay. The significance of SS leptons in the final state is that there are relatively few SM processes that will mimic this process due to $B - L$ conservation in SM interactions. The cross-section $\sigma(s)$ for the process $pp \to (W^{\pm})^* \to Nl^{\pm}$ with centre of mass energy $\sqrt{s}$ is calculated according to:

$$\sigma(s) = 2 \int dx \int dy \left[f^p_{\bar{u}}(x, Q^2) f^p_{\bar{d}}(y, Q^2) + f^p_{\bar{c}}(x, Q^2) f^p_{\bar{s}}(y, Q^2) \right] \hat{\sigma}(\hat{s})$$

where f^p_q are the parton distribution functions for quark q at $Q^2 = \hat{s} = xys$, x and y are the momentum fractions of the respective protons carried by the interacting quarks and $\hat{\sigma}(\hat{s})$ is given by:

$$\hat{\sigma}(\hat{s}) = \frac{\pi \alpha_W^2}{72 \hat{s}^2 (\hat{s} - m_W^2)^2} |V_{lN}|^2 (\hat{s} - m_N^2)^2 (2\hat{s} + m_N^2)$$

where α_W is the weak coupling constant, m_W is the W boson mass, m_N is the heavy neutrino mass and V_{Nl} is the heavy neutrino-lepton coupling. In this model V_{Nl} and m_N are the only free parameters. The theoretical cross-section for the heavy-neutrino production process presented in Figure 3.5 is shown in Table 3.1 which assumes a coupling of $|V_{Nl}|^2 = 1$. The cross-section decreases from 3.361 pb to 0.002778 pb in the mass range $100 < m_N$ [GeV] < 500.

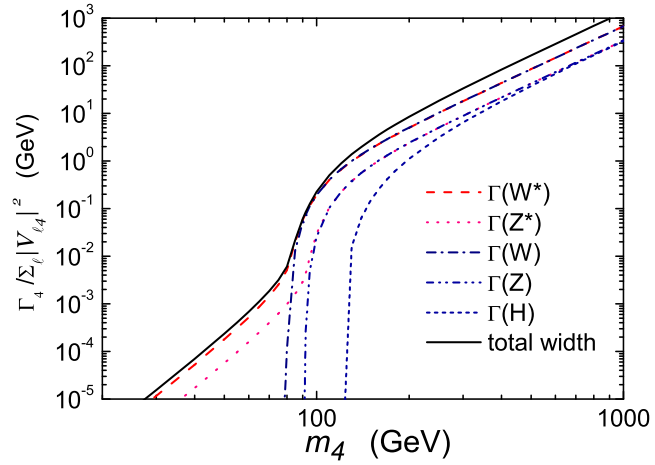

(a)

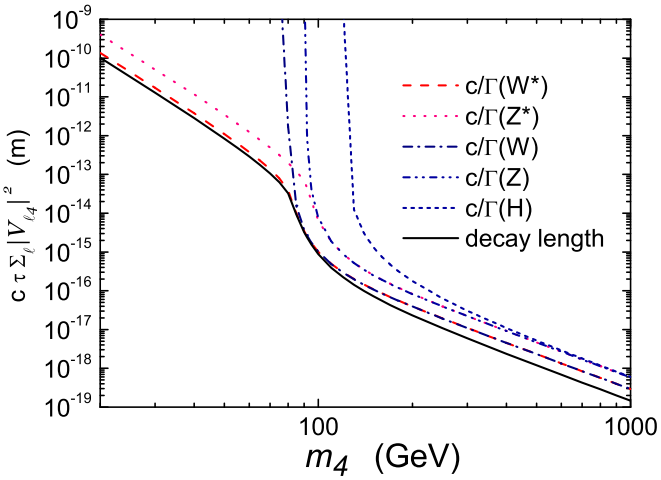

(b)

Figure 3.4: (a) Decay width and (b) decay length of of heavy Majorana neutrinos, denoted by the subscript $_4$, (normalised to coupling V_{4l}) for real and virtual bosons as a function of heavy neutrino mass m_4 [19].

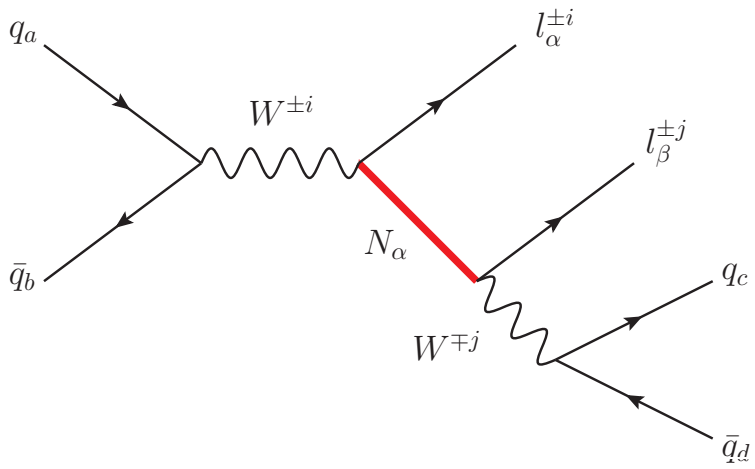

Figure 3.5: Production of a heavy neutrino N_α corresponding to lepton flavour α. The magnitude of the labelled electric charges are $|i| = |j| = 1$. As the neutrino is Majorana both the cases $i = j$ and $i \neq j$ are valid. If lepton flavour (α, β) is conserved $\alpha = \beta$, otherwise $\alpha \neq \beta$. The W produced from the N decay is on-shell and, in this case, decays hadronically.

m_N [GeV]	$\sigma(pp \to N\ell^\pm \to \ell^\pm\ell^\pm jj)$ [pb]
100	$3.361 \quad \pm 1.5 \times 10^{-2}$
110	$1.836 \quad \pm 9.6 \times 10^{-3}$
120	$1.159 \quad \pm 5.0 \times 10^{-3}$
140	$5.575 \times 10^{-1} \pm 2.1 \times 10^{-3}$
160	$3.057 \times 10^{-1} \pm 1.2 \times 10^{-3}$
180	$1.843 \times 10^{-1} \pm 6.4 \times 10^{-4}$
200	$1.180 \times 10^{-1} \pm 4.0 \times 10^{-4}$
240	$5.563 \times 10^{-2} \pm 1.5 \times 10^{-4}$
280	$2.947 \times 10^{-2} \pm 1.0 \times 10^{-4}$
300	$2.225 \times 10^{-2} \pm 8.9 \times 10^{-5}$
400	$6.959 \times 10^{-3} \pm 2.0 \times 10^{-5}$
500	$2.778 \times 10^{-3} \pm 1.1 \times 10^{-5}$

Table 3.1: Theoretical cross-section for process $pp \to N\ell^\pm \to \ell^\pm\ell^\pm jj$ as a function of heavy neutrino mass m_N, where N is a heavy Majorana neutrino, assuming a heavy neutrino-lepton coupling of $|V_{Nl}|^2 = 1$.

3.6 Heavy neutrinos in a Left-Right Symmetric Model

A Left-Right Symmetric Model (LRSM) [20–23] extends the SM Lagrangian to an $SU(3)_C \times SU(2)_L \times SU(2)_R \times U(1)$ symmetry where $SU(2)_R$ is the right-handed analogue of the SM $SU(2)_L$. In this scenario neutrino mass generation involves the introduction of three right-handed neutrino fields and a triplet of Higgs fields (which give rise to doubly-charged physical Higgs boson). Furthermore the $SU(2)_R$ symmetry gives rise to W_R and Z_R gauge bosons.

A search for heavy neutrinos and the right-handed gauge bosons within the LRSM framework was performed in parallel to the presented analysis by collaborators of the author of this thesis. As the decay of W_R and Z_R gauge bosons (Figure 3.6) lead to the same final state particles as in the Type-1 Seesaw Mechanism and the radiatively induced mass scenario, there has been an effort to share the analysis procedure and background estimates where it is possible, which is particularly reflected in Chapters 9 - 11.

It should be noted that the kinematics from LRSM decays differ greatly to those from a Type-1 Seesaw Mechanism heavy neutrino, requiring separate optimisation and signal understanding. This is mainly due to the energy scale of LRSM interactions (> 1 TeV), which significantly higher than the Type-1 Seesaw Mechanism heavy neutrino interactions considered in this analysis (< 500 GeV). In general the LRSM signal leads to a highly boosted final state especially for the case where the masses of the particles satisfy $m_{W_R}, m_{Z_R} \gg m_{N_R}$. Consequently the jets from W_R and Z_R decays can become highly collinear and would be subsequently merged into one jet for the case of W_R decays or two or three jets for the case of Z_R decays in the ATLAS jet reconstruction.

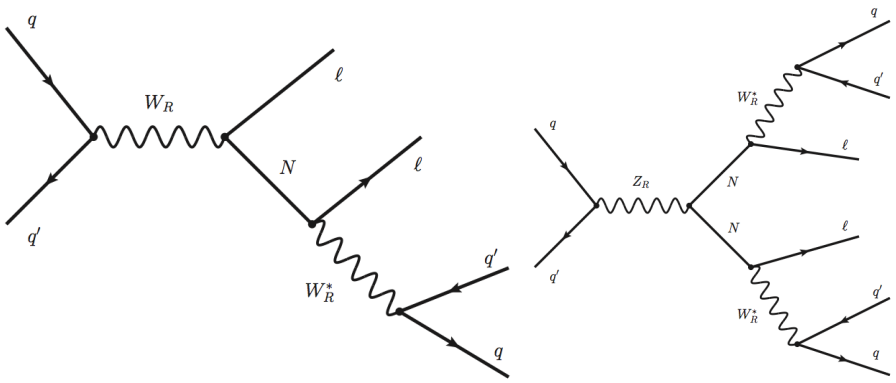

(a) (b)

Figure 3.6: Feynman diagram for the production of a heavy neutrino via (a) W_R decay in $qq' \to W_R \to N\ell \to \ell\ell jj$ and (b) Z_R decay in $qq' \to Z_R \to NN \to \ell\ell jjjj$.

3.7 Previous searches for heavy neutrinos

Limits on the direct production of heavy neutrinos have previously been set by experiments at the Large Electron Positron Collider (LEP) and the Large Hadron Collider (LHC) experiments. The LEP experiments set limits for heavy neutrino masses $m_N < 100$ GeV, and are presented in Section 3.7.1, and the LHC experiments set limits for $m_N > 100$ GeV which are presented in Section 3.7.2. For the case of $m_N < 100$ GeV, the experiments at the LHC will not be able to probe heavy neutrino masses with greater sensitivity than is currently set by the LEP experiments.

3.7.1 Indirect and LEP limits

Experiments prior to the LHC era have found no evidence for heavy neutrinos in the mass range 100 eV - 100 GeV (Figures 3.7a, 3.7b). For $m_N < 2$ GeV the strongest limits have been set by searches in leptonic decays of pions and kaons [24], and further limits were set in the e^+e^- collisions at LEP for $4 < m_N$ [GeV] < 100. A recent study of EW precision data [25] has found that at 90% CL:

$$|V_{eN}|^2 < 0.003, \quad |V_{\mu N}|^2 < 0.003, \quad |V_{\tau N}|^2 < 0.006, \quad |V_{eN}V_{\mu N}| < 3.5 \times 10^{-4}$$

respectively for heavy neutrino masses:

$$m_{N_e} \gtrsim \mathcal{O}(m_\pi), \quad m_{N_\mu} \gtrsim \mathcal{O}(m_\Lambda), \quad m_{N_\tau} \gtrsim \mathcal{O}(m_\tau), \quad m_{N_{e-\mu}} \gtrsim 100 \text{ GeV}.$$

Furthermore the most stringent limits on the electron-type heavy neutrino sector, assuming lepton-flavour conservation, are from experiments that aim to measure neutrinoless double beta decay. For a heavy Majorana neutrino mass which is large compared to the energy scale of the interaction, the contribution to the decay rate scales with the couplings $|V_{eN}|^2$ and heavy neutrino mass m_N as:

$$\left| \Sigma_{m'} \frac{V^2_{eN_{m'}}}{m_{N_{m'}}} \right|^2 . \tag{3.7}$$

For $m_{N_e} \gg 1$ GeV the current limit is [27]:

$$\left| \Sigma_{m'} \frac{V^2_{eN_{m'}}}{m_{N_{m'}}} \right| < 5 \times 10^{-5} \text{ TeV}^{-1}$$

which for the current best limits on $|V_{eN}|^2$, considering only the electron-type heavy neutrino, would require $m_{N_e} > 60$ TeV, although this scale can decrease due to cancellations when considering other lepton flavours.

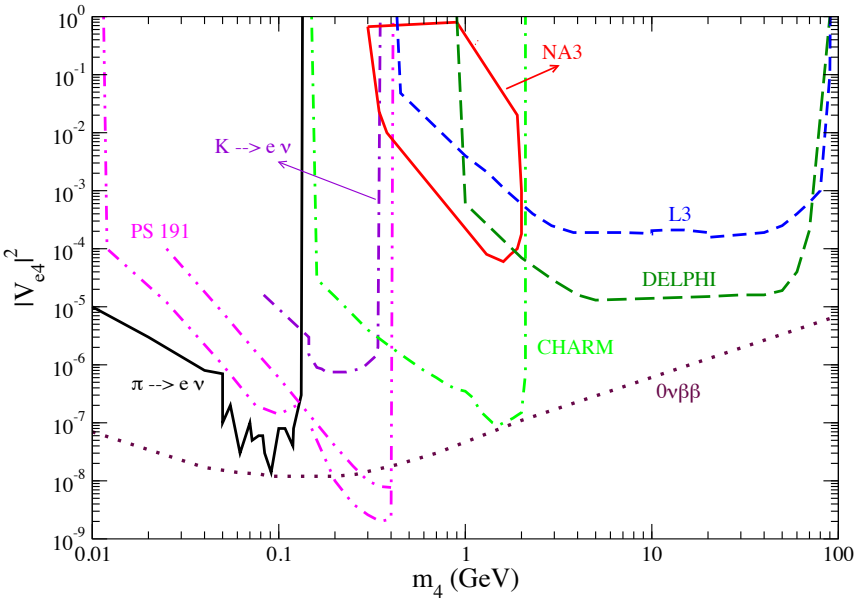

(a) Bounds on $|V_{e4}|^2$ versus m_4, where the subscript $_4$ refers to a heavy neutrino, in the mass range 10 MeV - 100 GeV. The excluded region with dotted maroon contour is derived from a reanalysis of neutrinoless double beta decay experimental data.

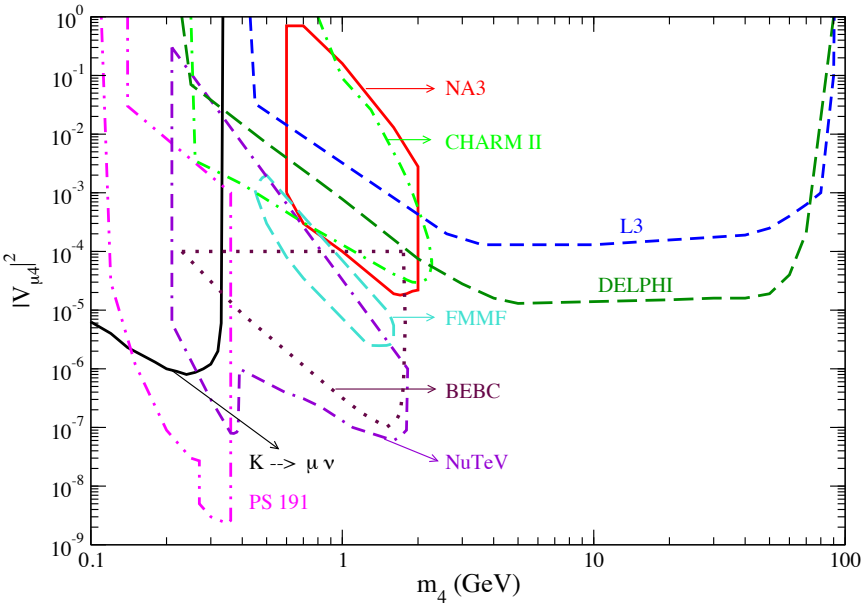

(b) Limits on $|V_{\mu 4}|^2$ versus m_4 where the subscript $_4$ refers to a heavy neutrino.

Figure 3.7: Current limits on heavy neutrino coupling as a function of heavy neutrino mass [26].

3.7.2 LHC limits

LHC experiments ATLAS and CMS have set limits on the production of heavy neutrinos in the frameworks of a radiatively induced neutrino mass, which is discussed in this thesis, and within a LRSM framework which is discussed in [28].

With a dataset corresponding to an integrated luminosity of 4.98 fb^{-1} collected by the CMS experiment at centre-of-mass energy $\sqrt{s} = 7$ TeV, 95% confidence level upper limits were set on the heavy neutrino-lepton coupling $|V_{lN}|^2$ [29]. Final states containing either two electrons or two muons were considered, where all pairs of leptons were required to have the same-sign (SS) electric charge. Heavy neutrinos with a mass in the range $90 < m_N$ [GeV] < 210 were considered in this study. The measured limits in the ee channel were the most stringent direct limits set to date for $m_N > 100$ GeV, before the analysis presented in this thesis.

Using a dataset corresponding to an integrated luminosity of 4.7 fb^{-1} collected by the ATLAS experiment at centre-of-mass energy $\sqrt{s} = 7$ TeV, 95% confidence level upper limits have been measured on the cross-section times branching ratio for the production of heavy Majorana neutrinos with a mass in the range $100 < m_N$ [GeV] < 300 with a final state containing two muons with SS electric charge [30]. The limits shown in Figure 3.8 were the most stringent limits in this mass range set to date before the analysis presented in this thesis is considered.

For the presented analysis the cross-section increases by a factor of two due an increase of centre-of-mass energy from 7 TeV to 8 TeV (Figure 3.9), and the search also benefits from a fourfold increase in dataset size. Furthermore the presented analysis will consider the mass range $100 < m_N$ [GeV] < 500 and also final states with either two electrons, two muons or the lepton number violating case of one electron and one muon in the final state.

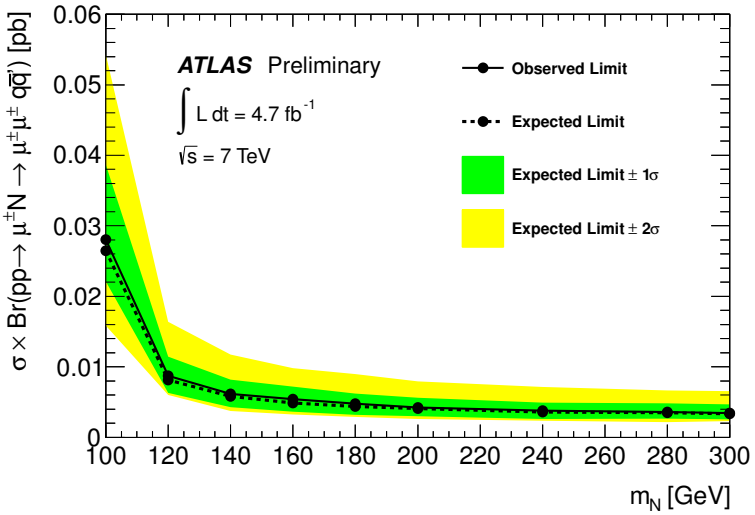

Figure 3.8: Observed and expected 95% confidence level limits on the cross section times branching ratio for the production of heavy Majorana neutrinos as a function of the heavy neutrino mass [30].

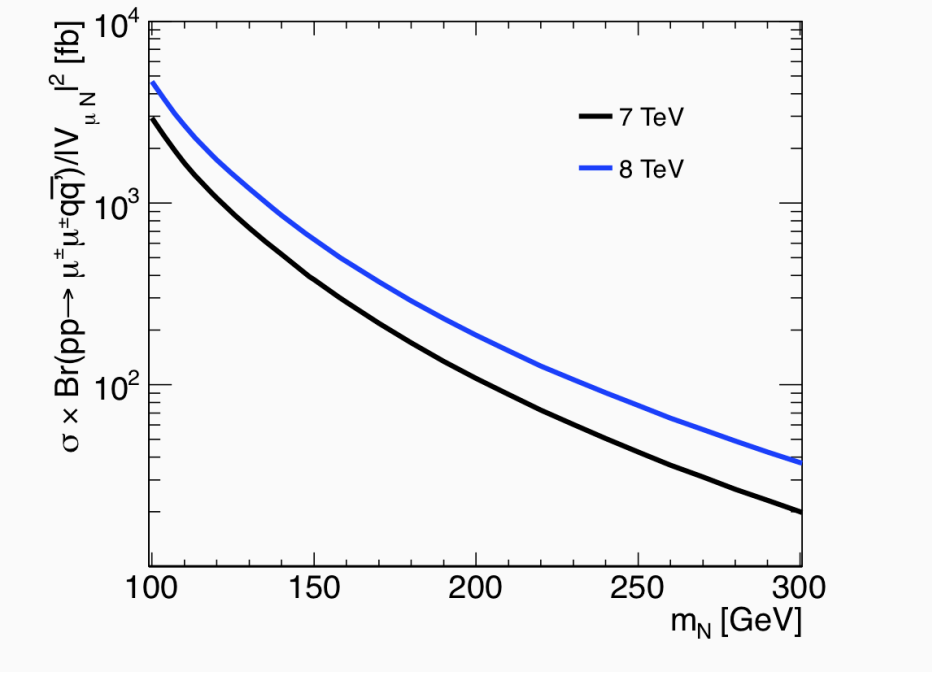

Figure 3.9: The cross-section for the process $pp \to (W^{\pm})^* \to N\mu^{\pm} \to \mu\mu$, normalised to the heavy neutrino-lepton coupling, as a function of heavy neutrino mass at $\sqrt{s} = 7$ TeV and $\sqrt{s} = 8$ TeV.

Chapter 4

The ATLAS detector at the Large Hadron Collider

4.1 The Large Hadron Collider

The Large Hadron Collider (LHC) [31], [32], [33] is a high energy proton-proton collider which follows the 26.7 km tunnel geometry originally used for the LEP collider [34], situated under the European Organisation for Nuclear Research (CERN) research laboratory in Geneva, Switzerland (Figure 4.1). There are four main experiments at the LHC studying various high energy physics processes. There are two specialist detectors: the ALICE experiment [35] which is designed to study the nature of hot dense states formed in heavy ion collisions, and the LHCb experiment [36] which predominantly makes measurements of heavy meson decays in order to gain an insight on rare processes and test matter-antimatter asymmetries. ATLAS and CMS [37] are general purpose detectors designed to search for a wide range of new and rare physics, as well as making precision and high energy tests of established physics processes. The ATLAS detector collected the data used in this thesis and is described in detail in Section 4.2.

One of the key features of the LHC programme is the production and circulation of high instantaneous luminosity (L_{inst}) beams. The LHC beams reached a peak instantaneous luminosity of approximately $L_{\text{inst}} = 7 \times 10^{33}$ cm^2s^{-1} in 2012, close to the design luminosity of 10^{34} cm^2s^{-1} which the LHC

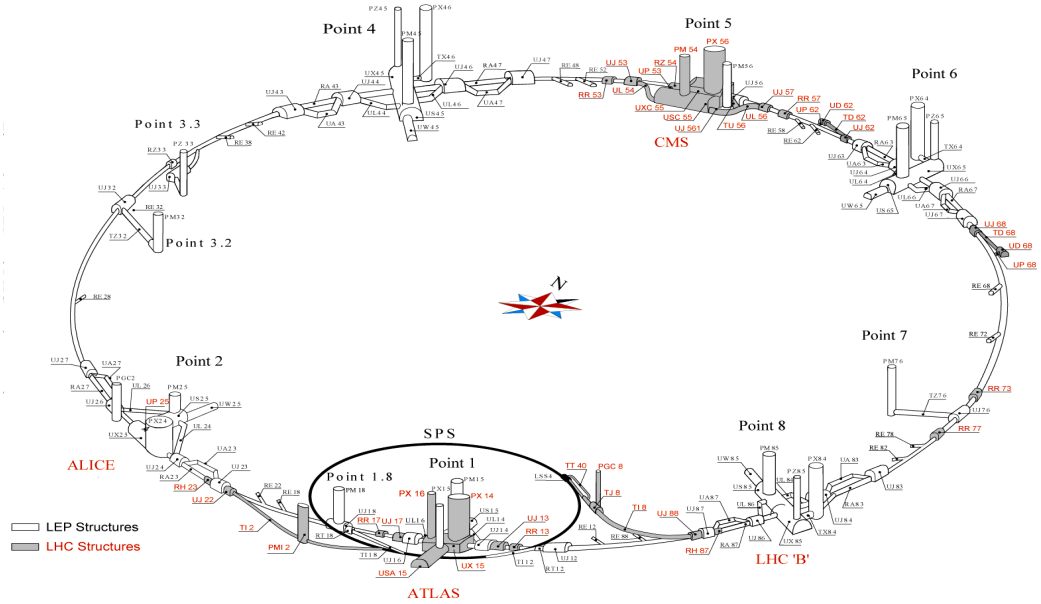

Figure 4.1: Schematic of the LHC/LEP and SPS tunnel structure, with the main experiments marked at points 1, 2, 5 and 8 [32].

is expected to exceed when collisions recommence in 2015. One can express the instantaneous luminosity of a beam in terms of beam parameters as:

$$L_{inst} = \frac{N_b^2 n_b f_{rev} \gamma_r}{4\pi\epsilon_n \beta*} F$$

where N_b is the number of particles per bunch, n_b is the number of bunches per beam, f_{rev} is the revolution frequency, γ_r is the relativistic gamma factor, ϵ_n is the normalised transverse emittance, $\beta*$ is the beta function at the collision point and F is the geometric luminosity reduction factor at the interaction point. A summary of the beam parameters is given in Table 4.1. Each LHC beam contains 2808 proton bunches, with the bunch spacing designed to be ≥ 25 ns. The LHC is expected to achieve this bunch spacing at a later stage in the programme despite running with 50 ns spacing in the most recent beam running. The number of events N produced per second at the LHC for a given process with total cross-section σ and the machine luminosity L_{inst} is calculated as:

$$N = L_{\text{inst}} \sigma.$$

Given that the total proton-proton cross-section is approximately 110 mb, the total event rate at the LHC design luminosity is approximately 40 MHz. This places strong requirements on the data acquisition rate and trigger efficiency of the LHC detectors, especially if one considers that the cross-section of some rare or exotic processes, such as Higgs or heavy neutrino production, imply a production rate $\lesssim 10$ mHz [38].

In order for the LHC to achieve high luminosity beams it is required that both colliding beams are composed of protons, as opposed to the Tevatron collider, Illinois, which collided beams protons with beams of anti-protons [39]. Protons for the LHC beams are extracted from a hydrogen source and subsequently injected into stages of higher acceleration before reaching the LHC where they are accelerated in RF cavities to their collision energy. The stages of the LHC accelerator system and the corresponding incremental increases in design beam energy are described in Table 4.2. In order to circulate beams of like-sign electrical charge the LHC is composed of two rings with independent magnetic fields and vacuum chambers, although the rings share common magnetic and vacuum chambers at the crossing regions in the detector caverns. The beams have separate injection insertions which transfer protons from the SPS system indicated in Figure 4.1. In order to remove the beams with off-normal parameters, a dedicated beam dumping system is in place to transport the beams to external absorbers.

The LHC is currently in a period of scheduled shutdown. When collisions resume in 2015 the LHC will collide proton beams close to its design centre-of-mass energy $\sqrt{s} = 14$ TeV. The LHC started running in 2008, although within nine days a mechanical fault delayed running until 2010. By the end of 2010, beams were running at centre of mass energy $\sqrt{s} = 7$ TeV and instantaneous luminosity $L_{\text{inst}} = 1 \times 10^{32}\text{cm}^2\text{s}^{-1}$. In 2012, the LHC achieved collisions with $\sqrt{s} = 8$ TeV as well as maintaining significant increases in instantaneous luminosity (Figures 4.2, 4.3). With half of this dataset in 2012, the ATLAS and CMS collaborations were able to discover Higgs boson [41].

	Injection	Collision
Proton energy [GeV]	450	7000
Relativistic gamma	479.6	7461
Number of particles per bunch	1.15×10^{11}	
Number of bunches	2808	
Longitudinal emittance [eVs]	1.0	2.5
Transverse emittance [μm rad]	3.5	3.75
Circulating beam current [A]	0.584	
Stored energy per beam [MJ]	23.3	362

Table 4.1: The LHC design beam parameters at injection and collision point [31].

Accelerator system	Outgoing proton energy [GeV]
LINAC2	5
PSB	1.4
PS	25
SPS	450
LHC	7000

Table 4.2: The design outgoing proton energies at five stages in the LHC accelerator system [31].

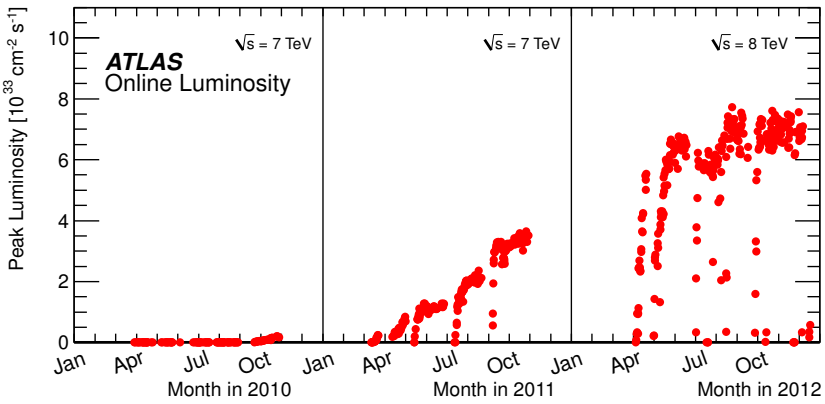

Figure 4.2: The instantaneous luminosity recorded by the ATLAS experiment in 2010, 2011 and 2012 [40].

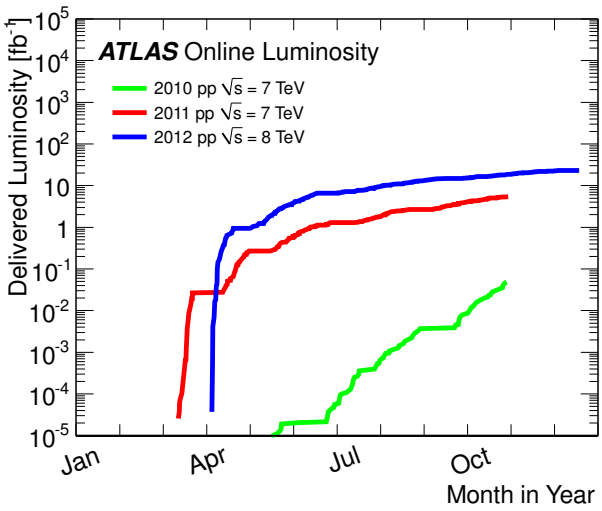

Figure 4.3: The integrated luminosity recorded by the ATLAS experiment in 2010, 2011 and 2012 [40].

4.2 The ATLAS detector

ATLAS [42] is a general purpose particle detector situated 92.5 metres underground at LHC Point 1 of Figure 4.1. The ATLAS detector, shown in Figure 4.4, is designed to search for new physics and make precision measurements of SM processes. The primary aim was the discovery of the Higgs boson, which like many processes that are probed by ATLAS has a low production cross-section in the most sensitive channels. ATLAS is designed to record an integrated luminosity of at least 300 fb^{-1} in the first ten years of running in order to achieve the precision required to discover or exclude new physics at the TeV-scale.

A consequence of the LHC's high instantaneous luminosity is the large number of proton-proton collisions per bunch crossing or 'pile-up' interactions, which are described in more detail in in Section 4.2.7. In 2012 ATLAS measured an average of 20.7 primary interaction vertices per bunch crossing. One should consider that typical ATLAS analyses aim to reconstruct events that correspond to only one of these vertices. With this in mind the ATLAS detector must be able to effectively extrapolate tracks to a primary vertex which requires a high resolution Inner Detector (ID) tracker- which is discussed in Section 4.2.3. A further challenge for ATLAS in a high luminosity

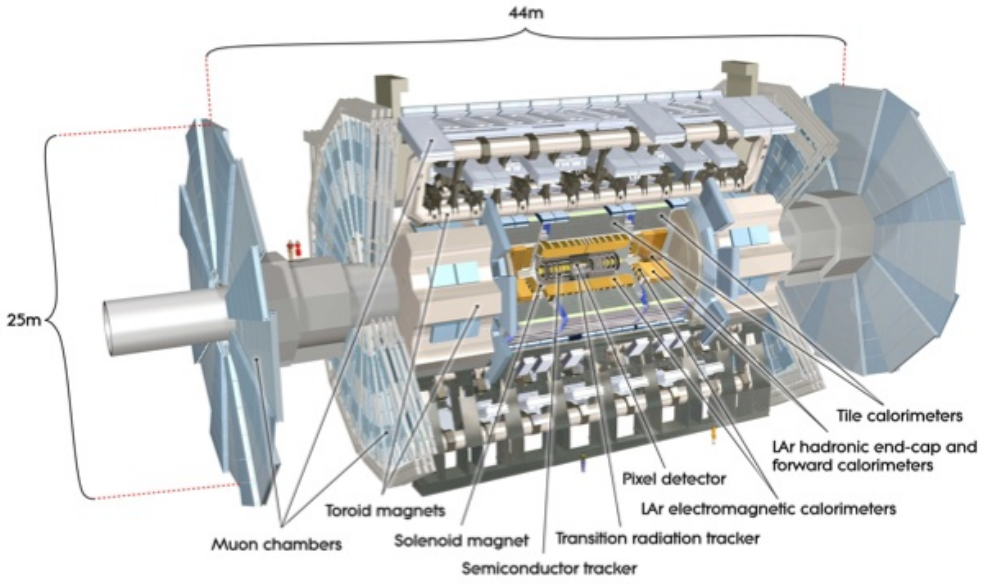

Figure 4.4: Diagram of the ATLAS detector, with one side cut away revealing the inner detector system, calorimeters, magnet system and muon spectrometer [42].

environment is that it must be able to record data at the level of 200 Hz from the initial bunch crossing rate of approximately 40 MHz [43]. This is managed by the Trigger and Data Aquisition (TDAQ) system which makes decisions on which events to retain in order to maximise signal purity and reduce event rates, and is described in detail in Chapter 5.

In order to consider the full diversity of final states that ATLAS is sensitive to, one can look to the 2012 ATLAS publication of the first observation of a Higgs-like particle, which used a combination of five search channels [41]. The high resolution Muon Spectrometer (Section 4.2.5) and Electromagnetic Calorimeter (Section 4.2.4) were required for accurate lepton identification and measurement at high energy in the decay $H \to V^{(*)}V$ $(V = W, Z)$ with multi-lepton finals states. The Electromagnetic Calorimeter was also required for photon identification in the $H \to \gamma\gamma$ search channel which relies on accurate separation from electrons. The ATLAS Inner Detector (Section 4.2.3) was required for fine momentum resolution and position vertexing in the $H \to bb$ channel by searching for decay vertices which are displaced from the Interaction Point (IP), due to the relatively long life of B-hadrons.

The Hadronic Calorimeter (Section 4.2.4) was used to separate jets (Section 7.5) from leptons (including hadronic τ decays) and photons. The combined calorimetry system also provides a measurement of missing transverse energy E_T^{miss} which is associated with neutrino production.

4.2.1 ATLAS coordinate system and detector overview

The coordinate system of the ATLAS detector is described in terms of a forward-backward symmetric cylindrical geometry about the beam-axis z, centred at the Interaction Point (IP). A Cartesian x-y plane is defined as the surface perpendicular to z such that x points towards the centre of the LHC ring and y points vertically upwards. The azimuthal angle ϕ describes the angle about z in the x-y plane. The Cartesian axes are imposed onto ATLAS in Figure 4.5a. ATLAS is defined to have three sides - sides A and C referring to the ATLAS end-caps (set in the x-y plane) with positive and negative z respectively and side B referring to the barrel surface, wrapped about z. Pseudorapidity η is related to the polar angle θ with respect to z (Figure 4.5b). Differences in angular position are given in terms of a cone ΔR, defined as the distance in pseudorapidity-azimuthal angle space:

$$\Delta R = \sqrt{\Delta\eta^2 + \Delta\phi^2}.$$

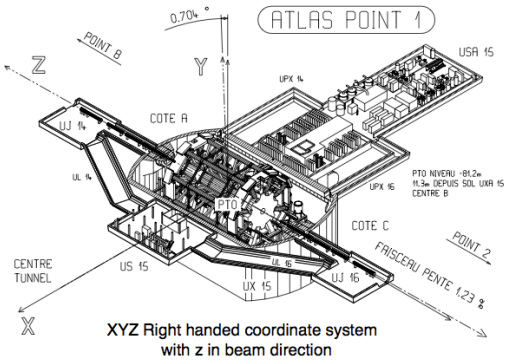

(a) The cartesian coordinate system (x,y,z) imposed onto the ATLAS detector [44].

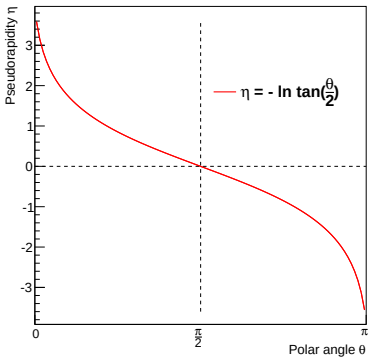

(b) Conversion from polar angle θ from beam axis z to pseudorapidity η.

Figure 4.5: The ATLAS coordinate system.

LHC experiments typically describe particle trajectories in terms of η and ϕ and particle kinematics in terms of transverse momentum p_T and transverse energy E_T. Transverse impact parameter d_0 is defined as the transverse distance to the z-axis, signed according to the angular momentum of the track. Longitudinal impact parameter z_0 is defined as the z position of the track origin relative to the point of closest approach.

The ATLAS detector is 44 m long and 25 m in height with the Inner Detector at its centre surrounding the beam line with a radius 1.2 m and length 3.5 m. The calorimetry system extends 4.4 m radially from the Inner Detector to the Muon Spectrometer which extends a further 7 m. ATLAS is mounted on a dedicated feet and rail system consisting of nine pairs of feet in the range $-2.1 < \phi < -1.1$ and which support the approximately 6000 tonne structure over a distance of 25 m.

Detector		η coverage		Resolution
System	Subsystem	Subsystem	Total	
ID	TRT	$\pm$ 2.0	$\pm$ 2.5	$\sigma_{p_T}/p_T = 0.05\%\ p_T \oplus 1\%$
	Pixel	$\pm$ 2.5		
	SCT	$\pm$ 2.5		
MS	MDT	$\pm$ 2.0	$\pm$ 2.7	$\sigma_{p_T}/p_T = 10\%$ (at $p_T = 1$ TeV)
	CSC	$2.0 < \lvert\eta\rvert < 2.7$		
	TGC	$1.05 < \lvert\eta\rvert < 2.4$		
	RPC	< 1.05		
ECal	Barrel	< 1.475	$\pm$ 3.2	$\sigma_E/E = 10\%/\sqrt{E} \oplus 0.7\ \%$
	Endcap	$1.375 < \lvert\eta\rvert < 3.2$		
	Presampler	< 1.8		
HCal	Tile	< 1.7	$\pm$ 3.2	$\sigma_E/E = 50\%/\sqrt{E} \oplus 3\ \%$
	HEC	$1.5 < \lvert\eta\rvert < 3.2$		
	FCal	$3.1 < \lvert\eta\rvert < 4.9$		$\sigma_E/E = 100\%/\sqrt{E} \oplus 10\ \%$

Table 4.3: ATLAS subdetector η coverage and resolution of energy E or transverse momentum p_T.

ATLAS is primarily divided along $|\eta| \approx 1.0$ which separates the central 'barrel' region from the two 'end-caps' regions, which also contain the 'forward' regions for $|\eta| > 3.2$. In order to reflect the different structure of these regions the geometric acceptance of ATLAS is usually parameterised in η, although there are also some inhomogeneities in ϕ, for example in the feet region. The geometric acceptance of each detector system and corresponding subsystems is detailed in Table 4.3, which also lists the p_T (or E_T) resolution of each detector system. The requirements and design specifications for each of the subsystems is described briefly in the following sections.

4.2.2 Magnet system

The ATLAS magnet system (Figure 4.6a) generates two magnetic fields in order to provide bending power for deflecting charged particles so that the curvature of a reconstructed track can be related to the momentum of the particle. The magnet system is composed of two regions - a central solenoid aligned to the beam axis and an exterior system of toroids. The central solenoid provides a 2 T magnetic field to the Inner Detector system and is only 45 mm thick in order to increase particle transparency to the calorimetry system. A combination of barrel and end-cap toroids delivers approximately 0.5 T and 1 T respectively for the Muon Spectrometer system.

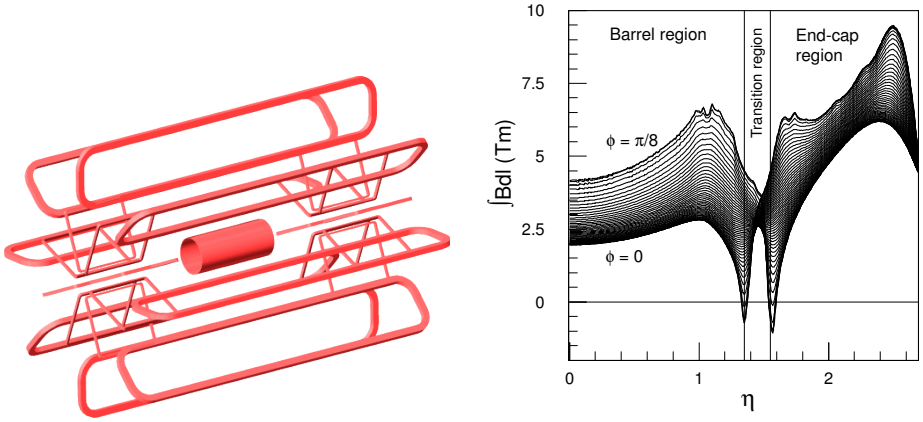

(a) (b)

Figure 4.6: The ATLAS magnet system (a) layout and (b) toroidal bending power as a function of (η, ϕ).

The two endcap toroids, which provide a magnetic field in the forward region, are aligned to each end of the central solenoid and positioned within the barrel toroid. The coils of the end-cap toroids are rotated by 22.5° with respect to the barrel toroid in order to optimise the bending power (Figure 4.6b) in the transition regions between the barrel and end-caps. The entire magnet system is cooled to 4.8 K with liquid helium from ATLAS's dedicated cryogenics system [45].

4.2.3 Inner detector

The ATLAS Inner Detector (ID) is designed to perform precision tracking at high luminosity. Its function is vital in high pile-up conditions where it is required to separate primary interaction vertices [46]. The ID also measures secondary vertices which are used for identifying B-hadrons. The vertex resolution in the z-direction is measured by the ID to be approximately 50 μm for high track multiplicities, providing fine resolution compared with the Gaussian parameter $\sigma_z = 5.6$ cm produced from LHC measurements.

As the ATLAS solenoidal magnet is 1.4 m shorter along the beam axis than the ID, the magnetic field across the ID system varies from 2.09 T to approximately 1.0 T at the edge of the solenoid and 0.5 T at the edge of the ID. To satisfy the ATLAS physics requirements the momentum resolution is required to be sufficient such that for an electron with $p_T = 0.5$ TeV the charge misidentification probability is no more than 0.13%. It follows that the intrinsic resolution $\sigma(1/p_T)$ should be at least 0.6 TeV^{-1}.

The ID is composed of three independent sub-detectors as shown in Figure 4.7. These are the Pixel and Semi-Conductor Tracker (SCT) detectors, which are at small radii and provide precision tracking, and the Transition Radiation Tracker (TRT) which is at larger radii and enhances pattern recognition.

The Pixel detector [47] is composed of 1744 sensors with dimensions $(0.25 \times 19 \times 63)$ mm^3 which are arranged to form three concentric cylinders with three disks located at the cylinder ends centred on the beam-axis. The SCT [48] combines with the Pixel detector to provide precise tracking

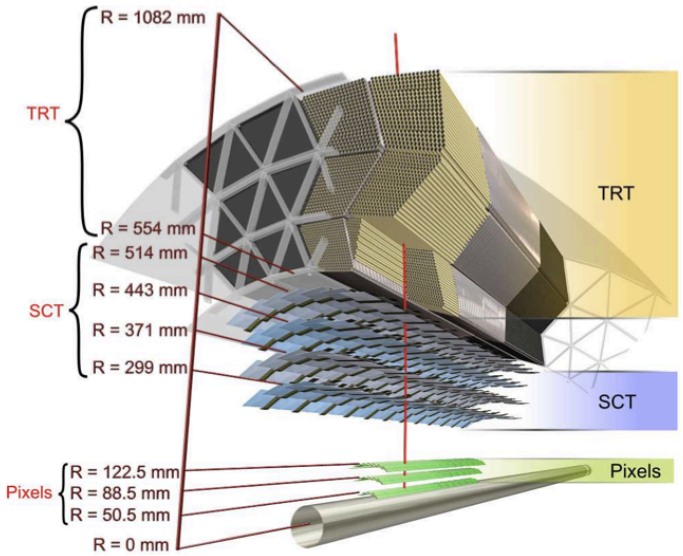

Figure 4.7: A slice of the ATLAS Inner Detector at $\eta \approx 0.0$ [42].

at extended radii. It is radially the central component of the ID system and is composed of 15912 silicon strips (80 μm $\times$ 12 cm). The TRT is formed of 25 μm thick Polyimide films wrapped into tubes (stabilised using carbon fibres) with diameter 4 mm and length in the barrel of 144 cm and length in the end-caps of 37 cm. The tubes are filled with a gas mixture of 70% Xe, 27% CO_2 and 3% O_2, described in detail in [42].

4.2.4 Calorimetry

Calorimetry systems are designed to determine the energy of incoming particles. The ATLAS calorimeters [49] are sampling calorimeters, consisting of absorbing layers and readout electrodes. Incoming particles interact with the absorbing layers to produce 'showers' of secondary particles via EM or nuclear interactions which are ultimately measured in the electrodes. The showering properties of the material in the absorbing layer are characterised by its hadronic (nuclear) and EM interaction lengths $\lambda^{\text{hadronic}}$ and λ^{EM}, which quantify the thickness of material required for a particle to be reduced to 37% of its initial energy.

The ATLAS calorimetry system consists of one barrel and two end-cap

calorimeters. The barrel and end-cap detectors are subdivided into EM Calorimeter (ECal) and Hadronic Calorimeter (HCal) systems. The end-cap calorimeter also contains the Forward Calorimeter (FCal) for measurements of forward jets. Liquid Argon (LAr) is used in all of the ATLAS calorimetry (except for the Tile calorimeters, which will be described later) as the active detector medium due to its intrinsic linear behaviour, its stability of response over time and intrinsic radiation-hardness. The specific composition and requirements of the ATLAS ECal and HCal systems is discussed in the following sections.

Electromagnetic Calorimeter

The ECal system has complete ϕ-coverage for the barrel and end-cap regions defined by $|\eta| < 1.475$ and $1.375 < |\eta| < 3.2$ respectively. The absorption layers of the ECal system consist of lead and form an accordion-shaped geometry with the electrodes as illustrated in Figure 4.8. The depth of the EM calorimeter D_{EM} varies with rapidity such that the barrel and end-caps depths are given by:

$$D_{\text{EM}}^{\text{barrel}} > 24\ \lambda^{EM}$$
$$D_{\text{EM}}^{\text{endcap}} > 26\ \lambda^{EM}.$$

As particles entering the calorimeter have traversed $\gtrsim 1.8\ \lambda^{EM}$ in the Inner Detector system, energy losses are corrected by using a 'presampler' which consists of an active LAr layer of thickness 1.1 cm in the barrel and 0.5 cm in the end caps.

Hadronic Calorimeter

The size of the HCal is required to entirely contain hadronic showers before they can penetrate the Muon Spectrometer system. At $\eta = 0$ a total thickness of 11 $\lambda^{\text{hadronic}}$ is sufficient to address this. The composition of the hadronic calorimeter varies with pseudorapidity to reflect different requirements and radiation environments. The Tile calorimeter operates in the region $|\eta| < 1.6$ and a LAr system is used for $1.5 < |\eta| < 4.9$. The end-cap HCal extends to $|\eta| < 3.2$ and the forward region is covered for the range $3.2 < |\eta| < 4.9$.

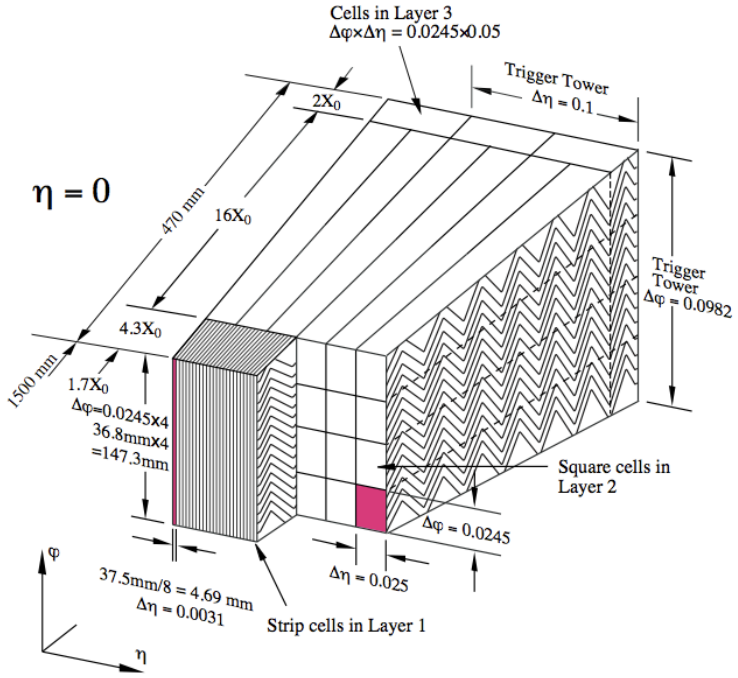

Figure 4.8: Schematic layout of a barrel electromagnetic module.

The Tile calorimeter consists of an alternating arrangement of iron and scintillating tiles each of thickness 3 mm. The tiles are positioned such that they are perpendicular to the beam axis. A periodic structure of tiles, staggered in depth, is used such that the total thickness of the iron plates is 14 mm per period. In addition to the Tile calorimeter there are two Hadronic Endcap Calorimeters (HECs) which each consist of two copper-plated wheels using Liquid Argon as the active medium.

Unlike the HEC and Tile calorimeters, ATLAS's FCal must be particularly dense in order to accommodate $> 9\ \lambda^{hadronic}$ and must be able to withstand a high radiation dose as it is situated 5 m from the IP. In order to meet these requirements the FCal system consists of three sections, such that the first layer is composed of copper and the outer two layers consist of tungsten.

4.2.5 Muon spectrometer

The Muon Spectrometer (MS), shown schematically in Figure 4.9, is the largest and outermost layer of the ATLAS detector system, accounting for 85 % of the total detector volume. It is designed to detect charged particles with trajectories within $|\eta| < 2.7$. The MS sub-detectors in the barrel and the end-cap regions are both positioned in concentric layers known as 'stations'. The MS is composed of 'trigger' and 'precision' chambers, which will be discussed in this section. There are three stations of trigger chambers in both the barrel and end-caps, in addition to three stations of precision chambers in the barrel and four stations in the end-cap.

In general only muons are detected in the MS system as other particles are expected to be fully contained by the calorimetry system. This is because muons emit relatively low levels of bremsstrahlung radiation compared to electrons and do not interact hadronically with the HCal. Secondary particles from beam-beam interactions also have a relatively high rate in the MS, although these can be rejected by comparing MS track information to tracks reconstructed in the ID (Section 7.3). It is required however that muons are reconstructed by the MS without information from the other detector systems with transverse momentum resolution of approximately 10% for 1 TeV muons. Additionally the MS is required to trigger on particles in the region $|\eta| < 2.4$ with its dedicated triggering system of Resistive Plate Chambers (RPCs) and Thin Gap Chambers (TGCs). Precision tracks are subsequently reconstructed with information the the Monitored Drift Tubes (MDTs) and Cathode Strip Chambers (CSCs) subsystems.

Muon spectrometer trigger chambers

The MS trigger system (Figure 4.10) is designed to provide fast measurements of muon p_T and (η, ϕ) track coordinates to the Level 1 (L1) trigger system which will ultimately be used in the muon High Level Trigger (HLT).

RPCs are chosen to operate in the barrel region of the MS ($|\eta| < 1.05$) as they offer sufficient spatial and time resolution whilst maintaining a rate that is manageable for the L1 trigger to process. Each of the RPCs consists of

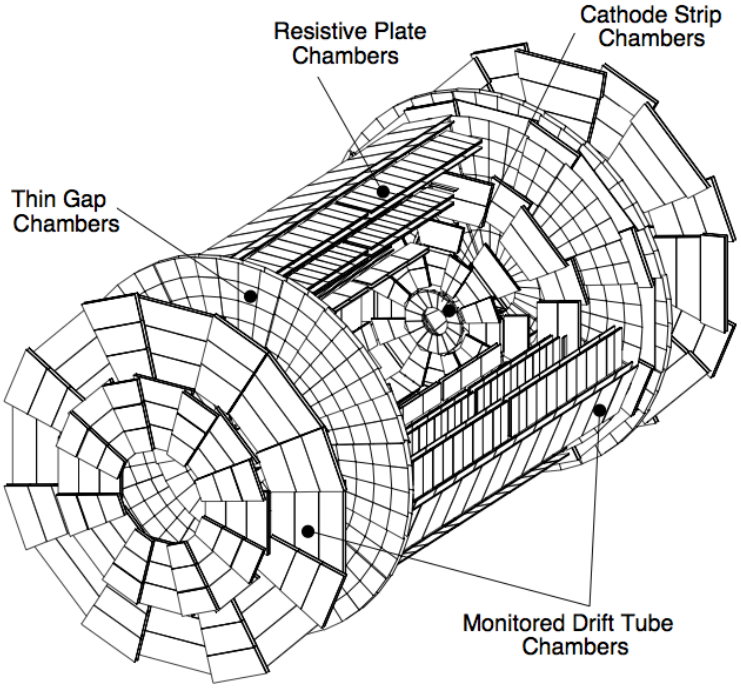

Figure 4.9: An overview of the ATLAS Muon Spectrometer with the independent subsystems highlighted.

two parallel resistive plates separated by 2 mm. The intermediate volume is filled with a gas, and an electric field is applied between the plates so that 'avalanches' of charge form along the paths of charge particles which ionise the gas. The gas mixture (which is detailed in [42]) is chosen for its non-flammability, low cost and safe avalanche formation.

A system of TGCs operates in the end-cap region defined by $1.05 < |\eta| < 2.4$. These are used to provide signals with finer granularity in the end-caps than the barrel region as particle tracks are generally less curved due to large inhomogeneities in the magnetic field. TGCs offer good time resolution and are able to operate at a high rate. The TGCs are multi-wire proportional chambers filled with a quenching gas mixture [42].

Muon spectrometer precision chambers

MDTs are used to measure particle momenta in the region $|\eta| < 2.7$ by precise determination of the η coordinate which is matched to a track measured

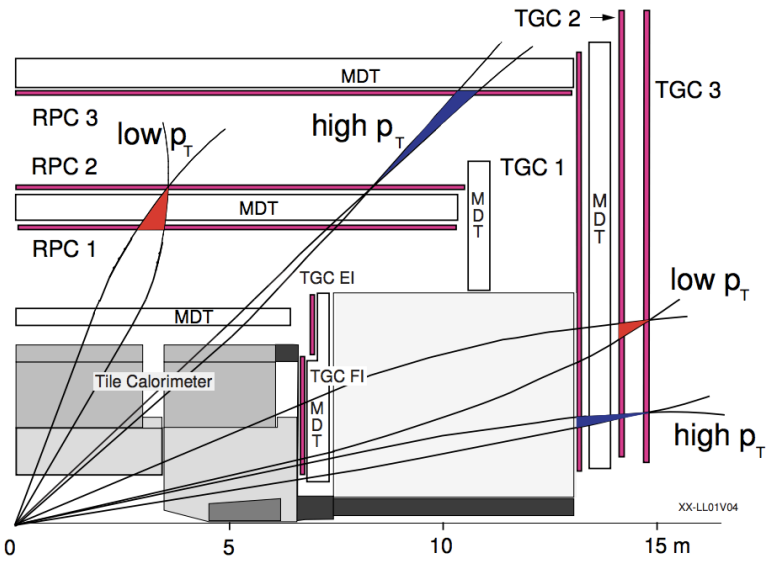

Figure 4.10: An overview of the ATLAS Muon Spectrometer trigger system with examples of high and low p_T tracks overlaid.

in the trigger chamber system. The MDTs are arranged in the barrel region in three concentric stations at approximately 5 m, 7.5 m and 10 m, such that the chambers in each layer cover an increasingly larger area. In the end-cap regions, the MS is composed of large wheels in the x-y plane, positioned at approximately 7.4 m, 10.8 m, 14 m and 21.5 m from the IP. The innermost MDT end-cap wheels only cover the region $|\eta| < 2.0$ to ensure that the design counting rate of 150 Hz cm^{-2} is not exceeded. A small wheel of CSCs is used in the otherwise uncovered region with $2.0 < |\eta| < 2.7$ as they are able to operate with counting rates up to 1000 Hz cm^{-2}.

The CSCs are multi-wire proportional drift chambers whereas the MDTs are composed of a number of pressurised cathode tubes, each < 30 mm in diameter, with an anode wire suspended through the centre of each tube. Both technologies determine charged particle position by measuring the drift time for charge induced by ionisation of the gas mixture to reach the wire.

4.2.6 The ATLAS-LHC interface and luminosity determination

The main interface between ATLAS and the LHC is the beam pipe vacuum system which is maintained at a pressure of 10^{-13} atm [31]. When in operation, ATLAS and the LHC continually exchange information of various beam parameters in order to optimise the combined operation. Unstable beams can be safely extracted from the LHC machine in a process known as a beam-dump which typically takes less than 300 μs.

The integrated luminosity delivered to ATLAS is calculated using the Beam Conditions Monitor (BCM) and LUCID detectors [50], which are fast detectors capable of making statistically precise luminosity measurements. The BCM consists of four small diamond sensors, each with ~ 1 cm^2 cross-section, which are arranged around the beam pipe on each side of the IP, at a distance of $z = 184$ cm. LUCID is a Cherenkov detector consisting of 16 aluminium tubes filled with a gas mixture surrounding the beam pipe on each side of the IP at a distance of $z = 17$ m, in the region $5.6 < |\eta| < 6.0$. The two detectors and various algorithms are calibrated using van der Meer scans [51], with the central value provided by the BCM detector.

4.2.7 Pile-up

Pile-up in high luminosity colliders occurs due to multiple pp collisions per bunch crossing. The mean number of pp interactions per bunch crossing μ is calculated according to:

$$\mu = \frac{L\sigma_{\text{inel}}}{n_{\text{bunch}} f_r} \tag{4.1}$$

where L is the luminosity, σ_{inel} is the total inelastic cross-section, n_{bunch} is the number of colliding bunches and f_r is the LHC revolution frequency. The pile-up of a particular run (or number of runs) is quantified in terms of the peak number of interactions per bunch crossing μ^{peak} or the mean value $\langle\mu\rangle$.

Chapter 5

The ATLAS Trigger and Data Acquisition system

The ATLAS trigger system is designed to reduce the recorded event rate from the initial bunch crossing rate of approximately 40 MHz so that data can be written to disk at a manageable level, which is typically below 1 kHz. ATLAS reduces the rate in three sequential stages known as Level 1 (L1), Level 2 (L2) and Event Filter (EF). The L1 stage is hardware based and the High Level Trigger (HLT), which refers to the combined L2 and EF system, is software based.

The L1 trigger system is based on custom electronics which use fast muon trigger information and low granularity calorimeter signals. The L1 system has two main functions; firstly it is required to reduce the rate that is passed to the HLT and secondly it is used to seed the HLT with Regions of Interest (RoIs), which are η-ϕ regions centred about L1 trigger objects.

The L2 trigger accesses information from the detector in RoIs in order to reconstruct L1 objects at a higher resolution using dedicated fast algorithms. The final stage of the trigger is the EF which has access to the full detector information. This stage uses algorithms that are very similar to those used in the full object reconstruction (described in Chapter 7) which means that the EF trigger reconstructs objects with resolutions comparable to fully re-

constructed objects.

The three tiers of the ATLAS trigger are sequenced in a trigger 'chain' in order to select a specific signal. In 2012 almost 700 different trigger chains were used by ATLAS when recording data [52]. A simple example of a trigger chain is the following muon trigger sequence:

$$\texttt{L1\_MU15} \rightarrow \texttt{L2\_mu24\_tight} \rightarrow \texttt{EF\_mu24i\_tight}$$

where `L1_MU15` corresponds to an L1 muon algorithm that selects events with at least one muon candidate with $p_T > 15$ GeV and `L2_mu24_tight` and `EF_mu24i_tight` correspond to L2 and EF muon algorithms respectively that select events with at least one muon candidate with $p_T > 24$ GeV. Additional details of the trigger nomenclature used here is given in Section 5.3. There are also more complex 'combined' trigger chains, which use additional algorithms in the sequence to select events with more specific topologies, which reduce the event rate without implementing tight p_T cuts.

Trigger signature groups are defined to group together similar trigger chains. Each of the main trigger signatures (b-jets, B-physics, e/gamma, Jets, Missing E_T, Muons and Tau) take a share of the maximum rate allowance at each trigger level. The rate allowance for each signature is detailed in Table 5.1. Each signature achieves their specific rate allowance by either only recording a preset fraction of events, known as a prescale, or only recording events which pass specific selection criteria. The selection criteria are primarily implemented in terms of particle p_T, although more complex criteria can be applied in the HLT system in order to reduce event rates.

Signature	Peak L1 rate (Hz)	Peak L2 rate (Hz)	Average EF rate (Hz)
b-jets	5000	900	45
B-physics	7000	50	20
e/gamma	30000	2000	140
Jets	3000	1000	35
Missing E_T	4000	800	30
Muons	14000	1200	100
Tau	24000	800	35
Total	65000	5500	400

Table 5.1: Peak and average rates for the main trigger signatures in a typical fill in 2012 with peak instantaneous luminosity of 7×10^{33} cm^{-2}s^{-1}. There is significant overlap between the groups (particularly at L1), which is accounted for in the total.

5.1 Level 1 trigger

The L1 trigger uses information from the muon trigger chambers and each of the calorimeter subsystems in order to identify objects of interest. After a signal is identified, the Central Trigger Processor (CTP) processes the final L1 decision. Information about the η-ϕ trajectory and p_T of trigger objects is stored in the L1 trigger processors so that it can seed the HLT in the form of RoIs.

The L1 calorimeter trigger identifies objects (or events) with high E_T or large E_T^{miss}. High E_T objects include electrons and photons, jets, and tau-leptons decaying into hadrons. The basic architecture follows a three-tier system which starts by digitalising analogue input signals which are translated into units of E_T using a Look-Up-Table (LUT). These are transmitted to the Cluster Processor (CP) and Jet Energy-sum Processor (JEP) in order to perform sums of E_T, E_T^{miss} (in the CP) and numbers of jets, electrons, photons and hadronic tau decays (in the JEP) which are then sent to the CTP.

The L1 muon trigger operates solely with the RPCs and TGCs in the barrel

and end-caps respectively in order to search for high p_T muons which are coarsely consistent with originating in the interaction region. Muon candidates are categorised according to whether they have passed the highest of six p_T thresholds. These thresholds are 0, 6, 10, 11, 15 and 20 (in units of GeV). The trigger system passes information of signal position and p_T threshold to the CTP. At L1 60% of muon candidates detected in the end-caps arise from secondary particles from beam interactions. These are subsequently rejected at L2 by matching to ID tracks. The L1 muon rate and L1 muon fake rate are shown in Figure 5.1. L1 muon triggers are identified as being fake if the corresponding L1 muon candidate does not match to an offline reconstructed muon.

5.2 The HLT

The HLT refines detector signals, which start with input RoIs from the L1 trigger. Trigger decisions are then applied in a series of steps, using data from increasingly more detector systems. Trigger chains associated with a physics signature are tested with hypothesis algorithms in order to determine whether identified features (tracks, calorimeter clusters and E_T measurements) meet the criteria of the physics signature. Only L2 triggers that pass the hypothesis algorithm decision are forwarded to the EF. Correspondingly, only events with EF particle candidates that pass the hypothesis algorithm decision will be written to disk.

As the author contributed to the maintenance and operation of the muon HLT system, it will be discussed in some detail in this section.

5.2.1 The L2 muon trigger

The muon HLT is seeded with RoIs produced by the L1 muon trigger's hardware-based logic. The L2 trigger uses additional information from the the MDTs in order to refine the L1 muon candidate. The coordinates of the muon track are calculated by fast algorithms that utilise drift times in the MDTs, and the muon p_T is reconstructed by using LUTs in order to reduce

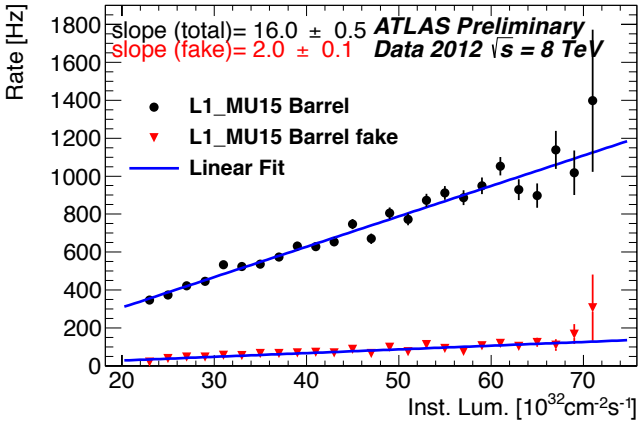

(a)

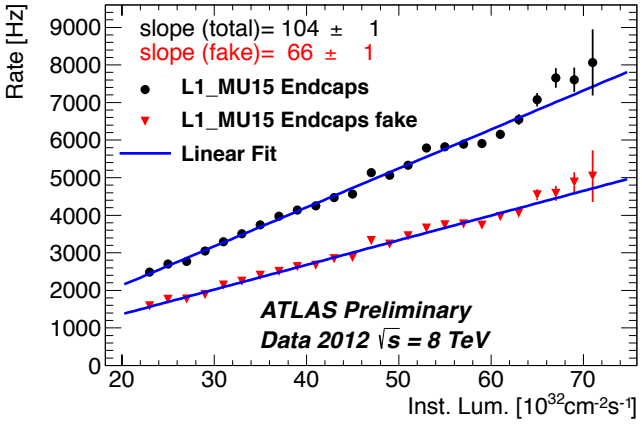

(b)

Figure 5.1: L1 muon rates as a function of the instantaneous luminosity in the ATLAS barrel (a) and endcap (b) for L1 muon $p_T > 15$ GeV ('L1_MU15'). The fake rate (in red) is calculated by matching L1 muon candidates to an offline reconstructed muon within a cone $\Delta R = 0.4$.

the algorithm's run-time.
At first, muon candidates that are reconstructed at L2 have tracks which are entirely confined to the MS, which means that there is little rejection from the initial rate of fake muons seeded from L1. In order to reduce the number of fake tracks reconstructed as muon candidates a second-stage fast L2 algorithm is used to combine MS-only muon candidates with tracks reconstructed in the ID. This algorithm operates by extrapolating the MS track back to the Interaction Point using LUTs to reduce computing time. ID tracks within a specified η-ϕ window of the extrapolated track are sequentially combined with the extrapolated track. The p_T of the 'combined' muon track is calculated from the resolution-weighted average of the MS-only and ID track p_T. The track with the lowest χ^2 is selected as the muon candidate.

5.2.2 The EF muon trigger

The EF muon trigger uses modified versions of the offline algorithms detailed in Section 7.3 in order to maximise efficiency and resolution. The EF muon algorithms are seeded by RoIs identified by L1 and confirmed at L2. Two different algorithms operate at EF and will be described as *outside-in* and *inside-out*, which refer to the order in which a track is extrapolated and combined with the ID track from the external detector systems.

The *outside-in* algorithm constructs an MS track which is extrapolated to the IP to form an initial standalone MS-only muon track, with all of its properties determined by the information provided by the MS. The standalone muon is then combined with an ID track to form a combined muon. The *inside-out* algorithm operates by extrapolating the inner detector tracks with $p_T > 2$ GeV to the muon spectrometer. The algorithm then searches for muon hits in a road around the track in each chamber intersected by the track. Track 'segments' are constructed when hits are found. The extrapolation is improved by using information provided by the new segments. This procedure is intrinsically slower than the *outside-in* strategy. It should be noted that not all muons are simultaneously found by both of the algorithms.

Until the end of 2011, ATLAS used both of the EF muon strategies in paral-

lel. In 2012 the two algorithms were merged in order to minimise processing time. This was achieved by introducing a 'wrapper' algorithm with access to both strategies. The merged trigger algorithm operates by executing the *outside-in* algorithm and then, if no muon candidate is found, the *inside-out* algorithm. The result of the new trigger setup is that the highest efficiency for muon reconstruction at EF is obtained with minimal processing time. Figure 5.2 shows the total processing time of each of three strategies for the same L2 input; the new combined setup is referred to as 'mu24_tight' (black), the *inside-out* strategy is referred to as 'mu24_tight_MGonly' (red) and the *outside-in* strategy is referred to as 'mu24_tight_MuonEFonly' (blue). It is found that the execution time for the merged trigger algorithm is approximately $< 0.3\%$ slower than running the *outside-in* algorithm alone, and a factor of approximately 3.6 faster than running the two algorithms (*outside-in* and *inside-out*) in parallel.

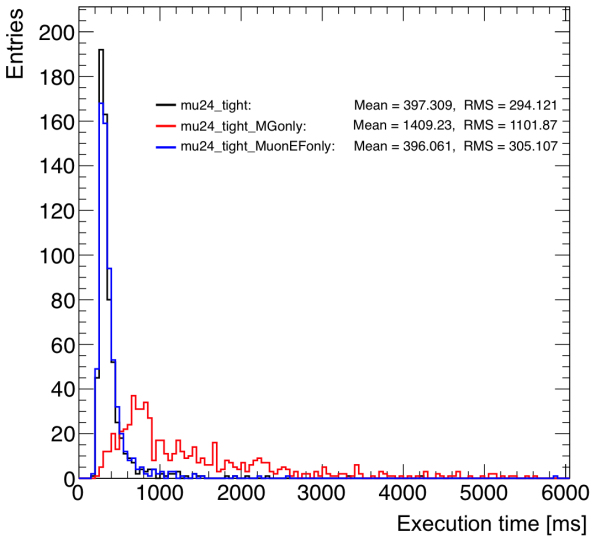

Figure 5.2: The total execution time of the two muon EF triggers, and the new combined setup. The new setup is referred to as 'mu24_tight' (black), the *inside-out* strategy is referred to as 'mu24_tight_MGonly' (red) and the the *outside-in* strategy is referred to as 'mu24_tight_MuonEFonly' (blue).

Figure 5.3 shows the HLT efficiency of the new setup compared to the standalone *inside-out* and *outside-in* strategies. The HLT efficiency is defined

as the combined EF + L2 muon trigger efficiency with respect to offline reconstruction for muons which have already passed L1. The result of the algorithm merger is an increase in the efficiency by approximately 1% with respect to the *inside-out* trigger.

As the EF trigger algorithms have access to ID track information it is possible to implement isolation criteria. This has the advantage of reducing the EF muon trigger rate, whilst rejecting muons from hadronic decays. The algorithm calculates the isolation variable by considering $(\sum p_T^{\mathrm{trk}})^{\Delta R<\Delta R^{\mathrm{cut}}}$, the sum of p_T of tracks (each requiring $p_T > 1$ GeV) found in the ID in a cone of size ΔR^{cut} centred around the muon. The isolation cut is defined by:

$$\frac{(\sum p_T^{\mathrm{trk}})^{\Delta R<\Delta R^{\mathrm{cut}}} - p_T^{\mu}}{p_T^{\mu}} < 0.12 \tag{5.1}$$

where p_T^{μ} is the muon candidate p_T. The efficiency loss due the isolation criteria at EF is $< 0.1\%$.

The total muon trigger efficiency is presented in Figure 5.4. The total efficiencies of the barrel and end-cap are $\sim 70\%$ and $\sim 90\%$ respectively, which are fundamentally limited by the geometrical acceptance of the trigger chambers.

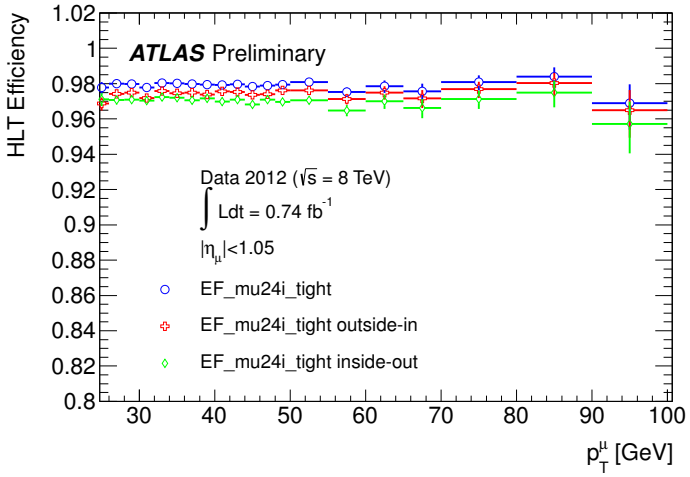

(a)

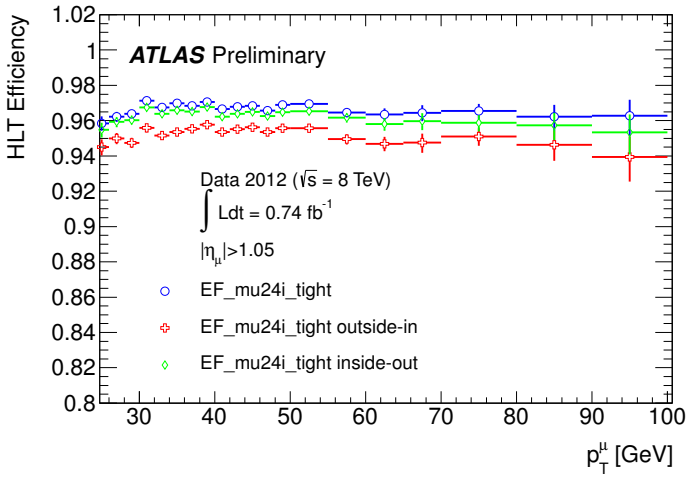

(b)

Figure 5.3: HLT muon trigger efficiency with respect to offline muons which are matched to a candidate passing L1 in (a) the barrel (b) the end-caps for isolated EF muon $p_T > 24$ GeV.

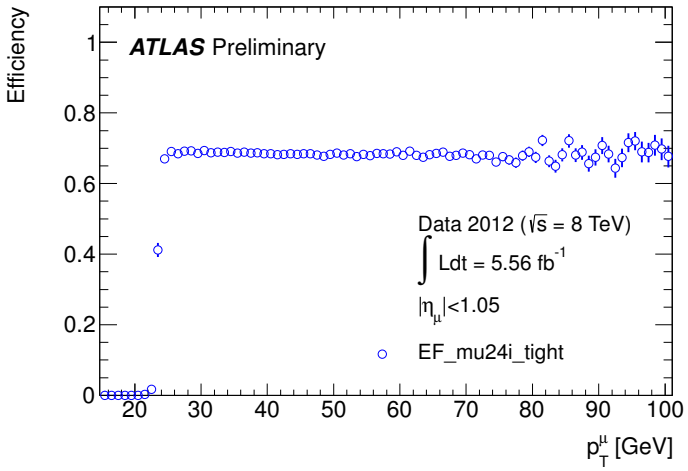

(a)

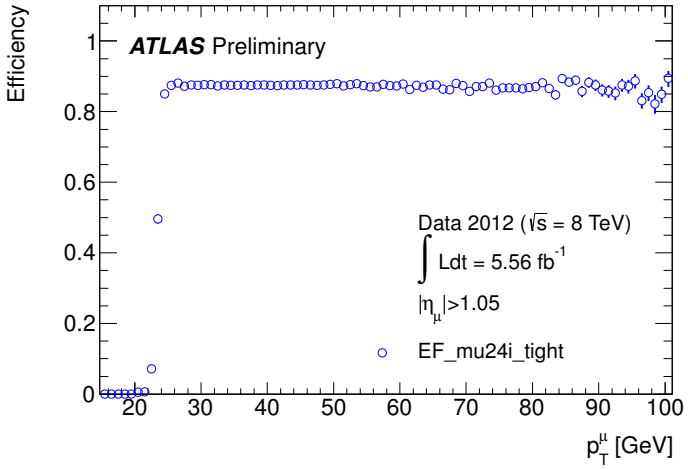

(b)

Figure 5.4: Muon trigger efficiency with respect to offline reconstruction in the barrel (a) and end-caps (b) respectively for isolated EF muon $p_T > 24$ GeV (`EF_mu24i_tight`).

5.3 Dataset and trigger nomenclature

The data used in this thesis was recorded by ATLAS in 2012 and corresponds to 20.3 fb^{-1} integrated luminosity of pp collisions with a centre of mass energy $\sqrt{s} = 8$ TeV.

As the final state of the signal presented in Section 3.5 contains two leptons, a set of triggers is chosen that selects events containing at least one lepton. The following triggers are considered in this thesis:

- electron triggers: `EF_e24vhi_medium1`, `EF_e60_medium1`;
- muon triggers: `EF_mu24i_tight`, `EF_mu36_tight`, `EF_mu18_tight_mu8_EFFS`.

The reasons for these choices of trigger are discussed in Sections 5.4.1 and 5.4.2. The names of the triggers can be decoded as follows, where 'PtCone20' is the scalar sum of ID track transverse momenta for cones about the trigger object $\Delta R = 0.2$:

- '`EF`' prefix on each of the triggers signifies that the event has passed an EF algorithm.
- For the electron trigger [53]:
  - '`e24`'('`e60`'): the event contains an electron candidate that has $p_T \geq 24(60)$ GeV, as calculated in the HLT stage.
  - '`vhi`'- The electron candidate has passed the following criteria:
    - At EF it is required that PtCone20/$p_T < 0.1$, where 'p_T' refers to the electron p_T.
    - At L1 the energy deposits outside of the core hadronic calorimeter signal are required to be ≤ 1 GeV.
  - '`medium1`'- The electron candidate must pass complex calorimeter criteria and additionally:
    - The transverse impact parameter must satisfy $d_0 < 5.0$ mm.
    - The electron track in the EM calorimeter and cluster must be matched to within some threshold in $\Delta\eta$.

- For the muon trigger:
  - 'mu24'('mu36', 'mu18', 'mu8'): the event contains an muon candidate that has $p_T \geq 24(36, 18, 8)$ GeV, as calculated in the HLT stage.
  - 'i': the muon candidate has passed a track isolation requirement at EF of PtCone20/$p_T < 0.12$.
  - 'tight': the muon candidate has passed at L1 a p_T cut of 15 GeV and has a three-station coincidence at L1.
  - 'EFFS ('EF full scan'): The chain has found multiple muons once a single trigger is confirmed. In the case of EF_mu18_tight_mu8_EFFS, a mu8 muon has been found after a EF_mu18_tight trigger is confirmed.

5.4 Analysis trigger selection

If one is to maximise the dataset available to be analysed for a specific signal it is important that a trigger is chosen that gives the maximum possible signal efficiency. As ATLAS has different triggers for events containing electrons and muons, the trigger selections for events containing electron and muons are presented separately. The trigger selections for events containing two muons, and one electron and one muon are presented in Section 5.4.1 and the trigger selection for events containing two electrons is presented in Section 5.4.2.

5.4.1 Muon trigger selection

The choice of trigger to select events with two muons in the final state is optimised for the highest signal efficiency with respect to the signal region cuts described in Section 8.2. It is assumed that background contributions are independent of trigger choice as the analysis selection cuts (including isolation requirements) are tighter than those at the trigger-level.

Muon trigger selection in $e\mu$ events

For events which require exactly one muon in the final state, the lowest p_T threshold trigger with the highest efficiency is given by the combination of triggers {EF_mu24i_tight or EF_mu36_tight}. For $e\mu$ events this is combined with the lowest threshold trigger combination in the electron channel such that the full trigger requirement is given by {EF_e24vhi_medium1 or EF_e60_medium1 or EF_mu24i_tight or EF_mu36_tight}.

Muon trigger selection in $\mu\mu$ events

If an event is required to contain exactly two muons then one can consider both single and dimuon triggers. The efficiency of heavy neutrino signal events with a dimuon final state, modelled with MC simulation as presented in Section 6.2, is measured as a function of heavy neutrino mass m_N with respect to each trigger. It is found for the lowest values of m_N ($\leq$ 120 GeV) that the dimuon trigger EF_mu18_tight_mu8_EFFS offers a higher signal efficiency than the combination of single muon triggers {EF_mu24i_tight or EF_mu36_tight}. This is shown by comparing the solid red line to the dashed red line in Figure 5.5. This is attributed to the lower average muon p_T in samples with $m_N \leq 120$ GeV compared to those with $m_N > 120$ GeV and that the dimuon trigger has a lower p_T threshold (18 GeV) compared to the single muon trigger (24 GeV).

For events with high muon p_T, which is the case for signal samples with heavy neutrino mass $m_N > 120$ GeV (and the majority of LRSM signal samples, described in Section 3.6), the dimuon trigger becomes less efficient with respect to the combination of single lepton triggers {EF_mu24i_tight or EF_mu36_tight}. This occurs because the single muon triggers (EF_mu24i_tight and EF_mu36_tight) operate with the merged muon trigger algorithm (Section 5.2.2) which runs the *outside-in* algorithm and then, if a muon is not found, the *inside-out*-type algorithm. The dimuon trigger only runs the *outside-in* algorithm, so a small inefficiency with respect to the single muon trigger is expected. The effect is quantified in Figure 5.6. The highest efficiency for all signal MC, as shown in blue in Figure 5.5, is obtained with the combination {EF_mu18_tight_mu8_EFFS or EF_mu36_tight}.

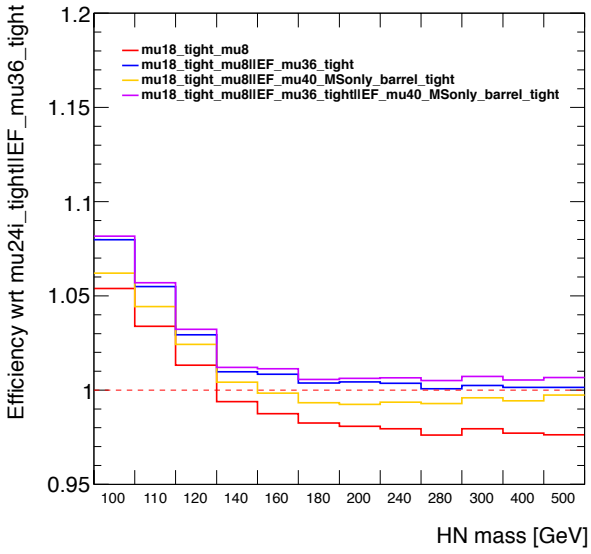

Figure 5.5: The efficiency of MC signal samples as a function of selected trigger, measured with respect to the efficiency measured using the trigger combination `EF_mu24i_tight` or `EF_mu36_tight`.

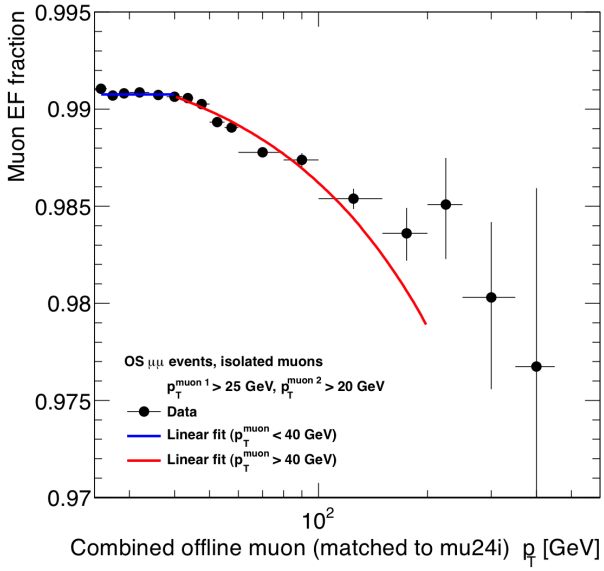

Figure 5.6: The fraction of muons matched to the trigger `EF_mu24i_tight` which were reconstructed with the *outside-in* (‘`TrigMuonEF`’) algorithm rather than the *inside-out* (‘`TrigMuGirl`’) algorithm, measured with respect to the combined offline muon p_T. The observed drop in `TrigMuonEF` fraction at high muon p_T is used to explain the signal efficiency drop at high muon p_T in the dimuon trigger `EF_mu18_tight_mu8_EFFS` which runs only `TrigMuonEF`.

5.4.2 Electron trigger selection

Whereas the L1 muon trigger is only approximately 70% efficient in the barrel, such that choice of trigger helps to recuperate efficiency losses, the L1 electron trigger is close to 100% efficient for electron $E_T > 25$ GeV so the choice of electron trigger does not increase data yields significantly. Studies within the heavy neutrino working group showed that there is no significant loss in efficiency compared to dielectron triggers when using the lowest p_T combination of single electron triggers {`EF_e24vhi_medium1` or `EF_e60_medium1`} to select dielectron events. This combination is used to select events in the *ee* channel.

Chapter 6

Monte Carlo simulation

The role of Monte Carlo (MC) simulation in this analysis is two-fold; to provide phenomenological modelling of heavy Majorana neutrino production and decay in ATLAS collisions, and to provide a prediction of the expected number of SM background processes that have the same final state as the signal. An important aspect of MC simulation is access to 'truth' information which details the complete decay chain of a process and also the true properties of particles before detector or object reconstruction effects. This makes it possible to measure biases or efficiencies of object selection cuts.

6.1 Monte Carlo event generation

MC event generators are used to simulate the dynamics, interactions and decays of a large number of particles. The probability distribution for a particular interaction and decay to occur is calculated using perturbation theory, with the incoming partons described by PDFs. The highest momentum-transfer process in the event, which is generally the interaction of interest, is referred to as the 'hard scatter' process. MC events are generated in a number of steps, which will be described here.

Event generation starts with the 'matrix element' calculation which represents the interaction probability amplitude. In general the matrix elements in this thesis have been generated at Leading Order (LO) in QCD meaning that no additional QCD radiation, which would be observed as a jet, is

generated in the hard-scatter process. Where Next-to-Leading Order (NLO) MC samples are used it implies that events have been generated by including the next-to-leading term in perturbation theory, which can lead to extra jets in the event. There are additionally LO MC generators which generate extra jets to form multi-parton final states without a full NLO calculation. These are referred to as 'multi-leg' generators.

The dynamics of incoming and outgoing partons due to QCD radiation are described by the 'parton shower' phase of event generation which is often implemented by a separate software package that is interfaced to the MC event generator. Parton showers evolve from the hard process and extend to a lower momentum scale by the continued emission of gluons, which are mainly soft. When a parton shower reaches a sufficiently low momentum scale then a hadronisation model is used which confines the partons into hadrons. After the hadronisation stage is implemented, unstable hadrons are subsequently allowed to decay.

It is important to also consider the 'underlying event', which is composed of the interactions between the remaining partons from the incoming protons, which evolve and hadronise. As jet cross-sections are steeply related to the jet p_T, even a small contribution from the underlying event can lead to a large change in the jet production rate and kinematics [54].

Generated events are then processed with a simulation of the ATLAS detector. The most thorough ATLAS simulation available uses the Geant4 framework [55], [56] which is able to simulate imperfections in the detector, subdetector alignment and inhomogeneities in the magnetic field. The MC generator Pythia [57] is used to reproduce additional proton-proton interactions in the event, which are overlaid on to the hard scatter process before detector simulation. As the full Geant4 simulation is relatively slow, simulation time can be reduced by an order of magnitude by using the Atlfast-II simulation [58]. Atlfast-II is a combination of fast and full simulation of the ATLAS detector; specifically the ID and MS are fully simulated with Geant4 whereas the calorimeter is simulated by parameterising MC events.

After simulation, the event is digitised so that the MC simulation data is in a format that be processed by ATLAS reconstruction software as described in Chapters 5 and 7. Each MC sample is assigned a weight w_{norm} to reproduce the number events from that interaction that one would expect to see given the interaction cross-section, σ, and the total integrated luminosity of the dataset, L:

$$w_{\text{norm}} = \frac{L}{N\sigma} \tag{6.1}$$

where N is the number of generated events.

6.2 Signal Monte Carlo

The MC simulation of heavy Majorana neutrino production and decay in the theoretical framework outlined in Sections 3.3 and 3.4 is described in this section. Events are produced using the `ALPGEN`-based `HvyN` package [59–61]. Like `ALPGEN`, `HvyN` is a LO event generator. The package allows the study of heavy Majorana neutrinos produced in association with charged leptons or neutrinos. In the case of the presented analysis, the production and decay of the heavy neutrino results in two leptons with the same-sign (SS) electric charge and two quarks in the final state. The leading-order Feynman diagram for the signal is shown in Figure 6.1.

Other than the heavy neutrino-lepton couplings $|V_{Nl}|^2$, which are taken from current best limits, the `HvyN` software package requires the user to input the desired heavy neutrino mass and whether the heavy neutrino-lepton interaction will conserve lepton flavour. This thesis considers the following values of heavy neutrino mass:

$$m_N \text{ [GeV]} = \{100,\ 110,\ 120,\ 140,\ 160,\ 180,\ 200,\ 240,\ 280,\ 300,\ 400,\ 500\}$$

and the final-state lepton flavour combinations from $\{ee,\ \mu\mu,\ e\mu\}$ where the the $e\mu$ combination explicitly violates lepton-flavour conservation. `HvyN` is interfaced to `Pythia` [57] for parton showering, underlying event and hadronisation modelling. A sample with $m_N = 200$ GeV is also generated which is

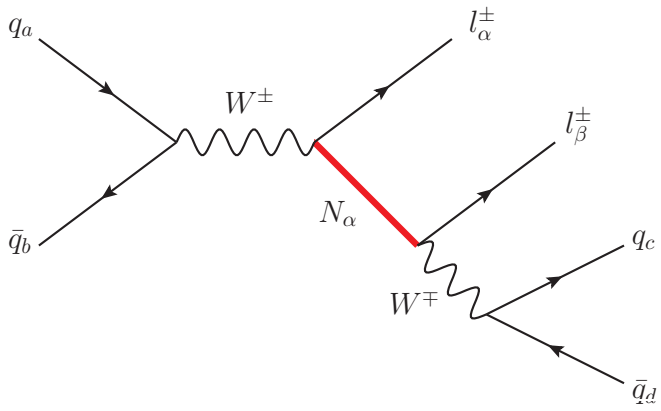

Figure 6.1: Production of a heavy Majorana neutrino N_α corresponding to lepton flavour α, where the final state contains SS leptons. If lepton flavour is conserved $\alpha = \beta$, otherwise $\alpha \neq \beta$. The W produced from the N decay is on-shell and, in this case, decays hadronically.

interfaced to HERWIG [62] for each of the three channels in order to evaluate a systematic uncertainty associated with the choice of parton shower. The Atlfast-II detector simulation is used for all samples. In addition, a sample with $m_N = 200$ GeV is generated with Geant4 for each of the three channels in order to evaluate a systematic uncertainty associated with fast simulation.

The kinematics of the generated signal events with two leptons and two jets in the $\mu\mu$ channel before detector simulation are presented in Figure 6.2. The invariant mass of the subleading-p_T lepton and two highest-p_T jets m_{ljj}, which reconstructs the mass of the heavy neutrino is shown in Figure 6.2 (a). As the heavy neutrino mass in the signal samples is at least 100 GeV, the W boson produced directly from the heavy neutrino decay is on-shell. Consequently the mass of the the two highest-p_T jets m_{jj} reconstructs to close to the W boson mass (approximately 80 GeV) as shown in Figure 6.2 (b).

Further details of the MC signal samples are given in Table 6.1 which also lists the ATLAS Dataset Identification (DSID) number, the number of generated events and the LO cross-sections, which are calculated by assuming the maximum values of $|V_{Nl}|^2$ allowed from experimental limits.

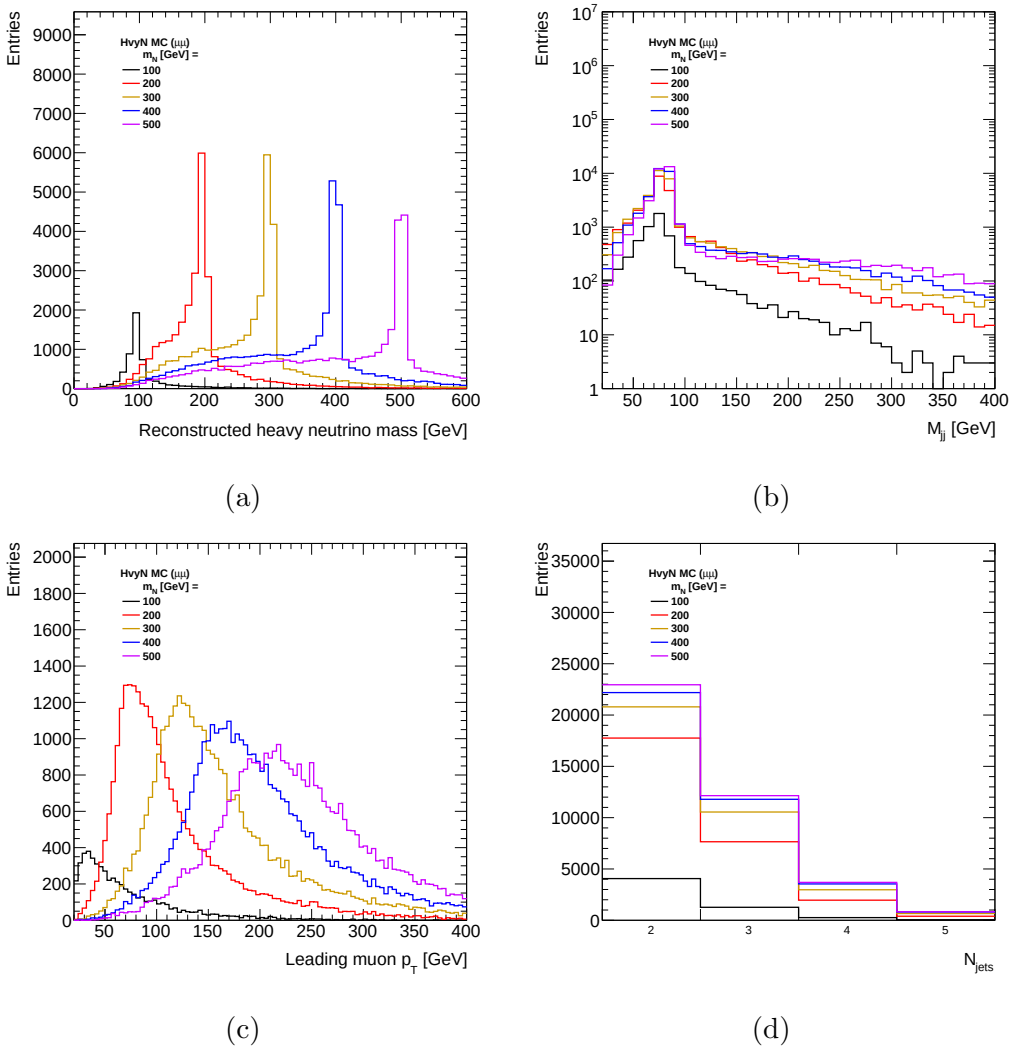

Figure 6.2: Kinematic distributions of the signal MC in the $\mu\mu$ channel, in events with two leptons and two jets. Both leptons and both jets are required to satisfy $p_T > 20$ GeV. There are 50000 events in each sample before the selection criteria is applied.

m_N [GeV]	Channel	LO σ [pb]	DSID	N_{MC}	Generator
100	ee	0.018201	158887	50000	HVYN + PYTHIA8
110	ee	0.010423	158888	50000	HVYN + PYTHIA8
120	ee	0.006706	158889	50000	HVYN + PYTHIA8
140	ee	0.003247	158890	50000	HVYN + PYTHIA8
160	ee	0.001710	158891	50000	HVYN + PYTHIA8
180	ee	0.001093	158892	50000	HVYN + PYTHIA8
200	ee	0.000711	158893	50000	HVYN + PYTHIA8
240	ee	0.000344	158894	50000	HVYN + PYTHIA8
280	ee	0.000188	158895	50000	HVYN + PYTHIA8
300	ee	0.000144	158896	50000	HVYN + PYTHIA8
400	ee	0.000046	158897	50000	HVYN + PYTHIA8
500	ee	0.000019	158898	50000	HVYN + PYTHIA8
100	$\mu\mu$	0.032358	158875	50000	HVYN + PYTHIA8
110	$\mu\mu$	0.018531	158876	50000	HVYN + PYTHIA8
120	$\mu\mu$	0.011922	158877	50000	HVYN + PYTHIA8
140	$\mu\mu$	0.005771	158878	50000	HVYN + PYTHIA8
160	$\mu\mu$	0.003110	158879	50000	HVYN + PYTHIA8
180	$\mu\mu$	0.001943	158880	50000	HVYN + PYTHIA8
200	$\mu\mu$	0.001264	158881	50000	HVYN + PYTHIA8
240	$\mu\mu$	0.000612	158882	50000	HVYN + PYTHIA8
280	$\mu\mu$	0.000334	158883	50000	HVYN + PYTHIA8
300	$\mu\mu$	0.000255	158884	50000	HVYN + PYTHIA8
400	$\mu\mu$	0.000082	158885	50000	HVYN + PYTHIA8
500	$\mu\mu$	0.000033	158886	50000	HVYN + PYTHIA8
100	$e\mu$	0.023299	158899	50000	HVYN + PYTHIA8
110	$e\mu$	0.013343	158900	50000	HVYN + PYTHIA8
120	$e\mu$	0.008582	158901	50000	HVYN + PYTHIA8
140	$e\mu$	0.004154	158902	50000	HVYN + PYTHIA8
160	$e\mu$	0.002303	158903	50000	HVYN + PYTHIA8
180	$e\mu$	0.001399	158904	50000	HVYN + PYTHIA8
200	$e\mu$	0.000909	158905	50000	HVYN + PYTHIA8
240	$e\mu$	0.000440	158906	50000	HVYN + PYTHIA8
280	$e\mu$	0.000240	158907	50000	HVYN + PYTHIA8
300	$e\mu$	0.000184	158908	50000	HVYN + PYTHIA8
400	$e\mu$	0.000059	158909	50000	HVYN + PYTHIA8
500	$e\mu$	0.000024	158910	50000	HVYN + PYTHIA8

Table 6.1: List of Type-I Seesaw Model samples. Cross-sections assume the maximum allowed coupling between the leptons and N.

6.3 Background Monte Carlo

MC simulation is used to provide a prediction for some of the expected backgrounds. The full background estimation is described in Chapter 9. The following MC samples are used specifically for background estimation:

- High statistics Drell-Yan events ($Z \to \ell\ell$) are generated with `Sherpa` [63].
- $t\bar{t}$ pair production is estimated using `MC@NLO+Jimmy` [64, 65].
- Backgrounds from WZ and ZZ production are estimated using MC samples generated with `Sherpa`. The contributions from both Z and virtual photons (γ^*) are included in both samples with the requirement $m(\ell\ell) > 0.1$ GeV. `Sherpa` additionally generates extra partons in the event.
- The contribution from $W^{\pm}W^{\pm} \to \ell^{\pm}\ell^{\pm}\nu\nu$ production is modelled using `MadGraph+Pythia` [66].
- Associated production of W and Z bosons with a $t\bar{t}$ pair are generated with `MadGraph+Pythia` [67, 68].
- The main contribution including a Higgs boson are from $H \to ZZ$, generated with `POWHEG+Pythia` [69] for both gluon-fusion and vector-boson fusion production modes.

Further details of the generated signal samples are given in Tables 6.2-6.4 which detail event and parton shower generators, the ATLAS DSID number, the number of generated events, the LO cross-section and the k-factor which accounts for NLO effects.

Process	LO σ [pb]	K-factor	DSID	N_{MC}	Generator
$Z \to ee$	1207	1.208	147770	30000000	SHERPA
$Z \to \tau\tau$	1207	1.208	147772	15000000	SHERPA
$(Z \to \mu\mu) + 0p$	712.1	1.229	107650	498999	ALPGEN+HERWIG+JIMMY
$(Z \to \mu\mu) + 1p$	154.8	1.229	107651	200000	ALPGEN+HERWIG+JIMMY
$(Z \to \mu\mu) + 2p$	48.88	1.229	107652	99500	ALPGEN+HERWIG+JIMMY
$(Z \to \mu\mu) + 3p$	14.20	1.229	107653	50000	ALPGEN+HERWIG+JIMMY
$(Z \to \mu\mu) + 4p$	3.802	1.229	107654	20000	ALPGEN+HERWIG+JIMMY
$(Z \to \mu\mu) + 5p$	1.109	1.229	107655	10000	ALPGEN+HERWIG+JIMMY

Table 6.2: List of MC samples for Z+jets production.

Process	LO σ [pb]	K-factor	DSID	N_{MC}	Generator
$t\bar{t}$ (lepton filter)	112.9	1.145	105200	14990603	MC@NLO+HERWIG+JIMMY
$t\bar{t}$ (hadronic decay)	95.12	1.144	105204	1199990	MC@NLO+HERWIG+JIMMY
$t\bar{t} + W$	0.1041	1.175	119353	399997	MADGRAPH+PYTHIA
$t\bar{t} + Wj$	0.09332	1.175	119354	399896	MADGRAPH+PYTHIA
$t\bar{t} + Z$	0.06769	1.34	119355	399996	MADGRAPH+PYTHIA
$t\bar{t} + Zj$	0.08734	1.34	119356	399895	MADGRAPH+PYTHIA
$t\bar{t} + WW$	0.0009190	1.00	119583	10000	MADGRAPH+PYTHIA

Table 6.3: List of MC samples for top production.

Process	Production mechanism	LO σ [pb]	K-factor	DSID	N_{MC}	Generator
$WW \to \ell\ell\nu\nu$	$q\bar{q}$	5.499	1.07	126892	2699994	SHERPA
$WZ \to \ell\nu\ell\ell$	$q\bar{q}$	9.751	1.06	126893	2699893	SHERPA
$ZZ \to \ell\ell\ell\ell$	$q\bar{q}$	8.740	1.11	126894	3799491	SHERPA
$ZZ \to \ell\ell\nu\nu$	$q\bar{q}$	0.4960	1.14	126895	899899	SHERPA
$WW \to \ell^{\pm}\ell^{\pm}\nu\nu$	VBF	0.070778	1.00	161981	199499	SHERPA
$ZZ \to \ell\ell\nu\nu$	VBF	0.001817	1.00	161982	100000	SHERPA
$WZ \to \ell\nu\ell\ell$	VBF	0.01322	1.00	161983	20000	SHERPA
$ZZ \to \ell\ell\ell\ell$	VBF	0.0009927	1.00	161984	499697	SHERPA

Table 6.4: List of MC samples for multi vector boson production. The production mechanisms '$q\bar{q}$' and 'VBF' refer to $q\bar{q}$ annihilation and vector boson fusion respectively.

Chapter 7

ATLAS object reconstruction and selection

ATLAS objects are collections of detector information that have been algorithmically refined in order to represent a physical particle or observable. This includes electrons, muons, jets and missing transverse energy which will be described in Sections 7.4 - 7.6. Additionally charged particles are expected to leave a 'track' in the ID section of the ATLAS detector, as described in Section 7.1, and all particles associated with the same decay are expected to have originated from a common Interaction Point or 'vertex', which are described in Section 7.2.

Object properties or kinematics are fully reconstructed after the ATLAS trigger system has accepted an event. The full reconstruction process is referred to as 'offline' reconstruction as there is no requirement to do this on the same timescale as the trigger algorithms. As a result the offline reconstruction implements complex algorithms that are able to reconstruct a particle with the highest degree of accuracy whilst rejecting background objects with selection cuts. There can be some overlap between reconstructed objects, but these can be rejected subsequently with additional selection cuts.

This chapter will describe the offline reconstruction process as well as the object selection cuts for the objects used in this analysis. Where simulation is used, the ATLAS detector is modelled in the Geant4 framework which,

as described in Chapter 6, is able to simulate imperfections, subdetector alignment and inhomogeneities in the magnetic field. An overview of reconstructed particles is shown in Figure 7.1.

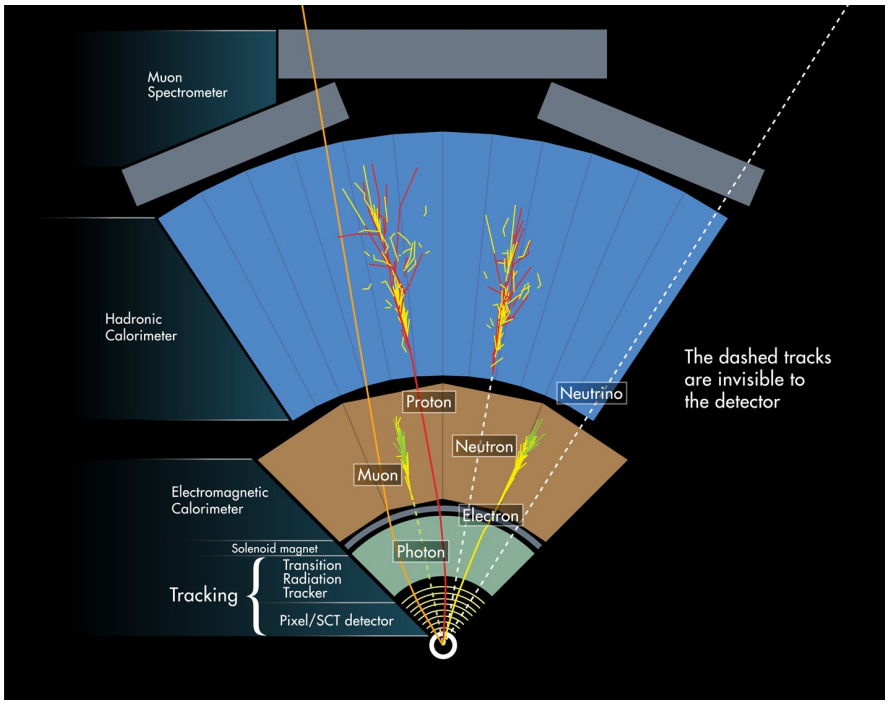

Figure 7.1: A summary of objects that are reconstructed by ATLAS offline algorithms, which overlap the respective subdetectors that are used in a wedge of the ATLAS detector [70].

7.1 Inner detector tracks

The tracks of charged particles are reconstructed using information provided by the ID system in the region $|\eta| < 2.5$. The reconstruction suffers from low efficiency at low particle momentum. This is due to significant energy losses resulting from material interaction which must be estimated by the track reconstruction algorithm. The ID track reconstruction operates in two sequences - *inside-out* and *outside-in* [71].

The primary ID pattern recognition follows the *inside-out* strategy, which is described here. The algorithm starts by creating a three-dimensional model

of the SCT and Pixel systems. In the case of the Pixel detector this is trivial as each module provides a two-dimensional measurement which is taken together with a beam-spot constraint to build a three-dimensional 'SpacePoint'. For the SCT detector the information provided by single SCT clusters is insufficient, so two adjacent SCT clusters are used to construct two-dimensional measurements. The SpacePoints are associated with each other by either using a fast primary vertex search to constrain pairs of SpacePoints, or by using a more time consuming method without such a constraint. Once the SpacePoint objects are built into track seeds, the directional information in the SpacePoint seeds is used to build roads of detector elements, along which tracks are fitted.

The silicon track building process results in a very high number of track candidates of which many are incomplete or describe fake tracks. The tracks are therefore ranked with a track-scoring system that uses track characteristics to award points or penalties. Sufficiently high-scoring tracks are extended to the TRT on a track-by-track basis which can later modify the selection of silicon hits by flagging them as outlier measurements. In the case of tracks coming from secondary decay vertices (such as from B-meson decays or from photon conversions) the track may not have enough silicon hits to achieve a sufficiently high score. The *outside-in* sequence is subsequently run to find these events, starting with a dedicated segment-finding algorithm in the TRT and a successive back-tracking of the segments into the silicon detector.

7.2 Vertex reconstruction

Vertex reconstruction is performed in two stages; the first is a primary vertex-finding algorithm, which associates ID tracks to the vertex candidates, and the second is a vertex-fitting algorithm which reconstructs the vertex position and refits tracks by constraining them to originate from the reconstructed interaction vertex [72]. Tracks in these methods are only considered if:

- $p_T^{\text{track}} > 150$ MeV,
- $|d_0| < 4$ mm,
- $\sigma(d_0) < 5$ mm,

- $\sigma(z_0) < 10$ mm,
- ≥ 4 hits in the SCT detector,
- ≥ 6 hits in the pixel and SCT detectors

where $\sigma(d_0)$ and $\sigma(z_0)$ denote the corresponding uncertainties of the track fit on d_0 and z_0. The latter requirements are optimised to remove tracks originating from secondary interactions.

7.3 Muons

Muons are reconstructed by the MS system and also independently by the ID offline reconstruction software as a charged track. The ID and MS muon objects have independently measured properties such as charge, p_T, η and ϕ. The ID and MS measurements are subsequently combined and the muon is refitted with new combined kinematics. Offline (MS + ID track) muon objects are reconstructed by the STACO algorithm [73], [74], [75], which is seeded by ID and MS-only tracks. The MS tracks are reconstructed with pattern recognition software in four stages:

1. Identify regions of activity (ROA), corresponding to regions of muon trigger chamber activity.
2. Reconstruct local straight segments in each muon station corresponding to an ROA.
3. Combine segments into muon track candidates.
4. Perform a global track fitting to the full MS system.

The MS track reconstruction also considers energy losses throughout the detector, which is most relevant for low p_T muons. The STACO combiner algorithm reconstructs combined muon objects by matching the reconstructed MS track with the ID track, using a statistical combination of the MS and ID track parameters. The p_T resolution of STACO combined muons, compared to MS-only and ID-only muons is presented in Figure 7.2. The STACO combination improves resolution particularly for muons with $p_T < 100$ GeV with respect to MS-only muon candidates. The ID track matching used in STACO combined muons allows for rejection of non-prompt muons from hadronic de-

cays, fakes tracks from beam-halo effects and 'punch-through' from high p_T jets.

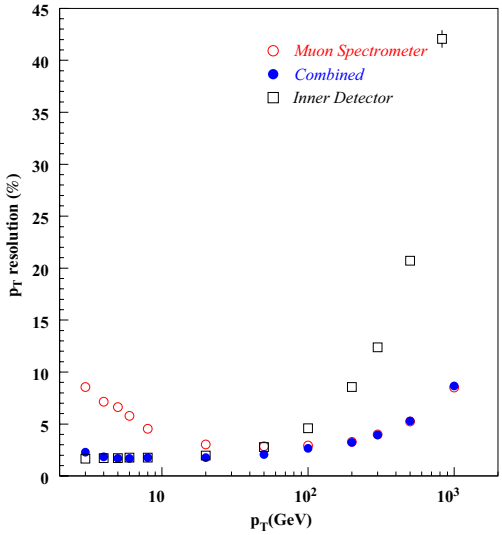

Figure 7.2: STACO muon p_T resolution as a function of STACO muon p_T for muons reconstructed with the MS, ID and combined MS + ID. The combined measurements improves the momentum resolution in the range $6 < p_T[\text{GeV}] < 100$ [74].

7.3.1 Object selection

Three quality points are defined for muons in this analysis, named *loose*, *medium*, and *tight*. A *loose* muon must satisfy the following criteria:

- Reconstructed by the STACO algorithm and passes the STACO 'loose' quality criteria. The STACO 'loose' criteria requires that the track is reconstructed with information from the Inner Detector and is also matched to track segments in the MS [76].
- The charge measured by the Muon Spectrometer and Inner Detector tracks must be of the same-sign in order to suppress backgrounds from charge mismeasurement.
- The muon must have $|\eta| < 2.5$.
- The muon must have $p_T > 10$ GeV.
- The inner detector track of the muon must satisfy the ATLAS Muon Combined Performance group (MCP) hit requirements [77].

A *medium* muon must satisfy the criteria for a *loose* muon, and additionally be reconstructed by STACO as a 'combined' muon. This means that the muon track is fully reconstructed in the MS and ID systems and a full combination is successfully performed. A *tight* muon satisfies the criteria for a *medium* muon and the following additional requirements:

- Muon $p_T > 20$ GeV.
- The muon impact parameters must satisfy: $|d_0| < 0.2\,\text{mm}$, $|z_0| < 2\,\text{mm}$, and $|d_0/\sigma(d_0)| < 3$.
- The muon must be isolated, as defined in Section 7.3.2.

7.3.2 Muon isolation optimisation

Isolation criteria for leptons in this analysis are a set of cuts applied to lepton objects in order to reject those categorised as 'non-prompt'. Non-prompt leptons are those originating from hadronic decays, and are described in more detail in Section 9.2. Compared to prompt leptons there can be a significant amount of residual event activity in the vicinity of a non-prompt lepton. This property is exploited by isolation criteria.

The muon isolation criteria are optimised using the signal MC samples describing the decays of heavy neutrinos N, which are detailed in Section 6.2. The signal MC used to describe heavy neutrinos in the LRSM model (Section 3.6) is also considered in order to share the optimisation for a separate analysis. The optimisation procedure considers the energy deposited in the calorimeter, EtConeX^{E_T}, and the scalar sum of ID track transverse momenta, PtConeX^{p_T}, for cones about the lepton ΔR^{E_T} and ΔR^{p_T} respectively where $\Delta R^i = \frac{X^i}{100}$ (and $\Delta R = \sqrt{\Delta\phi^2 + \Delta\eta^2}$). The isolation is optimised for dimuon events in terms of the number of events in a signal MC sample against the the total number of background events.

It is found for the LRSM case where $m_{W_R} \gg m_N$ that the efficiency to pass isolation cuts can be particularly low for small values of $\Delta R(\mu, \text{jet})$. In order to take this into account the isolation criteria differ at $\Delta R(\mu, \text{jet}) = 0.4$. For muons with no jet in a cone $\Delta R(\mu, jet) = 0.4$ it is required that:

- PtCone30 $< 0.05\ p_T$ for $p_T < 80$ GeV,
- EtCone20 $< 0.05\ p_T$.

For muons with a jet within cone $\Delta R = 0.4$ it is required that:

- $p_T > 80$ GeV,
- EtCone20 $< 0.05\ p_T + 1$ GeV or $|m(\mu j) - m(j)| > 10$ GeV

where the 'mass-drop' parameter $|m(\mu j) - m(j)|$ is used to recover some efficiency in the LRSM signal, as for large values of $|m(\mu j) - m(j)|$ it is indicative of boosted decay products rather than a hadronic decay.

7.4 Electrons

Electrons are reconstructed using the electromagnetic sliding-window clustering algorithm [78]. The algorithm starts by building 'towers' of electromagnetic calorimeter cells defined by a size $\Delta\eta \times \Delta\phi$ which results in a grid of towers in $\eta - \phi$ space. The energy of all cells in all longitudinal layers in this volume is then summed into the 'tower energy'. A window of a fixed number of towers is moved across each tower in the grid. If the sum of the transverse energy of the towers in the window is a local maximum (above a minimum threshold) then a precluster is formed. After duplicate preclusters are rejected, calorimeter cells are assigned to EM clusters by taking all cells in a rectangle centred on a precluster [79]. The region $1.37 < |\eta| < 1.52$ is excluded due to poor coverage.

ID tracks are matched to EM clusters in electron reconstruction in order to separate electron candidates from photons (and also QCD jets, if one considers $\pi^0 \to \gamma\gamma$ decays). Further separation is achieved by implementing quality criteria. Three levels of electron quality are considered in this analysis; **Loose++**, **Medium++** and **Tight++** which are a set of one-dimensional cuts on a number of discriminating variables. The discriminating variables are [80]:

- The EM shower shapes.
- The matching of track-cluster η.

- The number of SCT, pixel and b-layer hits and on the transverse impact parameter d_0.
- The matching of angular and energy-momentum between the calorimeter and inner detector. For electrons the momentum is required to closely match the energy.
- The sum of p_T about the inner detector track and the sum of E_T about the EM cluster in a cone of radius $\Delta R = \sqrt{\Delta\eta^2 + \Delta\phi^2}$.

7.4.1 Object selection

In addition to the quality levels defined in the offline reconstruction, three quality points for electrons are defined for this analysis- *very-loose*, *medium* and *tight*. The term 'loose' is reserved for the sample of electrons that is used for studying the non-prompt background in Section 9.2. For *very-loose* electrons, the following criteria must be satisfied:

- Electrons should satisfy **Loose++** requirements.
- An electron's calorimeter cluster should satisfy the condition $|\eta| < 2.47$, excluding the crack region.
- The transverse energy of the calorimeter cluster is required to satisfy $E_T > 10$ GeV.

A *medium* electron is defined as a *very-loose* electron which also satisfies the **Medium++** requirements. A *tight* electron is defined as a *medium* electron with several addition requirements:

- Electrons must satisfy the **Tight++** criteria.
- Electrons must pass a set of requirements on the impact parameters: $|d_0| < 0.2$ mm, $|z_0| < 2$ mm, and $|d_0|/\sigma(d_0) < 3$.
- The transverse energy is required to satisfy $E_T > 20$ GeV.
- Electrons must be isolated, defined as follows:
  - PtCone20 + 1 GeV $< 0.05\ p_T$, and
  - EtCone30 $< 0.05\ E_T$.

7.5 Jets

In this analysis jets are constructed according to the *anti-k_T* algorithm [81,82] with a cone-size parameter of $\Delta R = 0.4$. The *anti-k_T* algorithm is collinear safe and infrared safe, meaning that if an event is modified by a collinear splitting or the addition of a soft emission, the set of hard jets in the event are unchanged. The jet algorithm is seeded by topological clusters which have been calibrated according to the response of electrons to the LAr and Tile calorimeters.

Topological clustering aims to group neighbouring calorimeter cells into clusters that have energies that are sufficiently above an expected noise threshold. Cluster growth starts with seed cells, which are calorimeter cells that pass a minimum threshold energy significance condition. Seed cells are selected consecutively to form a 'proto-cluster' and the following steps are repeated until all seed cells have been assigned to a proto-cluster:

- If neighbouring cells have an energy significance above a low threshold they are added to the proto-cluster.
- If the latter cells also have an energy significance above a medium threshold they act as an additional seed to expand the cluster.
- If a cell is adjacent to more than one proto-cluster, and would pass either of the previous criteria then the proto-clusters are merged.

After these steps, the remaining proto-clusters are only accepted as 'clusters' if they have an E_T above a minimum threshold. The energy of the jet is corrected for detector effects and the response of the calorimeter to hadrons by considering the following:

- the energy deposited outside of the calorimeter,
- the energy deposited outside active detector regions,
- inefficiencies in the jet reconstruction and clustering.

7.5.1 Jet vertex fraction

The high instantaneous luminosity at ATLAS results in a large number of pp collisions per bunch crossing. Consequently, a considerable fraction of jets in events recorded by ATLAS are from the additional pile-up interactions and not the vertex associated with the 'primary' interaction. The Jet Vertex Fraction (JVF) discriminant quantifies the fraction of track transverse momentum associated with a jet from the interaction vertex [83]:

$$\mathrm{JVF}(\mathrm{jet}, v_j) = \frac{\sum_k p_T^{\mathrm{track}_k}(v_j)}{\sum_n \sum_p p_T^{\mathrm{track}_p}(v_n)} \tag{7.1}$$

where p_T^{track} is the track momentum, v_j is the primary vertex, and v_n are all vertices in the event. The JVF distribution for jets from simulated QCD dijet events is presented in Figure 7.3 which demonstrates that the JVF of jets from pile-up peaks at zero, whereas jets from the hard-scatter peak at one. Following various studies [84–86], this analysis requires that the JVF of jets to be $> 50\%$ for jets with $p_T < 50$ GeV and $|\eta| < 2.4$.

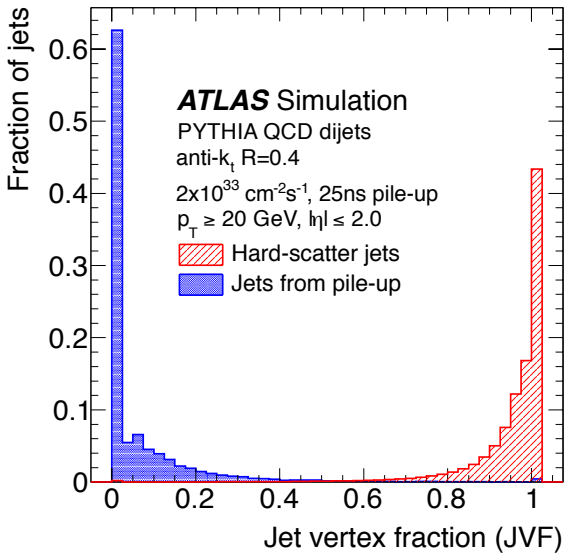

Figure 7.3: The fraction of jets from pile-up (blue) and the hard-scatter (red), confirmed with MC truth information (which is described in Chapter 6), as a function of Jet Vertex Fraction (JVF).

7.5.2 Jet object selection

Two qualities of jets are defined, referred to as *loose* and *tight*. A *loose* jet is any jet reconstructed as described in Section 7.5. An 'overlap removal' is performed for *loose* jet and *very-loose* electron candidates to avoid double counting electrons as jets. This requires the removal of the nearest *loose* jet j which has $\Delta R(e,j) < 0.2$ and $p_T^j < 2E_T^{\mathrm{e}}$ from each *very-loose* electron e. After overlap removal a final selection is applied to obtain the *tight* jets which must additionally satisfy the following:

- $p_T > 20$ GeV
- $|\eta| < 2.8$
- For $p_T < 50$ GeV and $|\eta| < 2.4$ it is required that $|\mathrm{JVF}| > 0.5$.

7.6 Missing transverse energy

The E_T^{miss} in an event is defined as the vector momentum imbalance in the transverse plane. It is obtained from the negative of the vector-sum of the energy in the transverse plane of all particles detected in a pp collision [87]. In SM interactions a true source of E_T^{miss} from particle decays is the presence of light neutrinos which lead to a momentum imbalance as neutrinos pass through the detector unimpeded. There are also contributions from the detector resolution and the geometric acceptance of the detector, particularly considering the presence of dead regions and sources of noise, cosmic rays and beam-halo effects.

E_T^{miss} is reconstructed in x and y components by considering contributions from energy deposited in the calorimeters $(E_{x(y)}^{\mathrm{miss}})^{calo}$ and from muons in the MS $(E_{x(y)}^{\mathrm{miss}})^{\mu}$:

$$E_{x(y)}^{\mathrm{miss}} = (E_{x(y)}^{\mathrm{miss}})^{calo} + (E_{x(y)}^{\mathrm{miss}})^{\mu} \tag{7.2}$$

and the values of E_T^{miss} and corresponding azimuthal coordinate ϕ^{miss} are

calculated from:

$$E_T^{\text{miss}} = \sqrt{(E_x^{\text{miss}})^2 + (E_y^{\text{miss}})^2} \tag{7.3}$$

$$\phi^{\text{miss}} = \arctan(E_x^{\text{miss}}, E_y^{\text{miss}}). \tag{7.4}$$

The calorimeter term $(E_{x(y)}^{\text{miss}})^{calo}$ in Equation 7.2 is calculated by associating calorimeter cells to reconstructed electrons (e), photons (γ), taus (τ), jets, muons (μ) and additional energy deposits (`CellOut`):

$$\begin{aligned}(E_{x(y)}^{\text{miss}})^{calo} = (E_{x(y)}^{\text{miss}})^{e} \quad + (E_{x(y)}^{\text{miss}})^{\gamma} \quad + (E_{x(y)}^{\text{miss}})^{\tau} \quad + \\ (E_{x(y)}^{\text{miss}})^{\text{jets}} + (E_{x(y)}^{\text{miss}})^{\mu,calo} + (E_{x(y)}^{\text{miss}})^{\texttt{CellOut}}\end{aligned} \tag{7.5}$$

where each term is calculated from the negative of the vector-sum of calibrated cell energies in each object. The $(E_{x(y)}^{\text{miss}})^{\mu,calo}$ term in Equation 7.5 is due to energy deposited by muons in the calorimeter system. The $(E_{x(y)}^{\text{miss}})^{\texttt{CellOut}}$ term is calculated from cluster of cells which are not otherwise reconstructed as any other offline object. In order to suppress noise, the $(E_T^{\text{miss}})^{calo}$ sum only considers cells belonging to topological clusters, unless they are associated with electrons or photons.

The $(E_{x(y)}^{\text{miss}})^{\mu}$ term in Equation 7.2 is calculated from the negative of the sum of momenta of muon tracks reconstructed with $|\eta| < 2.7$ in order to account for muon energy losses not included in $(E_{x(y)}^{\text{miss}})^{\mu,calo}$. A muon in the region $|\eta| < 2.5$ is only accepted if its MS track is matched in the ID in order to reduce fake contributions.

7.7 Corrections to simulation

To provide reliable predictions it is necessary to apply corrections so that MC is in good agreement with data in control samples of events which are experimentally well understood. These corrections will be discussed here, with the exception of the correction applied to events with a lepton charge-flip, which is discussed in Section 9.3.

Reconstruction and detector effects in simulated events can be corrected by

applying scale factors to MC events. The scale factors are calculated as the ratio of efficiencies measured in data and MC. Importantly using scale factors cancels phenomenological dependencies in the sample in which the efficiencies are measured.

7.7.1 The Tag-and-Probe Method

A common technique used to measure the efficiency of prompt leptons with respect to some quality criteria is known as the Tag-and-Probe Method. In this analysis it is used in the measurements of the lepton isolation efficiency, the prompt lepton efficiency and the charge-flip rate of prompt leptons. Crucially, the procedure requires a pure sample of prompt leptons so that the measured efficiencies are free of phenomenological biases. This is achieved by requiring events to contain two leptons of the same flavour and OS electric charge which have a dilepton mass close to the mass of the Z boson. These criteria are satisfied by events that are dominated by Z boson decays. Labelling (in any order) the two leptons as l_1 and l_2, the Tag-and-Probe Method is executed as follows for some additional set of criteria C:

1. If l_1 satisfies C, then l_1 is a 'tag' and l_2 is a 'probe'.
2. If l_1 is a tag, test whether the probe l_2 passes or fails C.
3. Repeat this process by exchanging the roles of l_1 and l_2.

After processing this for n_T tag leptons, the Tag-and-Probe efficiency ϵ_{TaP} is given by:

$$\epsilon_{\text{TaP}} = \frac{n_P}{n_T} \tag{7.6}$$

where n_P is the number of probes that have passed C. It should also be noted that the criteria C can differ for tag and probe leptons. Reconstruction and detector effects tend to vary strongly with a lepton p_T or η, so ϵ_{TaP} is often parameterised to reflect this.

7.7.2 Energy and momentum corrections

Muon momentum resolution and scale corrections

The momentum resolution of muon tracks is corrected by applying a Gaussian smearing function using factors provided by the ATLAS Muon Combined Performance group (MCP) [77]. The resolution correction factors have been derived by comparing the dimuon mass resolution measured in experimental and simulated data. Corrections to the momentum scale are derived from the peak position of the Z resonance peak after application of momentum smearing to the MC. Scale corrections to the ID and MS momentum measurements are consistent within $< 0.1\%$. Systematic uncertainties are also provided by the same study.

Electron energy resolution and scale corrections

Energy scale and resolution correction factors are applied to correct the electromagnetic cluster energy using a software package provided by the ATLAS E/gamma Performance group [88]. The energy resolution and scale correction factors are obtained from resonances such as $Z \to ee$ and $J/\psi \to ee$. The corrections are consistent within $< 1\%$ uncertainty.

7.7.3 Lepton efficiency corrections

A scaling is applied to MC events in order to match the efficiency of leptons measured in data to pass all trigger and offline object selections. For every lepton in a selected MC event, the event is reweighted according to scale factors that are calculated as the ratio {data : MC} of efficiencies which are parameterised primarily in terms of lepton p_T. The total efficiency ϵ_{tot} is factorised into three components as follows:

$$\epsilon_{\text{tot}} = \epsilon_{\text{reco}}\ \epsilon_{\text{ID}}\ \epsilon_{\text{tight}} \tag{7.7}$$

where ϵ_{reco}, ϵ_{ID} and ϵ_{tight} refer to the efficiencies due to the offline reconstruction, lepton identification and the tight lepton selection respectively. The measurement and implementation of these three components is discussed in this section.

A single identification and reconstruction efficiency ($\epsilon_{\text{ID}} \times \epsilon_{\text{reco}}$) for muons with a combined (ID + MS) track is provided by the ATLAS MCP group. The efficiency is measured with the Tag-and-Probe method (Section 7.7.1), using events with two isolated muons with OS electric charge. Both muons are required to have $p_T > 20$ GeV and a dimuon mass within 10 GeV of the Z boson mass. All tag muons are required to have a combined (ID + MS) track. The muon identification efficiency is measured by testing probe muons with a MS track for the existence of a matching ID track. The muon reconstruction efficiency is measured by using probe muons which have an ID track and are identified as a minimum ionising particle in the EM calorimeter, and testing whether each probe also has a combined (ID + MS) track. The efficiencies measured in data and MC are $> 98\%$ and the differences between the efficiencies are $< 1\%$ [89].

The reconstruction and identification efficiencies for electrons are calculated using $Z \to ee$ events with the Tag-and-Probe method. All electrons in the measurement are required to be reconstructed as sliding-window EM clusters with a matching track, as described in Section 7.4. Tag electrons are those with $E_T > 20$ GeV, pass the **Tight++** criteria and are matched to a single- electron trigger object. In order to measure the reconstruction efficiency, tag electrons must additionally satisfy $20 < E_T$ [GeV] < 50 and the 'track-quality criteria' defined for cluster ID tracks that have at least one Pixel hit and at least seven hits in the combined Pixel and SCT system. Probe electrons are then required to pass the track-quality criteria. For the electron identification efficiency, both tag and probe electrons must pass the track-quality criteria. The probes are required to have $E_T > 15$ GeV and OS electric charge with respect to the tag electron and must additionally pass the **Tight++** criteria. The reconstruction and identification efficiencies for electrons are measured to be $> 97\%$ and $\sim 80\%$ respectively. The reconstruction efficiency is measured in data and MC to be within 1%. The electron identification efficiency scale factors in data and MC are within 3%. [90].

The tight lepton selection efficiency ϵ_{tight} is defined as the Tag-and-Probe efficiency for leptons to pass the *tight* lepton criteria with respect to some looser criteria. For the case of muons, the looser criteria are the *loose* muon

selection cuts, and for electrons they are the *medium* electron criteria. The efficiencies are measured using events containing exactly two leptons from ee and $\mu\mu$ which have an invariant mass within 10 GeV of the Z boson mass.

For electrons, the ϵ_{tight} scale factors have been parameterised in p_T and η as a function of the number of jets in the event. The corresponding electron selection scale factors are typically > 0.95. The corresponding systematic uncertainties, which are approximately 3%, are estimated by considering the variation of the scale factors as a function of μ, η, ϕ, p_T and number of jets in the event. The statistical uncertainties associated with the scale factors are approximately 0.5% and 4% for events with less than two jets and at least three jets respectively.

The efficiencies for *loose* muons to pass the *tight* criteria in events with zero to five jets respectively are shown in Figure 7.4. The isolation efficiency scale factors increase from approximately 0.9 to 1 between muon $p_T = 20$ GeV and $p_T = 80$ GeV. For muon $p_T > 80$ GeV the *tight* isolation criteria are loosened to allow muons to be close to jets, so the efficiencies and scale factors in this region are approximately one. For this reason the absolute efficiencies presented in Figure 7.4 are discontinuous at muon $p_T = 80$ GeV, which is more pronounced for events with multiple jets where the muons are increasingly likely to overlap with a jet. The importance of using scale-factors of efficiencies is highlighted here as the shape of the distributions, which is produced in data and MC, is cancelled by the use of scale factors. The uncertainties in the scale factors are estimated by considering the variation of the scale factors as a function of μ, η and ϕ. A fitting function is used to describe the scale factors, shown in Figure 7.4 with an uncertainty of approximately 3%.

Lepton trigger scale factors are applied to Monte Carlo as recommended by the ATLAS MCP group [91]. The trigger efficiencies ϵ_{trig} are measured with respect to reconstructed leptons. The scale factors correct for differences in the trigger efficiency measured in data and MC, which are typically $< 1\%$ with an uncertainty of $< 1\%$.

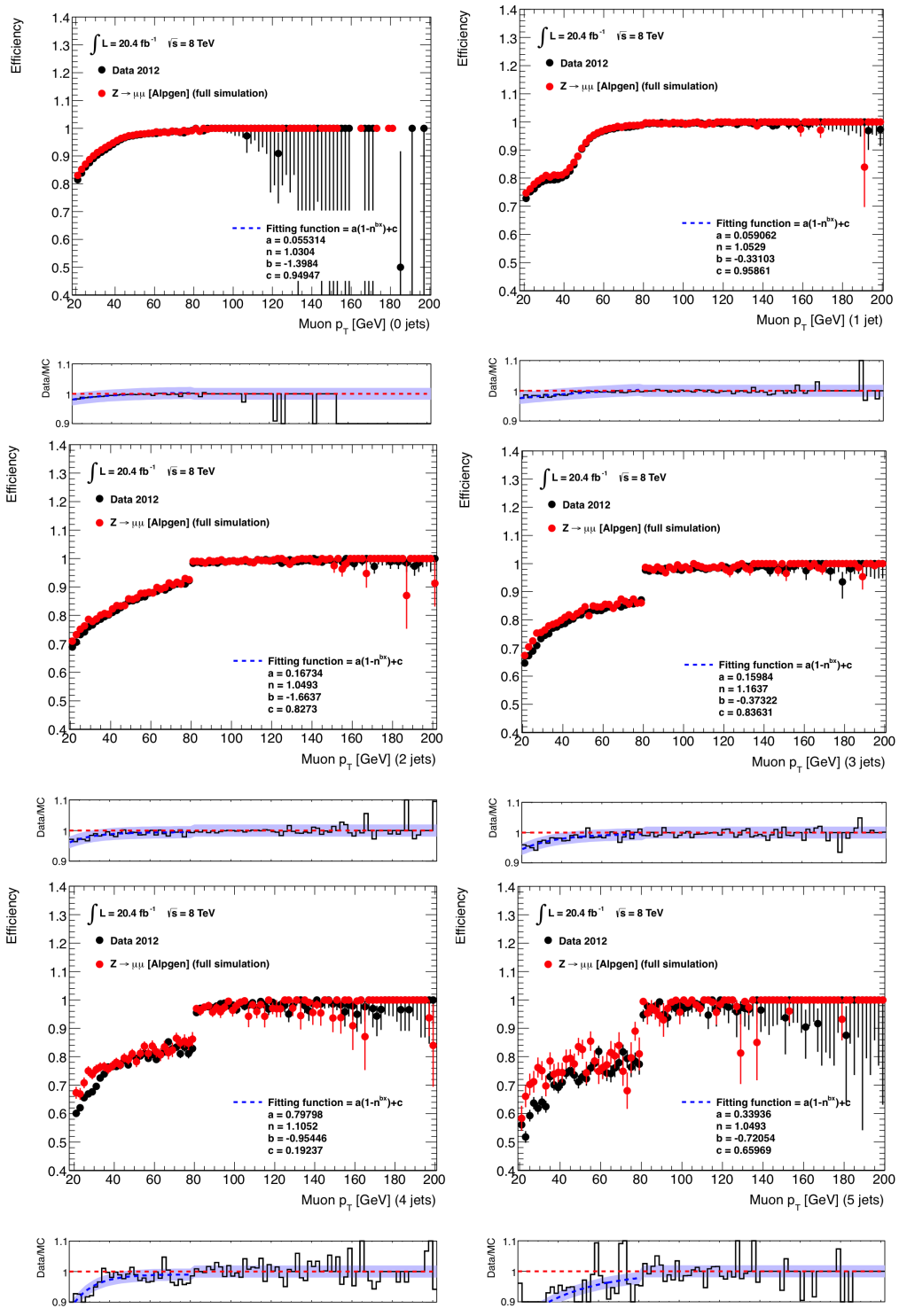

Figure 7.4: The *tight* muon object selection efficiency (top of each figure) for data and MC and data-to-MC scale factors (bottom of each figure). A fitting function is used below 80 GeV, with an error band (in purple) given by the variation in the scale factor with respect to μ, η and ϕ .

Chapter 8

Event selection

This chapter will describe the event selection procedure that is used in this analysis. Section 8.1 describes the ATLAS dataset that is presented in this thesis. Section 8.2 presents a general event selection which is the basis for the control regions described in Chapter 11. The signal selection presented in Section 8.3 aims to maximise sensitivity to the heavy neutrino decay by selecting events which exploit the signal's characteristics whilst rejecting SM backgrounds.

8.1 Dataset selection

The data used in this thesis were collected by ATLAS during the 2012 run of proton-proton collisions at $\sqrt{s} = 8$ TeV. To avoid any data integrity errors and to ensure the stability of detector systems operation, this analysis uses events that feature in the official standard ATLAS 'Good Run List' (GRL). The GRL removes events from data-taking intervals which may be unreliable, for example due to detector defects. The total integrated luminosity after GRL selection is 20.3 fb^{-1}.

ATLAS event data are categorised into 'streams' according to the type of trigger which the events have passed. As the signal contains leptons in the final state, this analysis uses events in the electron-stream or the muon-stream and takes into account any overlap of events between the streams.

8.2 General event selection

Unless otherwise stated all events used in this analysis must have exactly two leptons that adhere to the following selection criteria. The quality categories '*very-loose*', '*loose*', '*medium*' and '*tight*' are defined in Chapter 7. All leptons are required to be *tight* leptons of either electron or muon flavour. The leading p_T lepton must satisfy $p_T \geq 25$ GeV and all other leptons must have $p_T \geq 20$ GeV. There must be no additional *medium* leptons in the event. If any *very-loose* electron is the Inner Detector segment of any *loose* muon, then the event is rejected. Tracks associated with the leptons are required to be matched to the same vertex. All jets are required to be *tight* and satisfy $p_T > 20$ GeV.

Events are required to have passed the following triggers:

- ee channel: `EF_e24vhi_medium1` or `EF_e60_medium1`
- $e\mu$ channel: `EF_e24vhi_medium1` or `EF_e60_medium1` or `EF_mu24i_tight` or `EF_mu36_tight`
- $\mu\mu$ channel: `EF_mu18_tight_mu8_EFFS` or `EF_mu36_tight`

which are selected after considering the study presented in Chapter 5. The trigger objects are also required to be matched to an offline lepton within $\Delta R = 0.1$.

8.3 Signal event selection and optimisation

Signal events must be selected in a manner that discriminates signal-like events from background processes whilst maximising the efficiency of the signal. This requirement is quantified by optimising the number of signal events against the number of expected background events. Background processes refer to those which lead to the same final state as the signal, and are presented in detail in Chapter 9. The first requirement for signal events is that they must contain two leptons and at least two jets.

Due to the Majorana nature of the neutrino in the Seesaw Mechanism both of the scenarios where two leptons with OS or SS electric charge are in the final states are permitted, according to the decay presented in Section 3.5. Performing the search using events with OS dilepton final states is strongly disfavoured as SM backgrounds produced via gluon-gluon fusion or quark-anti-quark annihilation have final states that are intrinsically electrically neutral. This leads to an irreducibly large background in a search for a low-yield process. For this reason two SS leptons are required in the final state.

A signal event selection optimisation is quantified by studies presented in [92]. The signal event selection is optimised for events with SS leptons by considering cuts on the following variables:

The dilepton invariant mass, $m_{\ell\ell}$
A cut on $m_{\ell\ell}$ is used to suppress backgrounds due to low mass QCD resonances that enter into the non-prompt background calculation presented in Section 9.2. The cut is optimised for signal significance and it is found that requiring $m_{\ell\ell} > 40$ GeV offers good signal efficiency, even for the lowest mass heavy neutrino MC sample ($m_N = 100$ GeV). The $m_{\ell\ell}$ distribution of the signal and expected background are presented in Figure 8.1 for events containing two SS electrons. The arrows in Figure 8.1 indicate the region that is retained after the cut is applied.

The dielectron invariant mass, m_{ee}
In the ee channel there is a significant background from the mismeasurement of electron charge as described in Section 9.3, which leads to OS electron pairs being accepted in the SS selection. The dominant source of OS electron pairs is from the decay of Z bosons which are characterised as having m_{ee} close to the mass of the Z boson, $m_Z \approx 90$ GeV. Therefore a cut on the dielectron invariant mass can be used to suppress Z decays by removing events with $|m_{ee} - m_Z| < 20$ GeV. The m_{ee} distribution of the signal and expected background is presented in Figure 8.1d, where the arrows indicate the region that is retained after the cut is applied. The events used in this distribution are required to contain two SS electrons and two jets.

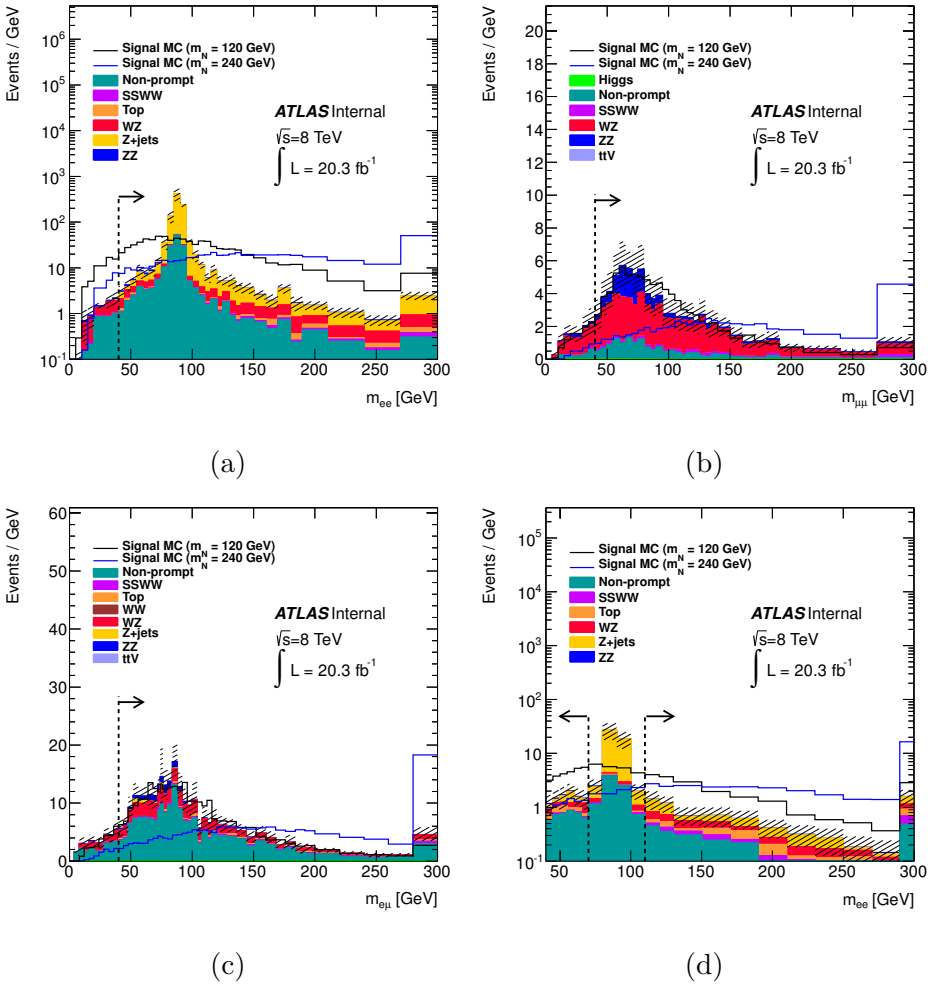

Figure 8.1: The invariant mass of lepton pairs in events with two SS leptons for signal MC and expected background in (a) the ee channel, (b) the $\mu\mu$ channel and (c) the $e\mu$ channel. Figure (d) shows events with two electrons, two jets and $m_{ee} > 40$ GeV. The total number of signal MC events are normalised to the number of predicted background events. The area indicated by the arrows is retained after the signal selection cut is applied.

The missing transverse energy, E_T^{miss}

As there are no prompt light neutrinos in the final state of the signal there is low E_T^{miss} in signal events. Any residual E_T^{miss} in the signal events is due to the E_T^{miss} resolution and the geometric acceptance of the detector. By requiring events to have E_T^{miss} below a threshold it is possible to suppress backgrounds such as $WZ \to \ell\nu\ell\ell$ with neutrinos in the final state. A cut of $E_T^{\text{miss}} < 40$ GeV is chosen, indicated by arrows in Figure 8.2, which shows events containing two SS leptons and two jets. In the ee channel there is additionally a requirement on the dielectron mass of $|m_{ee} - m_Z| > 20$ GeV.

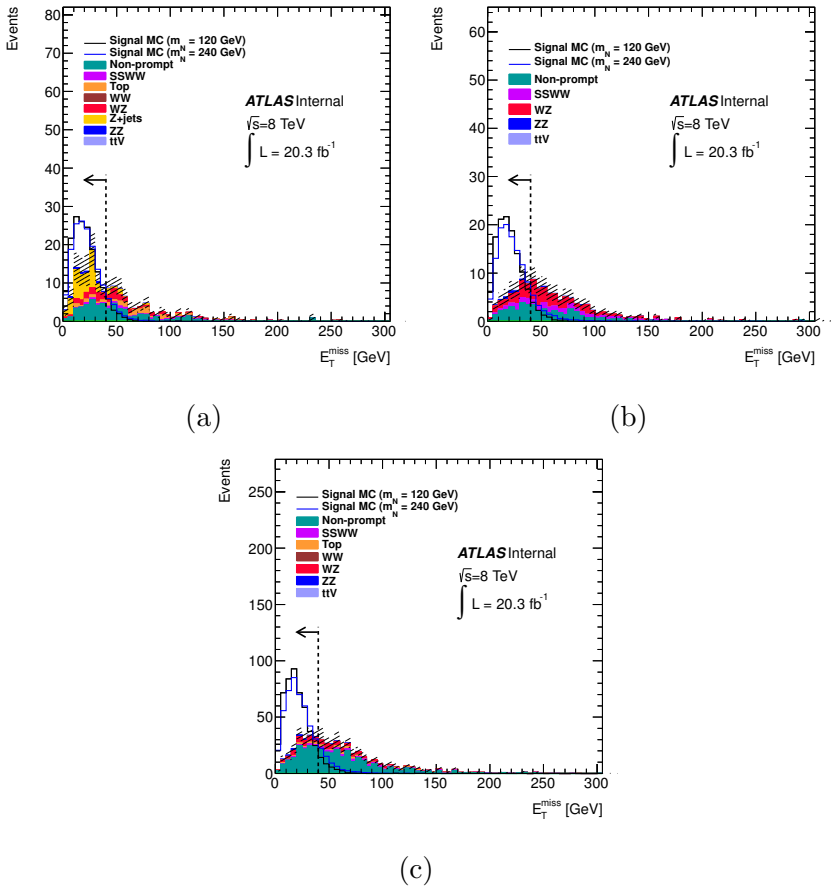

Figure 8.2: The E_T^{miss} distribution in events with two SS leptons and two jets for signal MC and expected background, for the (a) ee channel, (b) $\mu\mu$ channel and (c) $e\mu$ channel. Additionally in the ee channel it is required that $|m_{ee} - m_Z| > 20$ GeV. The total number of signal MC events are normalised to the number of predicted background events. The area indicated by the arrows is retained after the signal selection cut is applied.

Leading dijet mass, m_{jj}

Heavy neutrinos considered in this analysis have mass $m_N \geq 100$ GeV so the W bosons produced from the heavy neutrino decay are produced on-shell as they have mass $m_W \approx 80$ GeV. In order to select signal events at high efficiency whilst rejecting background it is required that the invariant mass of the two leading p_T jets satisfies $|m_{jj} - m_W| < 20$ GeV. The m_{jj} distribution of the signal and expected background is shown in Figure 8.3, where the arrows indicate the region that is retained after the cut is applied.

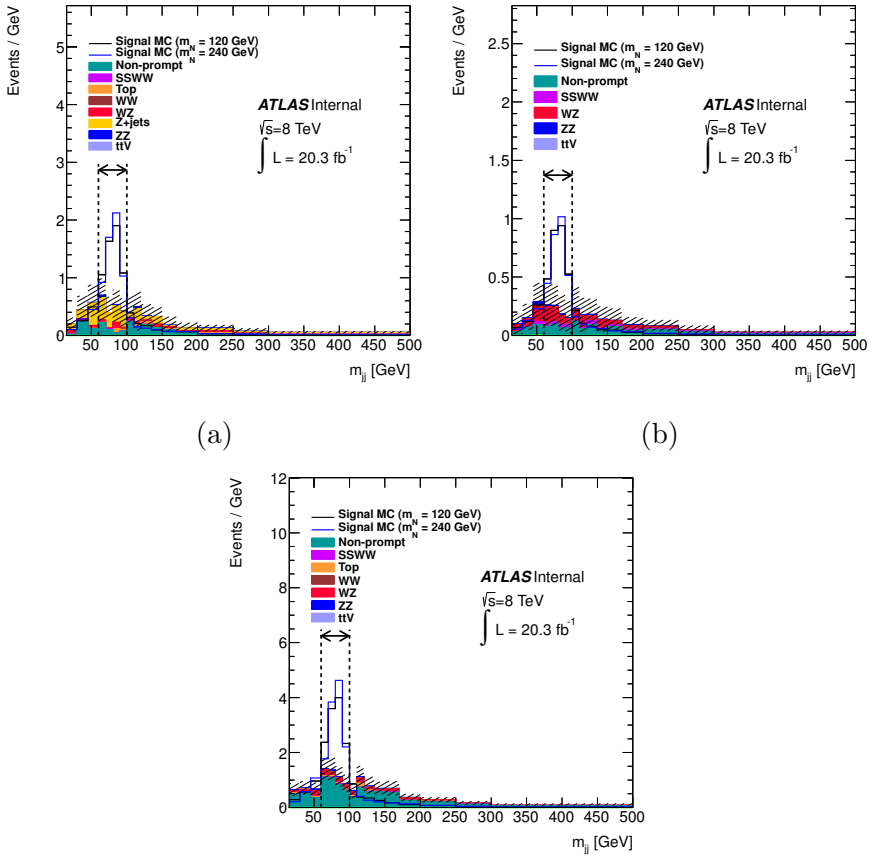

Figure 8.3: The m_{jj} distribution in events with two SS leptons, two jets, $E_T^{\text{miss}} < 40$ GeV and, for the ee channel, $|m_{ee} - m_Z| > 20$ GeV. Figures (a), (b) and (c) show the ee, $\mu\mu$ and $e\mu$ channels respectively. The total number of signal MC events are normalised to the number of predicted background events. The area indicated by the arrows is retained after the signal selection cut is applied.

After optimisation the events selected in the signal region are required to satisfy the following criteria:

- exactly two same-sign *tight* leptons,
- at least two *tight* jets,
- the missing transverse energy in the event $E_T^{\text{miss}} \leq 40$ GeV,
- the leading dijet mass is required to be $|m_{jj} - m_W| < 20$ GeV,
- the leading dilepton mass is required to be $m_{\ell\ell} > 40$ GeV,
- in the electron channel, the invariant mass of the dielectron pair must satisfy $|m_{ll} - m_Z| > 20$ GeV.

The acceptance A, efficiency ϵ and total efficiency $\{A \times \epsilon\}$ of the MC signal samples with respect to these cuts is presented in Figure 8.4. The acceptance A is the fraction of signal events, before detector simulation, to contain exactly two leptons with $p_T \geq 20$ GeV and $|\eta| < 2.5$ and at least two jets with $p_T \geq 20$ GeV and $|\eta| < 2.8$. The efficiency ϵ is the fraction of signal events, after the acceptance cuts, to pass the full signal event selection criteria. One should note that A and $\{A \times \epsilon\}$ are calculated independently and ϵ is therefore extrapolated from these numbers. Both A and ϵ are measured to increase with m_N. For the case of A this is due to the minimum lepton p_T criteria and for ϵ this is primarily due to the isolation efficiency increasing as a function of lepton p_T. The efficiency is also higher for muons than electrons due in part to the tighter isolation criteria for electrons, but also as a result of the requirement on the dielectron mass m_{ee} that is not applied to $\mu\mu$ and $e\mu$ events.

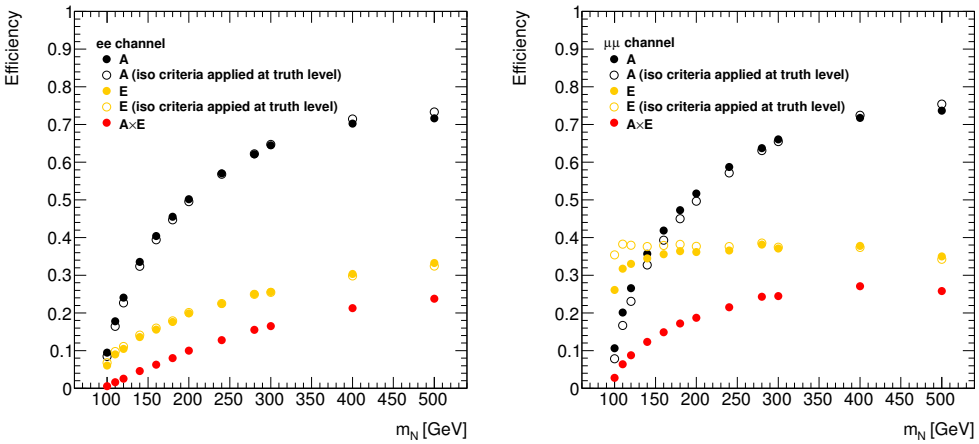

(a)

(b)

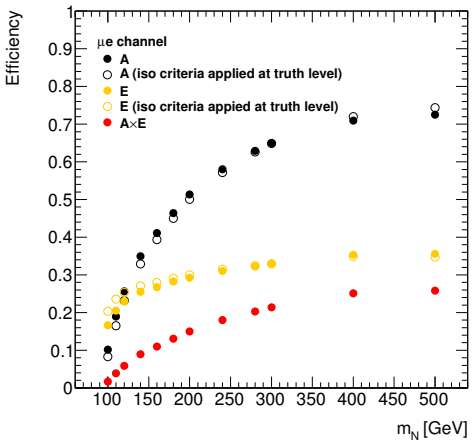

(c)

Figure 8.4: Signal efficiency for the signal samples. In the legends: A denotes the acceptance for events to pass truth-level cuts (defined by exactly two leptons, lepton $p_T > 20$ GeV, $|\eta| < 2.5$, at least one lepton with $p_T > 25$ GeV, $m(\ell\ell) > 40$ GeV, n(jets) > 1, where jets have $p_T > 20$ GeV, $|\eta| < 2.8$); E denotes the efficiency for events to pass analysis-level cuts after the latter acceptance cuts (A) are implemented; and $\{A \times E\}$ is the total efficiency for events to pass both sets of cuts (A **and** E). Note that A and$\{A \times E\}$ are calculated independently and E is extrapolated from these numbers. The clear circles indicate value of A (and corresponding E) if one includes the analysis isolation cut at truth level.

Chapter 9

Background estimation

In order to quantify whether a signal has been observed, one must be able to accurately predict the number of background events due to SM processes in the signal region presented in Section 8.3. Leptons produced in background events in this analysis are categorised either as originating from 'prompt' sources, which refers to those from W or Z decays, or from 'non-prompt' sources, which refers to misreconstructed leptons or leptons produced in hadronic decays.

In general the phenomenological calculations of EW processes are sufficiently accurate so that MC can be used to predict the background due to prompt processes, which will be discussed in Section 9.1. In Section 9.2, a data-driven approach is used to estimate the number of events due to non-prompt lepton production as this background is a convolution of detector effects and hadronic processes. There is also a contribution from Z+jets and $t\bar{t}$ events due to electron 'charge-flips' which leads to pairs of leptons with OS electric charge being accepted in the SS selection. Charge-flips originate from both electron-detector interactions and charge misassignment in the electron reconstruction. A data-driven method, presented in Section 9.3, is used to estimate the charge-flip background due to this complexity.

9.1 Prompt background

Prompt leptons are those originating from EW decays. As well as mechanisms that lead to two SS leptons in the final state, there are also processes that give rise to more than two leptons. The latter processes can contribute to the background in the signal region if one or more of the leptons fail the selection criteria or fall out of the detector's geometric acceptance. An example of such an event is shown in Figure 9.1, where one muon from the decay $WZ \to e\nu\mu\mu$ falls out the detector geometry.

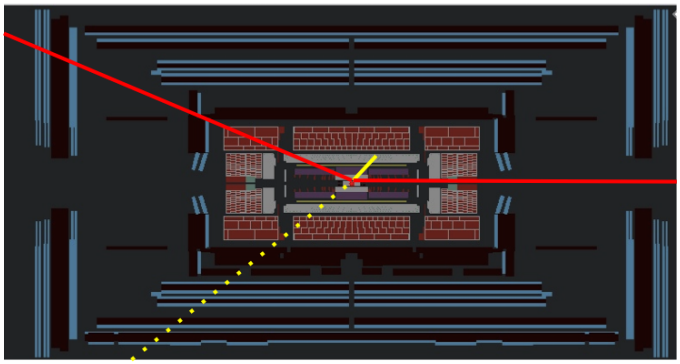

Figure 9.1: Illustration of a $WZ \to e\nu\mu\mu$ decay where the electron is represented by the solid yellow line, the neutrino by the dotted yellow line and the muons by the red lines. One muon has fallen out of the detector acceptance so this event would mimic a two lepton event.

This section presents the production mechanisms and cross-sections for prompt processes that are relevant to this analysis in Section 9.1.1 and the uncertainty associated with the number of predicted events in Section 9.1.2.

9.1.1 Production mechanisms and cross-sections

The dominant prompt background contributions in the signal region are from diboson processes $WZ \to \ell^{\pm}\nu\ell^{\pm}\ell^{\mp}$ and $ZZ \to \ell^{\pm}\ell^{\mp}\ell^{\pm}\ell^{\mp}$. These are collectively denoted 'VV', where V is a W or Z boson. The Leading Order (LO) Feynman diagrams for these processes are presented in Figure 9.2. Another source of VV events is via Higgs production, primarily due to the process $gg \to H \to ZZ$ as shown in Figure 9.3. The contribution from $t\bar{t}$ production associated with a Z boson ('$t\bar{t}Z$') is also considered as shown in Figure 9.4.

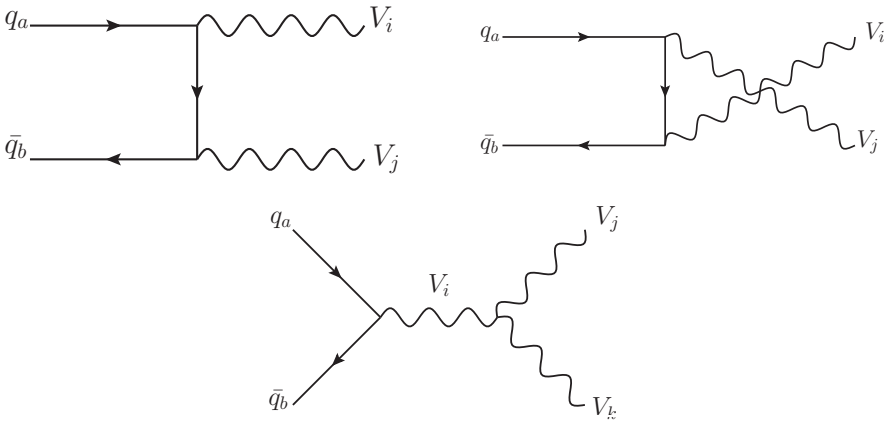

Figure 9.2: Leading order Feynman diagrams describing diboson (ZZ, WW, WZ) production.

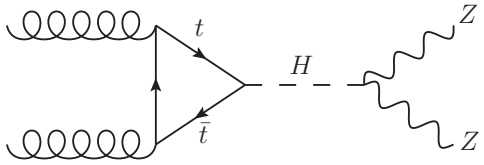

Figure 9.3: Leading order Feynman diagram describing $gg \to H \to ZZ$ production.

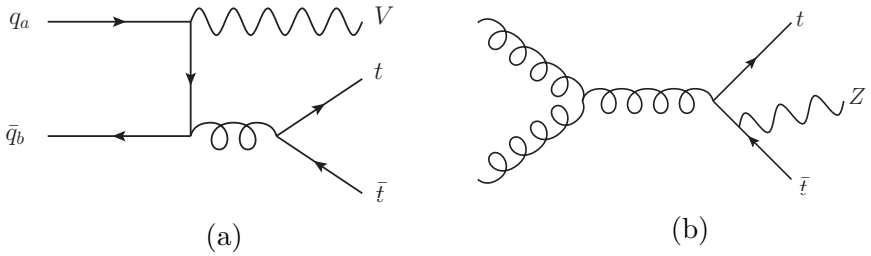

Figure 9.4: Example of leading-order Feynman diagrams (a) describing $t\bar{t}V$ and (b) $t\bar{t}Z$ production.

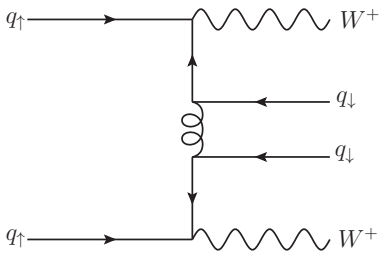

Figure 9.5: Leading order Feynman diagram describing SS WW production in association with two jets. The subscripts '↑' and '↓' refer to up and down-type quarks respectively.

There are also SM interactions which result in exactly two SS leptons. One such source is from $t\bar{t}$ production in association with a W boson, which is referred to as '$t\bar{t}W$'. The processes $t\bar{t}W$ and $t\bar{t}Z$ production are collectively referred to as '$t\bar{t}V$', which are produced according to the LO diagrams in Figure 9.4. Two SS leptons can be produced by this mechanism if the following decays occur:

$$t\bar{t}W \rightarrow \left\{ \begin{array}{lllll} t & \rightarrow & W^+q & \rightarrow & \ell^+\nu q \\ \bar{t} & \rightarrow & W^-q & \rightarrow & qqq \\ W & \rightarrow & \ell^+\nu & & \end{array} \right\} \rightarrow \ell^+\ell^+ \; \nu\nu \; qqqq.$$

Another mechanism for SS dilepton production is the production of two SS W bosons ('SS-WW') by the mechanism in Figure 9.5. The W bosons in this process are then required to decay according to $W^\pm W^\pm \rightarrow \ell^\pm\ell^\pm\nu\nu$.

The cross-sections of the presented prompt background processes are shown in Table 9.1. The highest cross-section times branching ratio is due to WZ production, although the given value does not account for the requirement that leptons fall out of the detector geometry or lepton selection if the process is to be accepted in the signal region.

Process	$\sigma_{\text{tot}} \times$ BR [pb]
$pp \rightarrow WZ \rightarrow \ell\ell \; \ell\nu$	0.34
$pp \rightarrow ZZ \rightarrow \ell\ell \; \ell\ell$	0.035
$pp \rightarrow ttZ \rightarrow \ell\nu \; \ell\ell \; qqqq$	0.021
$pp \rightarrow W^\pm W^\pm \rightarrow \ell^\pm \; \ell^\pm \; qq$	0.018*
$pp \rightarrow ttW \rightarrow \ell\nu \; \ell\nu \; qqqq$	0.0076
$pp \rightarrow H \rightarrow ZZ \rightarrow \ell\ell \; \ell\ell$	0.0027

Table 9.1: The NLO (*LO) cross-section times branching ratio for prompt background processes. The branching ratios do not account for the requirement that leptons fall out of the detector geometry in the case of WZ, ZZ and $t\bar{t}Z$ if they are to accepted in to the signal region [93–96].

9.1.2 Normalisation uncertainty on the prompt background estimation

In addition to the uncertainties presented in Section 7.7 which are applied to all MC, one must also consider the uncertainty on the cross-sections used to generate the MC samples. For ttV, Higgs and SS-WW backgrounds the uncertainty on the cross-section is calculated at NLO. The uncertainties for these processes are taken from the uncertainty on the cross-section, scale uncertainty and PDF choice, and are listed in Table 9.2.

Background	MC generator	Normalisation uncertainty
ttV	`MadGraph+Pythia`	30%
Higgs	`POWHEG+Pythia`	20%
SS-WW	`MadGraph+Pythia`	50%

Table 9.2: The normalisation uncertainty assigned to ttV, Higgs and SS-WW backgrounds [66, 97, 98].

Unlike the background processes in Table 9.2, the VV background features no additional jets produced at LO. The MC generator (`Sherpa`) produces up to three extra jets in addition to the diboson pairs. As it is possible to isolate a high yield of VV events, the normalisation in the VV MC is evaluated as a function of the number of jets in the event by comparing MC to data. In particular one can consider events containing exactly three leptons, which are dominated by WZ decays, and events containing exactly four leptons, which are dominated by ZZ decays. Control regions are therefore defined which contain three or four *tight* leptons. In these regions, the leading lepton in the event is required to satisfy $p_T > 25$ GeV, and all other leptons are required to satisfy $p_T > 20$ GeV. Events with any additional *medium* leptons are rejected.

The kinematics of these events in data are compared to the prediction from simulation. Figure 9.6 shows the number of jets and the invariant mass of the leading two leptons in events containing four electrons or four muons. The invariant mass distributions show a peak at m_Z, as predicted in MC and

observed in data. The overall level of agreement between data and MC is good, although the sample of data is statistically limited, particularly in the electron channel. Figures 9.7(a) and (b) show three-electron events, Figures 9.7(c) and (d) show three-muon events and Figures 9.7 (e) and (f) show any combination of electrons and muons in the events containing three leptons, but excluding any events which are in Figures 9.7 (a-d). There is good agreement in all three channels between data and MC, so it is concluded that the predicted normalisation does not need to be corrected.

All events from the three and four lepton regions are used to assign an uncertainty on the normalisation of all VV processes. The procedure to assign the uncertainty to both WZ and ZZ processes is justified as the underlying modelling of additional jets is fundamentally the same in both the WZ and ZZ MC samples. The uncertainty is assigned from the difference observed between data and MC as a fraction of the total number of events. The uncertainties are presented in Table 9.3 as a function of the number of jets in the event. For events with at least two jets, which is true for the signal region presented in Section 8.3, the uncertainty is 17.5%.

In order to test the validity of the measured normalisation uncertainty in events with two SS leptons, diboson events generated by `Sherpa` MC are compared to those generated with `Powheg+Pythia8` in Figure 9.8. The prescribed uncertainty, which is indicated by the red lines, is considered to be sufficient to cover the observed variations between the generators.

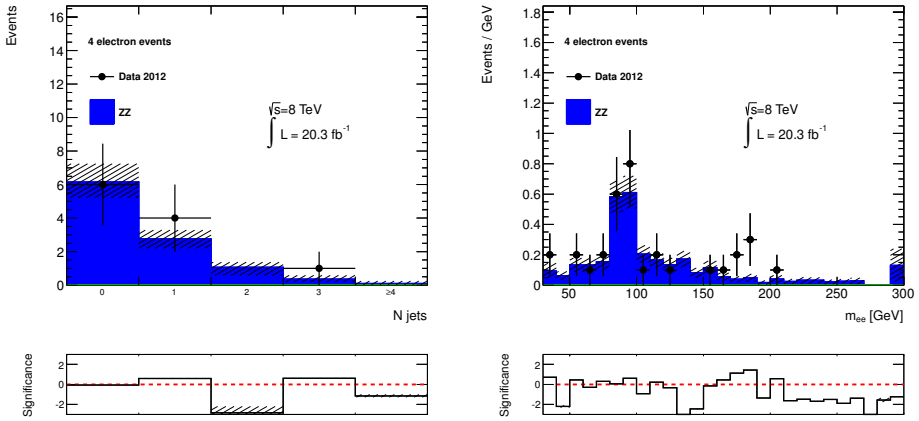

(a) *eeee* (b) *eeee*

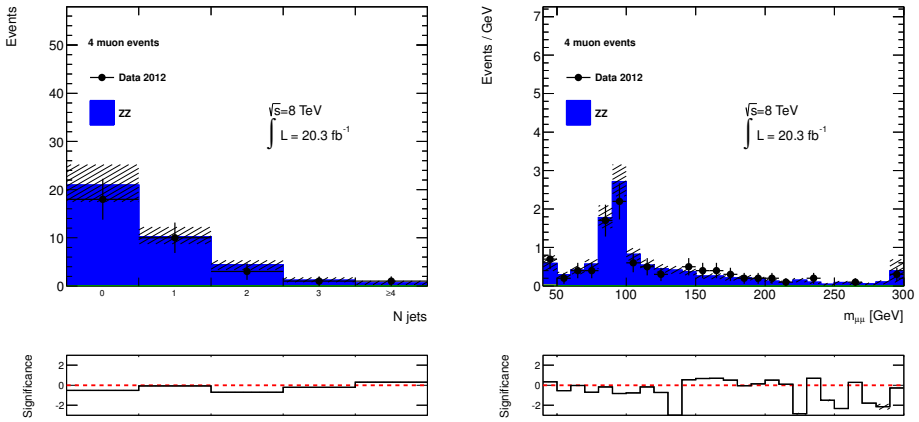

(c) $\mu\mu\mu\mu$ (d) $\mu\mu\mu\mu$

Figure 9.6: Kinematic distributions for events with four leptons. Only the two highest p_T leptons are used in the dilepton mass distributions.

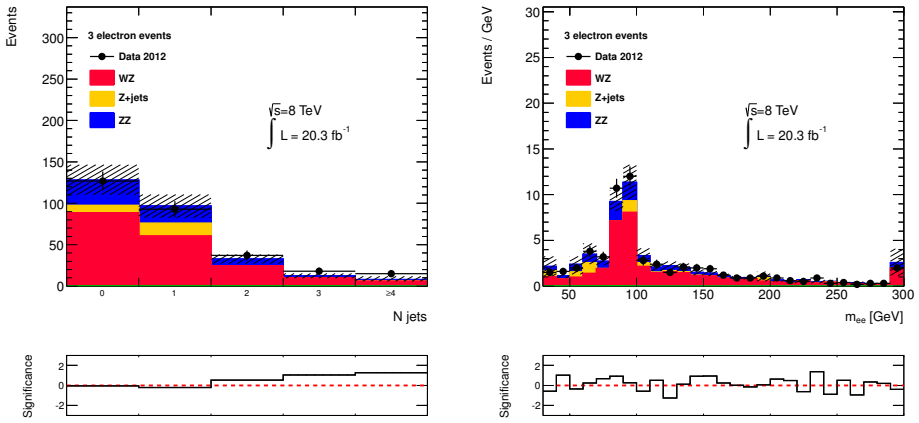

(a) eee

(b) eee

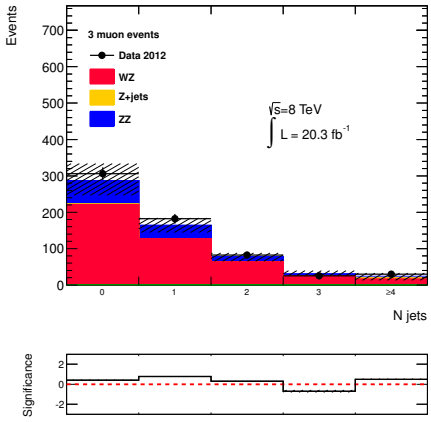

(c) $\mu\mu\mu$

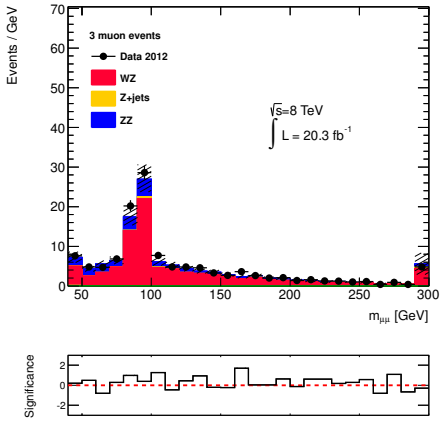

(d) $\mu\mu\mu$

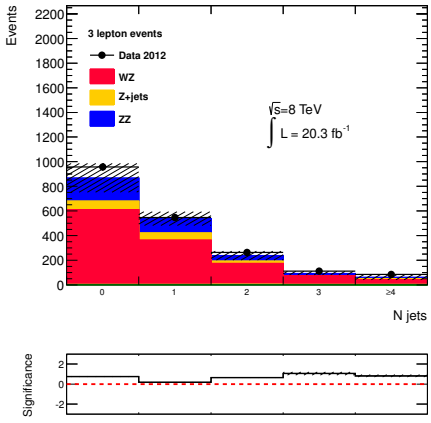

(e) $\ell\ell\ell$

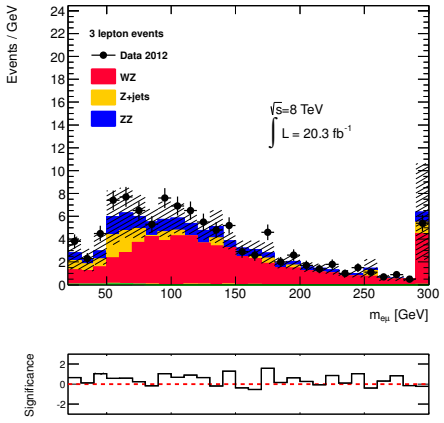

(f) $\ell\ell\ell$

Figure 9.7: Kinematic distributions for events with three leptons. Only the two highest p_T leptons are used in the dilepton mass distributions. The events in the three regions, eee, $\mu\mu\mu$ and $\ell\ell\ell$, are mutually exclusive.

Number of jets	0	1	2	≥ 2	3	≥ 4
Normalisation uncertainty [%]	8.3	4.7	9.49	17.5	18.5	30.2

Table 9.3: Normalisation uncertainty as a function of jet multiplicity for diboson backgrounds.

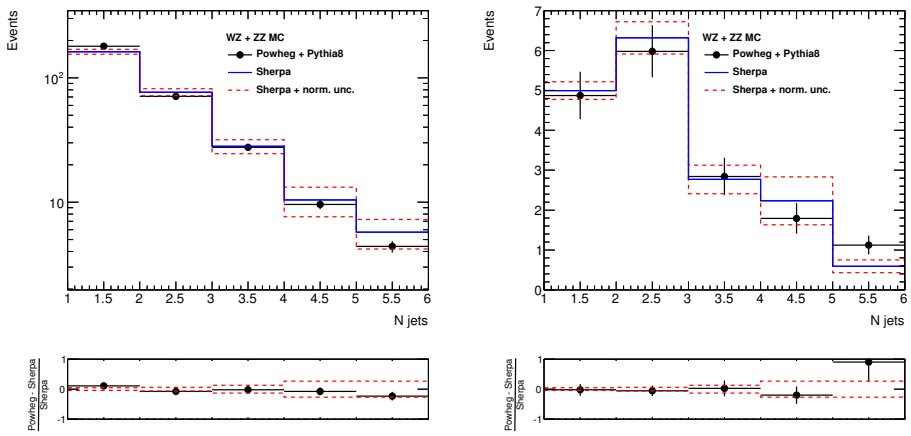

Figure 9.8: The jet multiplicity distribution measured in simulated events generated with `Sherpa` and `Powheg+Pythia8` MC for events containing (a) three muons and (b) two SS muons. The normalisation uncertainties that are indicated by the red lines are the values presented in Table 9.3.

9.2 Non-prompt background

Non-prompt or 'fake' leptons contribute a large irreducible background in the signal region. Non-prompt leptons mainly originate from hadronic decays, such as semi-leptonic heavy meson decays or the decay-in-flight of a $\pi^{\pm}$ or $K^{\pm}$ meson. The non-prompt background for muons also includes 'punch-through' jets that penetrate the muon system. For electrons it includes photons or jets which have been misidentified as an electron, and also electrons that originate from photon conversions. In order to estimate these backgrounds in this analysis the data-driven 'Matrix Method' is used. This method is presented in the following section.

9.2.1 Matrix Method

There are broadly two types of events where non-prompt leptons may contribute to the signal region. The first case is where one non-prompt lepton is produced in an event which also includes a prompt lepton originating from a W or Z boson decay. An example of a SM process included in this category is the process $W \to \ell\nu+$ jets which is illustrated in Figure 9.9, where a non-prompt lepton is produced in the decay of a hadron from a jet. The second case of events to consider is those where both leptons are non-prompt, which includes QCD dijets, $b\bar{b}$ production or hadronically decaying $t\bar{t}$ events.

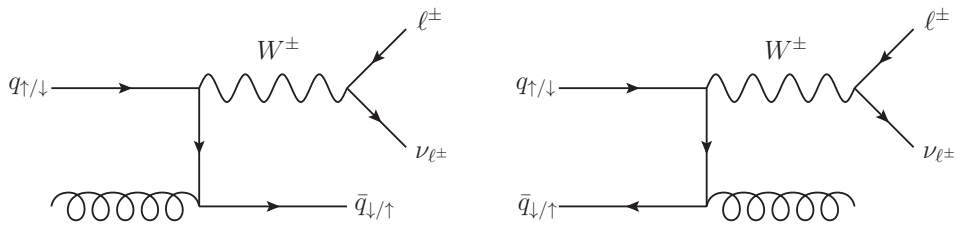

Figure 9.9: Leading order Feynman diagrams for W production in association with one jet. A lepton that is produced in the decay of the hadronised jet is categorised as being 'non-prompt', whereas the lepton produced directly from the W decay is 'prompt'.

Considering these types of processes, the following categories of dilepton events are defined:

- *RR* - events with two prompt ('real') leptons,
- *RF* - events where the highest-p_T lepton is prompt and the second lepton is non-prompt,
- *FR* - events where the highest-p_T lepton is non-prompt and the second lepton is prompt, and
- *FF* - events with two non-prompt leptons.

The total non-prompt background N^{fake} in terms of the number of events, N, from these region is given by:

$$N^{\text{fake}} = N_{RF} + N_{FR} + N_{FF}. \tag{9.1}$$

The key principle of the Matrix Method is that loose-quality leptons can be characterised as being prompt or non-prompt by their efficiency to pass a *tight* cut. The 'loose' lepton criteria are defined for electrons in Section 9.2.2 and for muons in Section 9.2.6. The '*tight*' criteria are defined in Section 7.4.1 for electrons and Section 7.3.1 for muons. Therefore one can rewrite the terms in Equation 9.1 as:

$$\begin{aligned} N_{RF} &= rfN^{ll}_{RF} \\ N_{FR} &= frN^{ll}_{FR} \\ N_{FF} &= ffN^{ll}_{FF} \end{aligned} \tag{9.2}$$

where N^{ll} is the number of events containing two loose leptons, and r and f are the efficiencies for loose prompt leptons and loose non-prompt leptons respectively to pass the *tight* lepton selection criteria. Although the efficiencies r and f can be measured directly, the yields N^{ll}_{RF}, N^{ll}_{FR} and N^{ll}_{FF} cannot. Instead they can be related to the observed number of data events in four categories of events with exactly two leptons:

- *TT* - events with two leptons passing the tight criteria,
- *TL* - events where the highest-p_T lepton passes the tight criteria and the second lepton fails the tight criteria,

- LT - events where the highest-p_T lepton fails tight criteria and the second lepton passes the tight criteria, and
- LL - events with two leptons failing the tight criteria.

The number of events in categories (TT, TL, LT, LL) are related to those in (RR, RF, FR, FF) according to:

$$\begin{bmatrix} N_{TT} \\ N_{TL} \\ N_{LT} \\ N_{LL} \end{bmatrix} = \begin{bmatrix} rr & rf & fr & ff \\ r(1-r) & r(1-f) & f(1-r) & f(1-f) \\ (1-r)r & (1-r)f & (1-f)r & (1-f)f \\ (1-r)(1-r) & (1-r)(1-f) & (1-f)(1-r) & (1-f)(1-f) \end{bmatrix} \begin{bmatrix} N^{ll}_{RR} \\ N^{ll}_{RF} \\ N^{ll}_{FR} \\ N^{ll}_{FF} \end{bmatrix}.$$

Measurements of r and f are generally a function of the kinematics of the lepton so the substitutions $r \to r_i$, $f \to f_i$ are made with i corresponding to whether one is describing the highest-p_T lepton ($i = 1$) or the second lepton ($i = 2$). The yields N^{ll}_{RF}, N^{ll}_{FR} and N^{ll}_{FF} can now be extracted by inverting the matrix:

$$\begin{bmatrix} N^{ll}_{RR} \\ N^{ll}_{RF} \\ N^{ll}_{FR} \\ N^{ll}_{FF} \end{bmatrix} = \alpha \begin{bmatrix} (1-f_1)(1-f_2) & (f_1-1)f_2 & f_1(f_2-1) & f_1 f_2 \\ (f_1-1)(1-r_2) & (1-f_1)r_2 & f_1(1-r_2) & -f_1 r_2 \\ (r_1-1)(1-f_2) & (1-r_1)f_2 & r_1(1-f_2) & -r_1 f_2 \\ (1-r_1)(1-r_2) & (r_1-1)r_2 & r_1(r_2-1) & r_1 r_2 \end{bmatrix} \begin{bmatrix} N_{TT} \\ N_{TL} \\ N_{LT} \\ N_{LL} \end{bmatrix} \tag{9.3}$$

$$\text{where} \quad \alpha = \frac{1}{(r_1 - f_1)(r_2 - f_2)}.$$

If the prompt and non-prompt efficiencies are measured, then the different categories of events can be combined together to give an estimate of the non-prompt background. Weights w_{TT}, w_{TL}, w_{LT} and w_{LL} are assigned to each event according to (using Equations 9.1, 9.2 and 9.3):

$$
\begin{aligned}
\text{for } TT \text{ events:} \quad & w_{TT} = \alpha\,(r_1 f_2(f_1-1)(1-r_2) \\
& \qquad + f_1 r_2(r_1-1)(1-f_2) \\
& \qquad + f_1 f_2(1-r_1)(1-r_2))\,, \\
\text{for } TL \text{ events:} \quad & w_{TL} = \alpha r_1 r_2(1-f_1) f_2, \\
\text{for } LT \text{ events:} \quad & w_{LT} = \alpha r_1 r_2 f_1(1-f_2), \\
\text{for } LL \text{ events:} \quad & w_{LL} = -\alpha r_1 r_2 f_1 f_2,
\end{aligned}
$$

$$
\text{such that for } n \text{ events:} \quad N^{\text{fake}} = \sum_j^n \left(w_{TT}^j + w_{TL}^j + w_{LT}^j + w_{LL}^j\right).
$$

Generally one should note that as $r > f$, w_{TT} is always negative. Consequently TT and LL events have the effect of reducing the non-prompt background estimate, whereas TL and LT events increase the estimate. In the following sections the measurements of r and f, which are the key variables in determining the non-prompt background, will be discussed.

9.2.2 Loose electron definition

A loose electron is defined as an electron which passes both the *medium* requirements and the impact parameter requirements of the *tight* electron selection. Therefore for a loose electron to be tight it must satisfy the **Tight++** and *tight* isolation requirements.

The non-prompt efficiency is found to depend on whether an electron originates from a photon conversion or not. As part of the **Tight++** requirement any 'single-track conversion' electron is rejected, however electrons from 'two-track conversions' are not. A two-track conversion, as illustrated in Figure 9.10, refers to an electron that has radiated a photon that has subsequently converted to an electron-positron pair so that two additional tracks are reconstructed. In a single-track conversion only one of the two additional tracks is reconstructed. In order to retain consistency with the **Tight++** criteria, loose electrons are defined as not being from a single-track conversion.

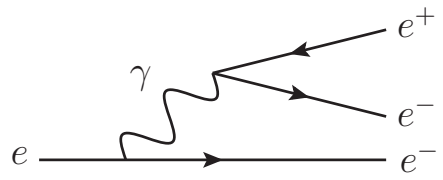

Figure 9.10: Diagram illustrating a two-track conversion, where an electron has radiated a photon that converts to give two additional tracks.

9.2.3 Electron trigger parameterisation

As the primary electron trigger (`EF_e24vhi_medium1`) includes a requirement on hadronic core leakage ('`vhi`') as well as track isolation (both defined in Section 5.3), the prompt and non-prompt efficiencies are parameterised in terms of the following categories of electron objects:

- Electrons matched to the 'isolated' analysis trigger `EF_e24vhi_medium1`.
- Electrons matched to the 'non-isolated' analysis trigger `EF_e60_medium1` but not the isolated trigger `EF_e24vhi_medium1`.
- Electrons not matched to any trigger.

9.2.4 Prompt electron efficiency

The efficiency of prompt electrons is measured in a control region which is dominated by prompt electrons and is orthogonal to the signal region. The control region is defined for events such that:

- The event contains exactly two loose electrons with the leading-p_T electron satisfying $p_T > 25$ GeV and the second electron with $p_T > 20$ GeV.
- The electron pair has OS electric charge.
- The electrons must originate from the same vertex.
- The dielectron mass m_{ee} must satisfy $|m_{ee} - m_Z| < 5$ GeV, where m_Z is the Z boson mass.

These requirements isolate a sample of $Z \to ee$ events in order to perform a Tag-and-Probe measurement (Section 7.7.1), with the efficiency criteria being for loose electrons to pass the tight requirement. Since the control region may not be kinematically representative of the signal region, the real electron efficiencies are parameterised in terms of electron p_T and η. The measured efficiencies for prompt electrons are presented in Figure 9.11. The efficiencies are observed to increase for high electron p_T and η.

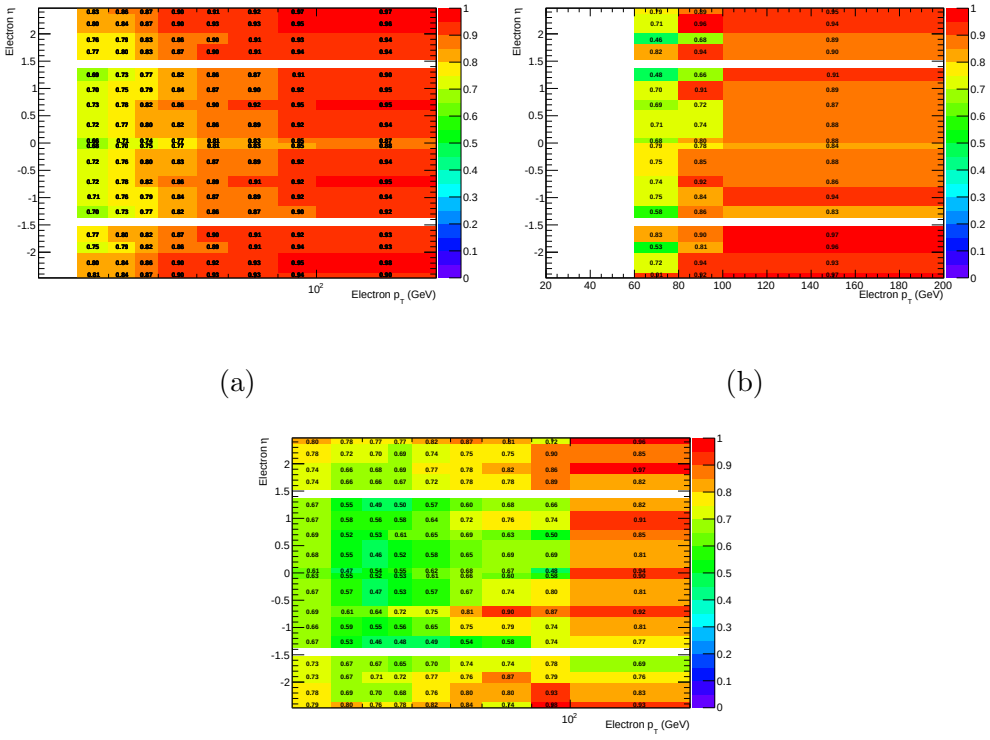

Figure 9.11: Prompt electron efficiencies using electrons in the control region which fire: (a) the primary trigger, (b) only the secondary trigger, (c) neither electron trigger. Note that the secondary trigger requires a 60 GeV offline p_T threshold.

9.2.5 Non-prompt electron efficiency

The non-prompt electron efficiency is measured by defining a region which is dominated by non-prompt electrons. In addition to the loose electron criteria, events are selected with exactly one loose electron and at least one *tight* jet. To suppress W decays it is required that $E_T^{\text{miss}} + m_T < 40$ GeV where m_T is the transverse mass[1], and $|\Delta\phi\left(e, E_T^{\text{miss}}\right)| < 0.5$. To suppress Z decays it is required that the dielectron mass m_{ee} of any pairs of *very-loose* electrons satisfies $|m_{ee} - m_Z| > 30$ GeV. In order to prevent low mass QCD resonances contaminating the control region with isolated non-prompt leptons it is required that the dielectron mass of any pair of *very loose* electrons is greater than 15 GeV. Additionally, it is required that there are no *loose* muons in the event. This control region isolates events which are dominated by QCD multi-jet events. Any contamination due to W, Z, and $t\bar{t}$ in the events is subtracted using MC estimates.

The non-prompt electron efficiency is parameterised in bins of p_T and η, however this is done separately for the three different trigger conditions and for two-track conversion electrons. The measured non-prompt electron efficiencies are shown in Figure 9.12.

9.2.6 Loose muon definition

There are separate loose muon definitions used to estimate the non-prompt background in $\mu\mu$ and $e\mu$ events respectively, which is driven by the different muon trigger conditions in the two channels (`EF_mu18_tight_mu8_EFFS` or `EF_mu36_tight` in $\mu\mu$ events and `EF_mu24i_tight` or `EF_mu36_tight` in $e\mu$ events). Loose muons with $p_T < 80$ GeV and $\Delta R(\mu, j) < 0.4$ are removed in order to correctly account for the isolation dependence on $\Delta R(\mu, j)$ that is described in Section 7.3.2.

For the non-prompt estimate in $\mu\mu$ events, a loose muon is defined as a *tight* muon without the requirement on the *tight* isolation, which is detailed in Section 7.3.1. Therefore a muon is tight if it passes all the *tight* criteria and

[1] $m_T = \sqrt{2p_T E_T^{\text{miss}}(1 - \cos\left(\Delta\phi\left(e, E_T^{\text{miss}}\right)\right))}$, where p_T refers to the electron.

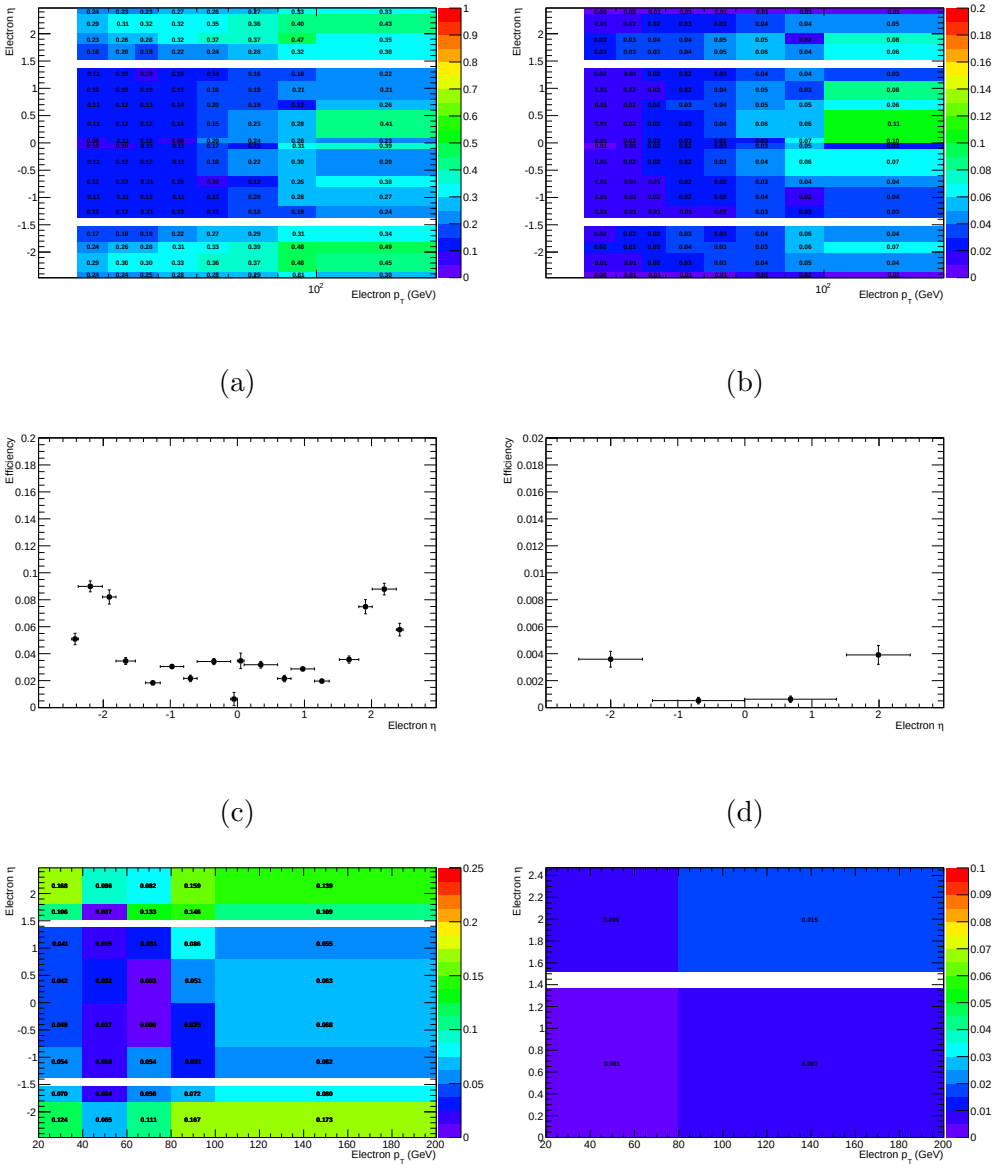

Figure 9.12: Measured non-prompt efficiency for electrons which fire: (a-b) the primary trigger (c-d) only the secondary trigger, (e-f) neither electron trigger. Figures (a,c,e) are for non-conversion electrons while two track conversion electrons are in (b,d,f). Figure (c-d) are parameterised in η only as this region contains a limited number of events in data.

loose if it has passed the same requirement without the isolation

As the muon trigger in $e\mu$ events contains an isolation requirement for $p_T < 36$ GeV (corresponding to 'i' in `EF_mu24i_tight`, see Section 5.3) it is necessary to apply the trigger isolation requirement of PtCone20/$p_T > 0.12$ to all loose muons with $p_T < 36$ GeV.

9.2.7 Prompt muon efficiency

The Tag-and-Probe Method, presented in Section 7.7.1, is used to measure the prompt muon efficiency. Events are selected that contain exactly two loose OS muons which have an invariant mass within 5 GeV of the Z boson mass to isolate $Z \to \mu\mu$ events. The prompt efficiencies are parameterised in terms of muon p_T, η and the number of jets in the event. The efficiencies are also calculated separately for muons with $\Delta R(\mu, \text{jet}) > 0.4$ and $\Delta R(\mu, \text{jet}) < 0.4$ in order to reflect the *tight* isolation criteria.

The prompt muon efficiencies that are used for estimating the non-prompt muon rate in $\mu\mu$ and $e\mu$ events are presented in Figure 9.13 and Figure 9.14 respectively. As a consequence of the trigger requirement in $\mu\mu$ events, the efficiency in the $\mu\mu$ channel can be measured for muon $p_T > 10$ GeV if the event has passed `EF_mu18_tight_mu8_EFFS`.

The prompt efficiencies calculated for the $e\mu$ channel are comparable to those rates calculated for the $\mu\mu$ channel. The prompt efficiencies generally decrease for low η and low p_T, and the efficiencies are lower when there are additional jets in the event. The efficiencies for muons with $\Delta R(\mu, \text{jet}) < 0.4$ are lower as a function of muon p_T than the efficiencies for muons with $\Delta R(\mu, \text{jet}) > 0.4$, when compared to efficiencies at the same value of p_T.

9.2.8 Non-prompt muon efficiency

The efficiency for non-prompt muons to pass the *tight* requirement is measured in a control region which is dominated by muons from non-prompt sources. Events in the control region must satisfy the following criteria:

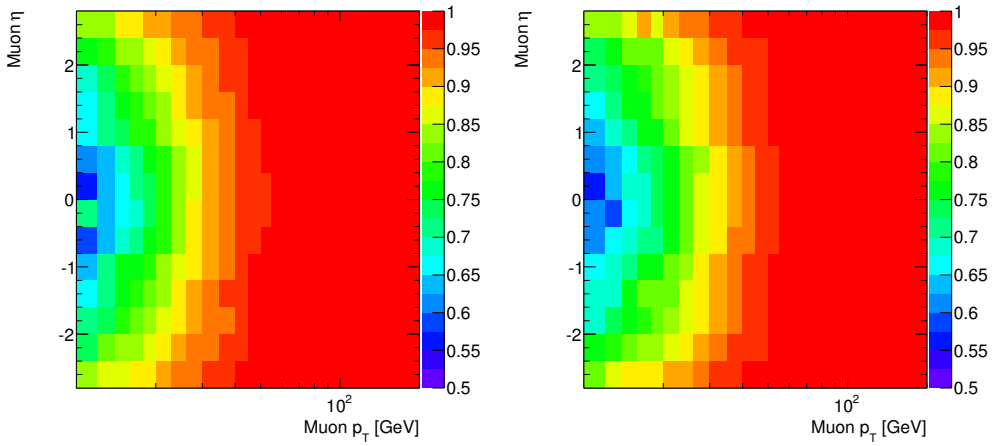

(a)

(b)

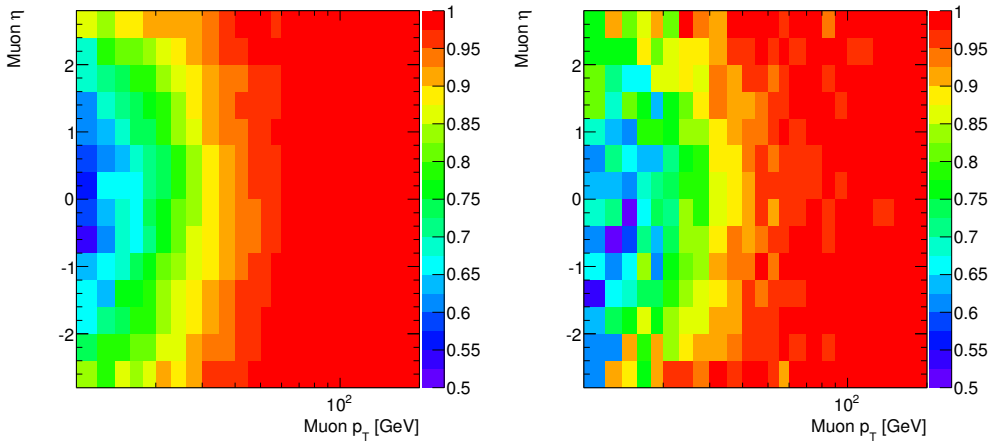

(c)

(d)

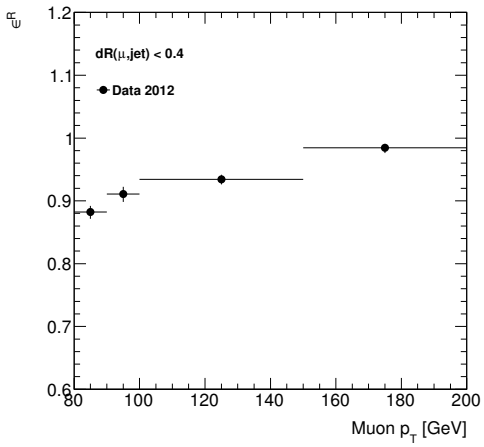

(e)

Figure 9.13: Efficiency for prompt muons in the $\boldsymbol{\mu\mu}$ **channel** measured in events with $dR(\mu, j) > 0.4$ and: (a) 0 jet events, (b) 1 jet, (c) 2-3 jets and (d) ≥ 4 jets. For $dR(\mu, j) < 0.4$ the efficiencies are presented in (e).

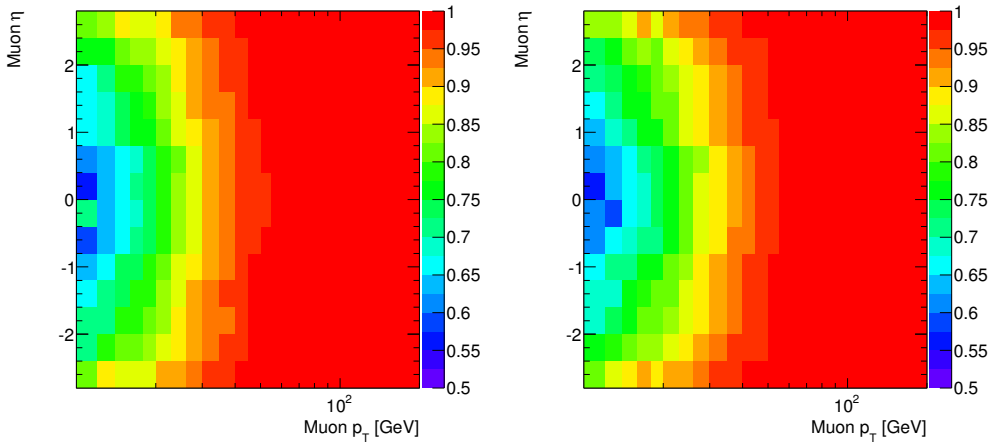

(a)

(b)

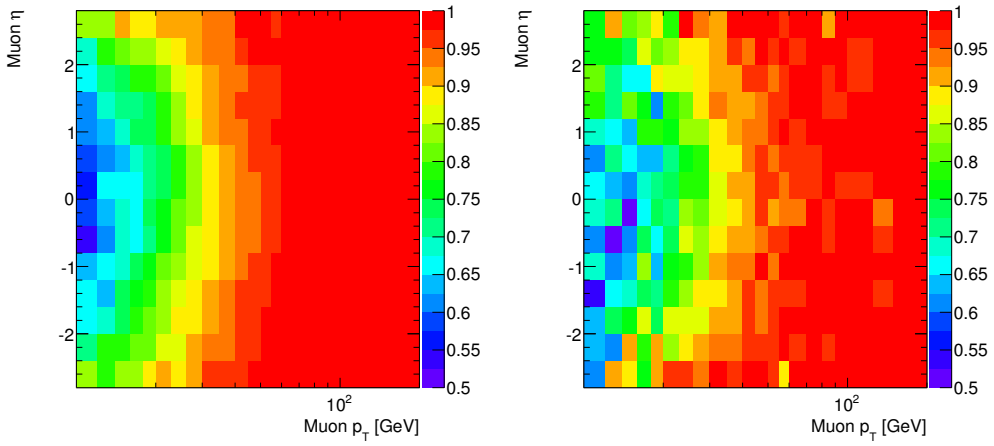

(c)

(d)

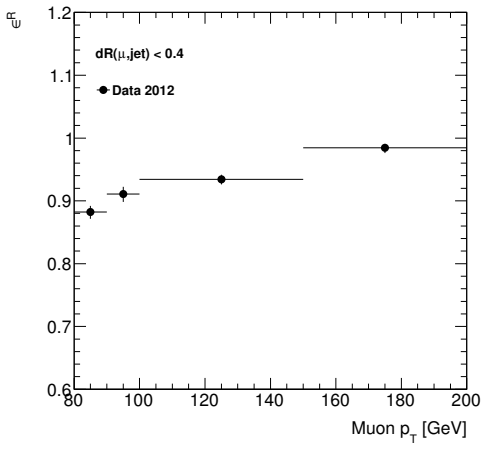

(e)

Figure 9.14: Efficiency for prompt muons in the ***eμ* channel** measured in events with $dR(\mu, j) > 0.4$ and: (a) 0 jet events, (b) 1 jet, (c) 2-3 jets and (d) ≥ 4 jets. For $dR(\mu, j) < 0.4$ the efficiencies are presented in (e).

- **$\mu\mu$ channel:** The `EF_mu18_tight_mu8_EFFS` or `EF_mu36_tight` muon trigger is fired.
- **$e\mu$ channel:** The `EF_mu24i_tight` or `EF_mu36_tight` muon trigger is fired.
- The event has exactly two loose muons.
- In order to reject low mass resonances, $m_{\mu\mu} > 15$ GeV.
- For OS muon pairs: $|m_{\mu\mu}$ - $m_Z| > 30$ GeV.

In order for the control region to contain a high fraction of non-prompt muons, the *tight* impact parameter cut is changed such that:

- $|d_0/\sigma(d_0)| > 5$, as opposed to $|d_0/\sigma(d_0)| < 3$,
- $|d_0| < 10$ mm, as opposed to $|d_0| < 0.2\,\text{mm}$.

Although this region is dominated by non-prompt muons, there is a small contribution from Z+jets, $t\bar{t}$ and VV processes which is subtracted using MC estimates.

Scale factors are applied to account for any difference in the non-prompt muon efficiency measured in this section and muons satisfying the *tight* impact parameter requirements. The correction factors are derived using $b\bar{b}$ MC as the ratio of the non-prompt muon efficiencies measured using muons with $|d_0/\sigma(d_0)| < 3$ and $|d_0| < 0.2\,\text{mm}$ to those measured with $|d_0/\sigma(d_0)| > 5$ and $|d_0| < 10$ mm. The scale factors are shown as function of muon p_T in Figure 9.15, and are validated against $t\bar{t}$ MC in order to confirm that there is no bias due to the phenomenology of $b\bar{b}$ events. A constant correction factor of 1.1 is applied to the non-prompt efficiencies for muon $p_T > 35$ GeV and 1.5 for muon $p_T < 35$ GeV.

It is observed that the probability for loose non-prompt muons to pass the *tight* isolation cut is different for muons from the decays of heavy-flavour mesons, which are mesons containing a b-quark, than from other light-flavour mesons. The non-prompt efficiencies are therefore calculated separately for

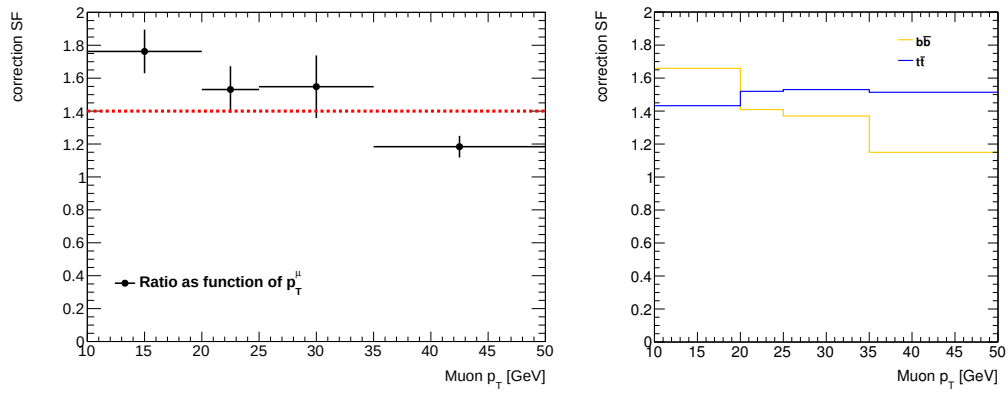

(a) (b)

Figure 9.15: Ratio of the non-prompt muon efficiencies measured using muons with low impact parameter significance compared to muons with high impact parameter significance as a function of muon p_T. Figure (a) shows the correction factor using $b\bar{b}$ MC and (b) shows a comparison of the ratio for $b\bar{b}$ and $t\bar{t}$ MC.

muons in events where a jet is tagged as being heavy-flavour from those without tagged jets. A 'heavy-flavour event' is defined as containing a jet that has been identified as being likely to have originated from the decay of a b-quark. The MV1 'b-tagging' algorithm [99] is used to assign a weight to jets according to their consistency with having originated from a B-meson decay. In order for an event to be tagged as heavy-flavour, a muon must be in an event with at least one jet with tag weight > 0.8119, which corresponds to a b-tagging efficiency of $\sim 70\%$ and purity of $\sim 92\%$. For an event to be tagged as 'light-flavour', the event has to fail the heavy-flavour requirement.

The non-prompt muon efficiencies measured for the $\mu\mu$ channel are presented in Figure 9.16 as a function of muon p_T. The non-prompt muon efficiencies measured for the $e\mu$ channel are presented in Figures 9.17 and 9.18 for the cases $\Delta R(\mu, \text{jet}) < 0.4$ and $\Delta R(\mu, \text{jet}) > 0.4$ respectively. The efficiencies are also separated into regions in η that correspond to the barrel and the end-cap if there are sufficiently high statistics in the sample.

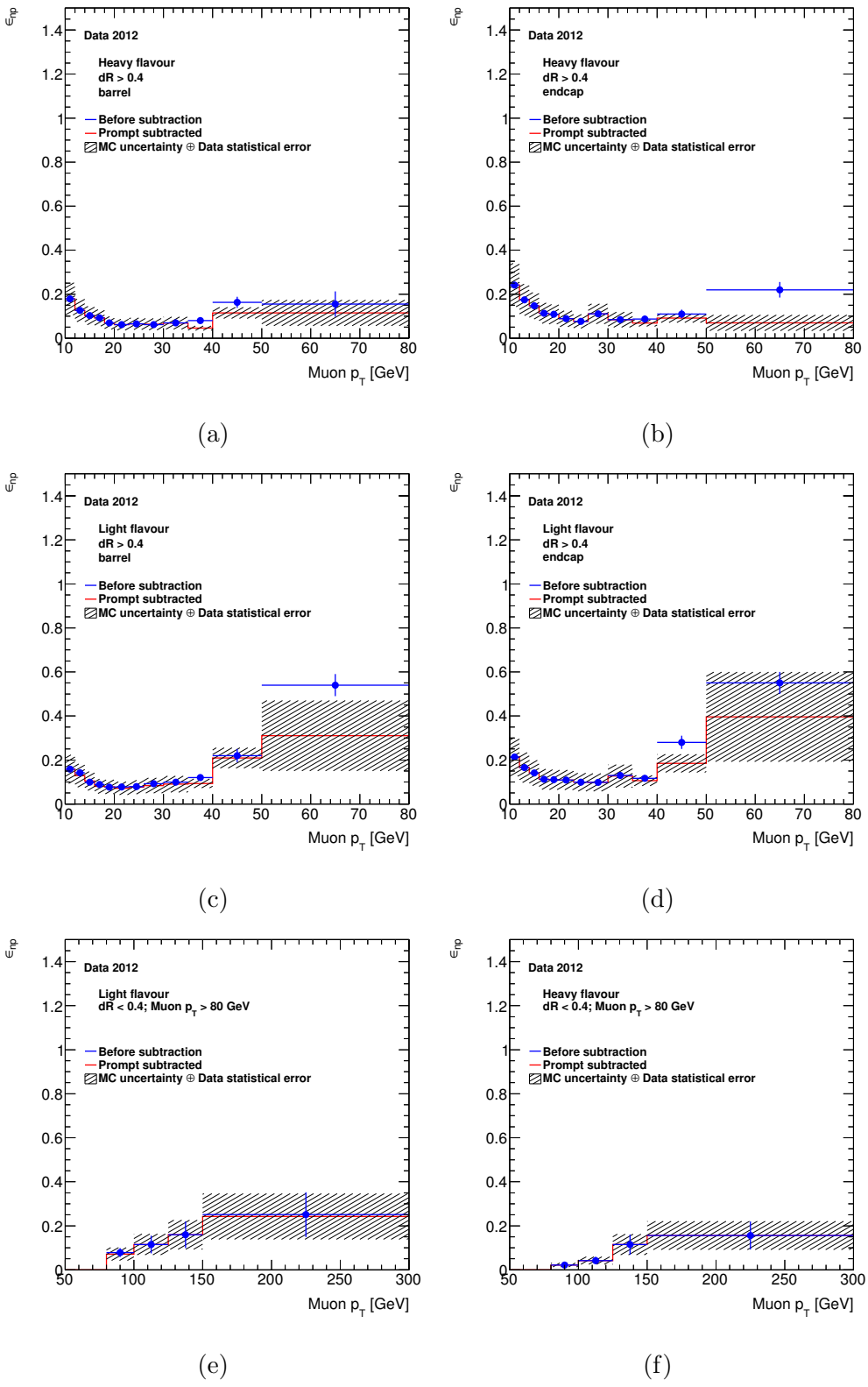

Figure 9.16: Non-prompt efficiencies for muons in the ***μμ* channel** in events passing the `EF_mu18_tight_mu8_EFFS` or `EF_mu36_tight` trigger requirement. Figures (a-d) correspond to $dR < 0.4$ and (e-f) to $dR > 0.4$.

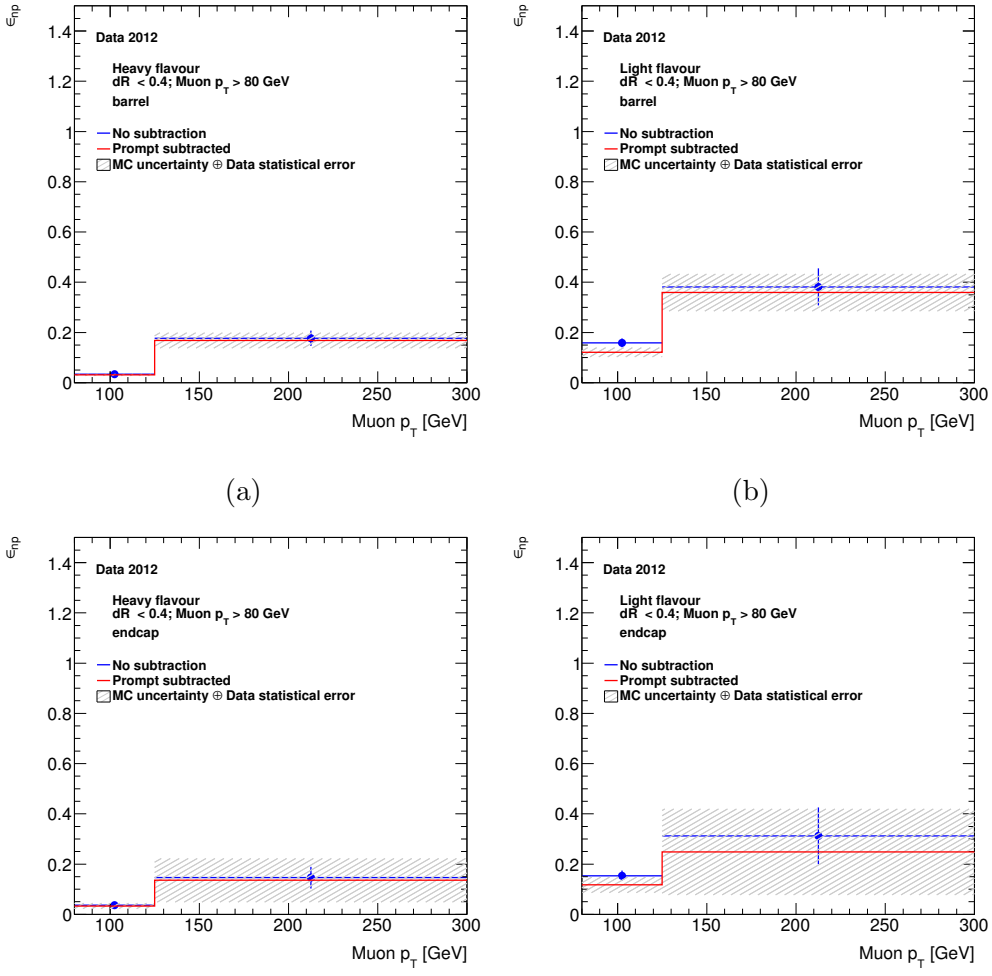

Figure 9.17: Non-prompt efficiencies for muons in the $e\mu$ **channel** in events passing the `EF_mu24i_tight` or `EF_mu36_tight` trigger requirement in the region $dR < 0.4$.

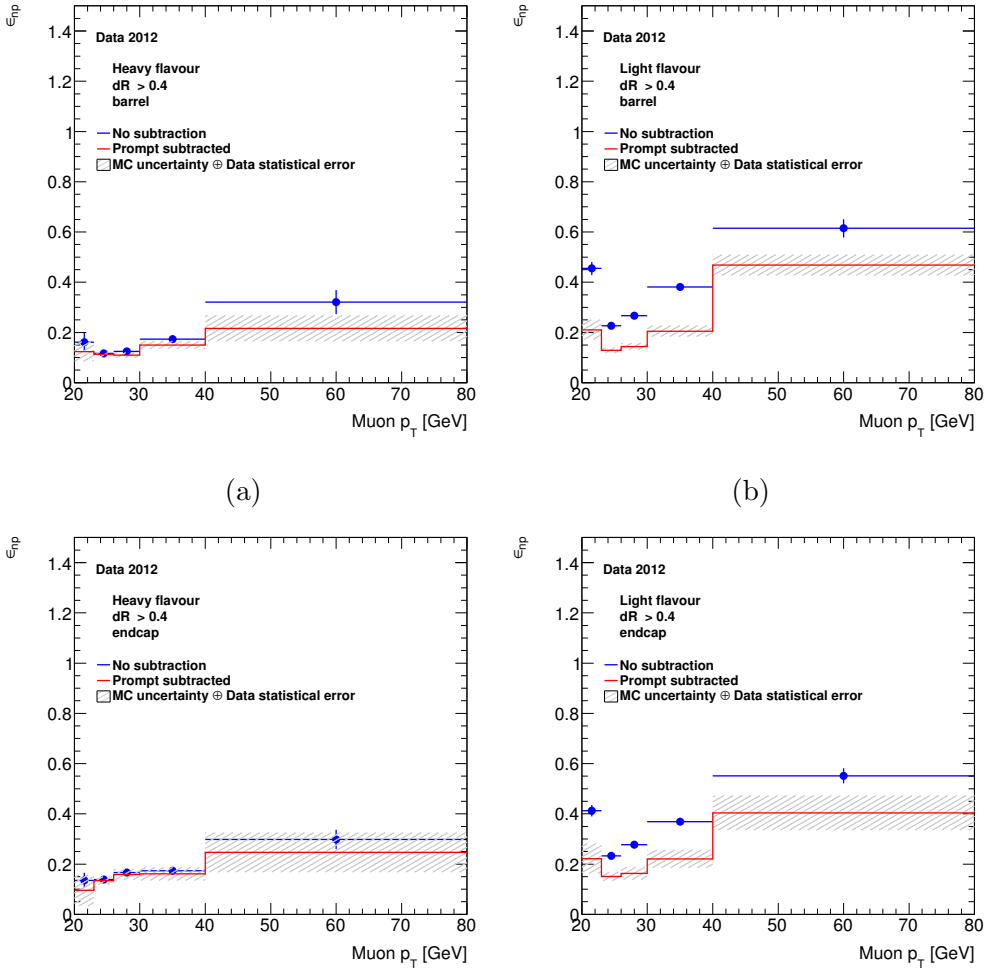

Figure 9.18: Non-prompt efficiencies for muons in the $e\mu$ **channel** in events passing the `EF_mu24i_tight` or `EF_mu36_tight` trigger requirement in the region $dR > 0.4$.

9.2.9 Systematic uncertainty

The uncertainty on the prompt and non-prompt lepton efficiencies is estimated by considering the contributions described in this section.

Prompt lepton efficiency

A systematic uncertainty is assigned to account for any dependence of the prompt efficiencies on lepton η and jet-multiplicity. For electrons, muons in $\mu\mu$ events and muons in $e\mu$ events the uncertainty on the efficiencies corresponds to approximately 3%, 3% and 2% respectively.

Non-prompt efficiency

There are several effects that are taken into account when considering the uncertainty on the non-prompt efficiency:

- The statistical uncertainty on the data, due to limited number of data events. This is typically $\lesssim$ 20% for $p_T > 40$ GeV and $\lesssim$ 40% for $p_T > 100$ GeV.
- Uncertainty on the contamination of prompt muons in the non-prompt control sample. This is estimated using the normalisation uncertainty in MC which has an effect on the measured rate of $\lesssim$ 5%.
- **For muons:** the uncertainty associated with the correction factor between non-prompt efficiencies of muons with low and high impact parameter significance. An uncertainty of 40% is used to cover the scale factor that is applied, as presented in Figure 9.15. This is considered to be an uncertainty associated with the choice of control region in which the non-prompt efficiencies are measured.
- **For electrons:** an uncertainty is considered that is associated with the choice of the control sample. This is evaluated by calculating the total non-prompt background with the presented non-prompt efficiencies, and comparing to the background yield as calculated with efficiencies measured using electrons in a different control region. This region contains a SS electron pair with the signal region removed, a cut on the invariant mass to suppress Z+jets events and a cut on the E_T^{miss}

to suppress W+jets events. The non-prompt efficiencies measured in this region are presented in Figure 9.19. The difference between the total number of backgrounds predicted using both sets of non-prompt efficiencies is assigned as a systematic uncertainty. The systematic uncertainty due to this variation is approximately 25%.

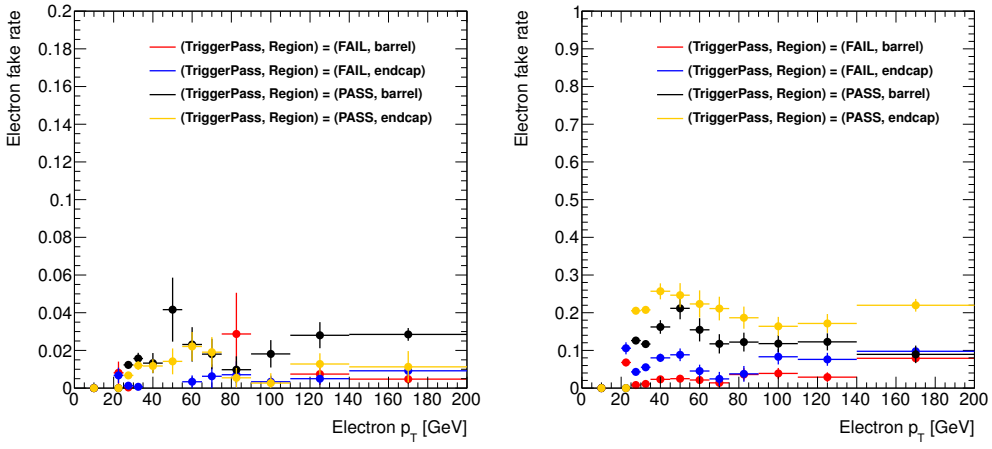

(a) (b)

Figure 9.19: Non-prompt electron efficiencies calculated using electrons in an alternative loose sample to those in the main analysis. Figure (a) shows the non-prompt efficiencies for conversion electrons and (b) for non-conversion electrons.

9.3 Charge-flip background

A lepton 'charge-flip' refers to the mismeasurement of a lepton's true charge, which for this analysis means that genuine OS lepton pairs can contribute to the SS background. Sections 9.3.1 and 9.3.2 will discuss the measurements of the charge-flip rate of electrons and muons respectively. The charge of a lepton is assigned from the curvature of its associated ID track, as well as the MS track in the case of muons. The curvature of a track C is related to the track momentum p orthogonal to the magnetic field B by:

$$C = \frac{qB}{p}$$

where q is the charge of the track. The sign of q is given by the direction of curvature of C. At high momentum the curvature is small so the correct assignment of a track's charge is limited by the resolution of the detector. Furthermore the charge of a lepton can be misassigned by reconstructing a lepton from the conversion of a bremsstrahlung photon.

9.3.1 Electron charge-flips

The electron charge-flip rate, ϵ, is dominated by electrons that emit a hard bremsstrahlung photon which subsequently converts into an electron-positron pair. This can lead to a charge-flip if one of the conversion electrons is mistaken for the hard-scatter electron in the track reconstruction. The energy loss of a charged particle in material, and therefore the probability for the emission of bremsstrahlung photons, is correlated with the length of material traversed. As the material depth of the ATLAS detector is primarily dependent on polar angle from the beam axis, the electron charge-flip rate ϵ is parameterised in η. An initial study with MC events has been used to justify the choice of parameterisation in η rather than p_T. The measurement of $\epsilon(\eta)$ is discussed in this section.

A statistical method is used which considers events with exactly two electrons from Z decays. The method assumes a Poisson distribution P of the number of SS electron pairs N_{SS} in an inclusive set of OS and SS pairs N:

$$P(N_{SS}) = \frac{\left(N\epsilon^{SS}\right)^{N_{SS}} e^{-N\epsilon^{SS}}}{N_{SS}!} \qquad \text{for} \quad N_{SS} \ll N \tag{9.4}$$

where ϵ^{SS} is the probability to select a pair of SS electrons from the inclusive set, which is equated to the charge-flip rate. In order to account for any contamination in data from events considered in the non-prompt estimate, N and N_{SS} are calculated in data as:

$$N = N_{\text{data}} - N_{\text{non-prompt}}$$
$$N^{SS} = N^{SS}_{\text{data}} - N^{SS}_{\text{non-prompt}}$$

where N_{data} and $N_{\text{non-prompt}}$ are the number of events with OS and SS electron pairs measured in data and estimated in the non-prompt background respectively. Correspondingly, N^{SS}_{data} and $N^{SS}_{\text{non-prompt}}$ are the number of events containing only SS electron pairs in data and estimated in the non-prompt background respectively. The non-prompt background is estimated using the method described in Section 9.2.

Regions of the detector where the charge-flip rate is approximately constant, measured with $Z \to ee$ MC, are used to define the following six discrete ranges of η in which ϵ will be measured:

$$|\eta| = \{0.0 \to 0.8 \to 1.45 \to 1.7 \to 2.2 \to 2.3 \to 2.5\}\,. \tag{9.5}$$

The two electrons in a selected $Z \to ee$ event have charge-flip rates which are respectively labelled ϵ_k and ϵ_l, such that $|\eta|$ region k contains one electron and $|\eta|$ region l contains the other electron. The regions k and l refer to any of the six exclusive ranges indicated in Equation 9.5. In order to include the η dependency of the charge-flip rate for events containing two electrons the following substitutions are made:

$$\begin{aligned} N &\to N^{kl} \\ N_{SS} &\to N^{kl}_{SS} \\ \epsilon^{SS} &\to \epsilon_k + \epsilon_l \end{aligned}$$

where N^{kl} is the number of events with electrons in respective η regions k and l, and N^{kl}_{SS} is the subset of N^{kl} that are SS events. Hence Equation 9.4 can be rewritten as:

$$P(N_{SS}) = \prod_{k,l} \frac{\left(N^{kl}(\epsilon_k + \epsilon_l)\right)^{N^{kl}_{SS}} e^{-N^{kl}(\epsilon_k+\epsilon_l)}}{N^{kl}_{SS}!}. \tag{9.6}$$

The numbers N^{kl}_{SS} and N^{kl} can be measured directly however $\epsilon(\eta)$ cannot be directly inferred from these distribution. In order to extract $\epsilon(\eta)$ the likelihood function L is defined as:

$$L = -\ln(P)$$

which is explicitly written as:

$$L = \sum_{k,l} -N^{kl}_{SS} \ln(N^{kl}(\epsilon^k + \epsilon^l)) + N^{kl}(\epsilon^k + \epsilon^l) + \ln(N^{kl}_{SS}!). \tag{9.7}$$

The values of $\epsilon(\eta)$ are therefore extracted by minimising the likelihood L. The following section will discuss the limitations and systematic bias introduced by this method.

Systematic bias

A limitation of the presented method is apparent if one considers that the single-electron charge flip-rate $\epsilon(\eta)$ is derived from events containing two electrons, where only one electron has a charge-flip. Furthermore this method ignores the electron p_T dependence of the charge-flip probability which, as shown using $Z \to ee$ MC in Figure 9.20, is also correlated with the electron η distribution. These effects could potentially introduce a bias in the measured electron charge-flip rate $\epsilon^{\text{meas}}(\eta)$ compared to the true charge-flip rate $\epsilon^{\text{true}}(\eta)$.

The measured electron charge-flip rate $\epsilon^{\text{meas}}(\eta)$ is calculated with the likelihood function L which takes pairs of electrons with a true two-dimensional charge-flip probability distribution $R(k,l)$, where k and l refer to regions of the detector defined in Equation 9.5:

$$R(k,l) = \epsilon^{\text{true}}_k + \epsilon^{\text{true}}_l \qquad \text{where } \epsilon^{\text{true}} \ll 1.$$

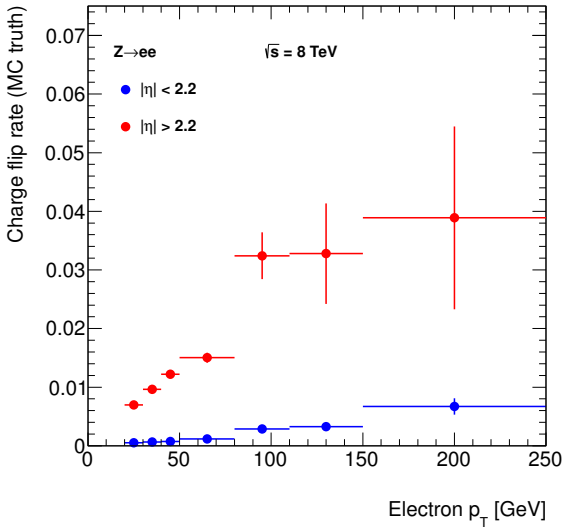

Figure 9.20: The charge-flip distribution as a function of p_T for individual electrons as determined using MC truth information. The distribution is split at electron η = 2.2, as for $\eta > 2.2$ the highest discrepancy is observed between the charge-flip rate measured using the Likelihood Method and using MC truth information.

One can consider $\epsilon^{\text{meas}}(\eta)$ as a transformation of the true charge-flip distribution $\epsilon^{\text{true}}(\eta)$ by a bias function $b(\eta)$:

$$\epsilon^{\text{meas}}(\eta) \;=\; b(\eta)\epsilon^{\text{true}}(\eta). \tag{9.8}$$

If the bias $b(\eta)$ were approximately equal for different $R(k,l)$, i.e. in data and MC, then a simple solution to explicitly remove the bias would be to use a scale factor $S(\eta)$ calculated as the ratio of $\epsilon^{\text{meas}}(\eta)$ measured in data and in MC:

$$S(\eta) = \frac{\epsilon^{\text{meas}}_{\text{Data}}(\eta)}{\epsilon^{\text{meas}}_{\text{MC}}(\eta)} = \frac{b^{\text{Data}}(\eta)\epsilon^{\text{true}}_{\text{Data}}(\eta)}{b^{\text{MC}}(\eta)\epsilon^{\text{true}}_{\text{MC}}(\eta)}.$$

Hence if the bias is equal in data and MC then applying $S(\eta)$ to events in MC which are identified as having a true charge-flip should reproduce the true charge-flip rate of data electrons. The bias can be measured directly in MC by comparing ϵ^{meas} to ϵ^{true}. In order to confirm whether the bias is approximately equal for different true charge-flip rates, 'toy' scale-factors $\chi(\eta)$ are applied to the true charge-flip rate in MC which modifies the two-

dimensional charge flip distribution as:

$$\chi(\eta)R(k,l) = \chi(\eta_k)\epsilon_k^{\text{true}} + \chi(\eta_l)\epsilon_l^{\text{true}}. \tag{9.9}$$

Consider the new bias $b'(\eta)$ that is generated by the modified charge-flip distribution $\chi(\eta)R(k,l)$ by using Equations 9.8 and 9.9:

$$\epsilon'(\eta) \quad = \quad b'(\eta)\chi(\eta)\epsilon^{\text{true}}(\eta).$$

Hence in general one can compare $\chi(\eta)\epsilon^{\text{meas}}$ to $\epsilon'(\eta)$ and simply confirm whether the bias is equal. Six arbitrary forms of $\chi(\eta)$ are shown in Figure 9.21. A comparison between $\chi(\eta)\epsilon^{\text{meas}}$ and $\epsilon'(\eta)$ in Figure 9.22 shows that the bias is, to a good approximation, unaffected by the choice of $\chi(\eta)$.

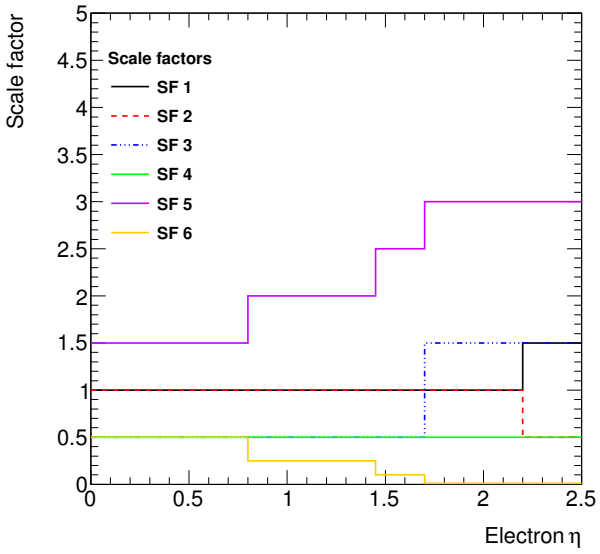

Figure 9.21: Scale factors $\chi(\eta)$ which are applied in Figure 9.22

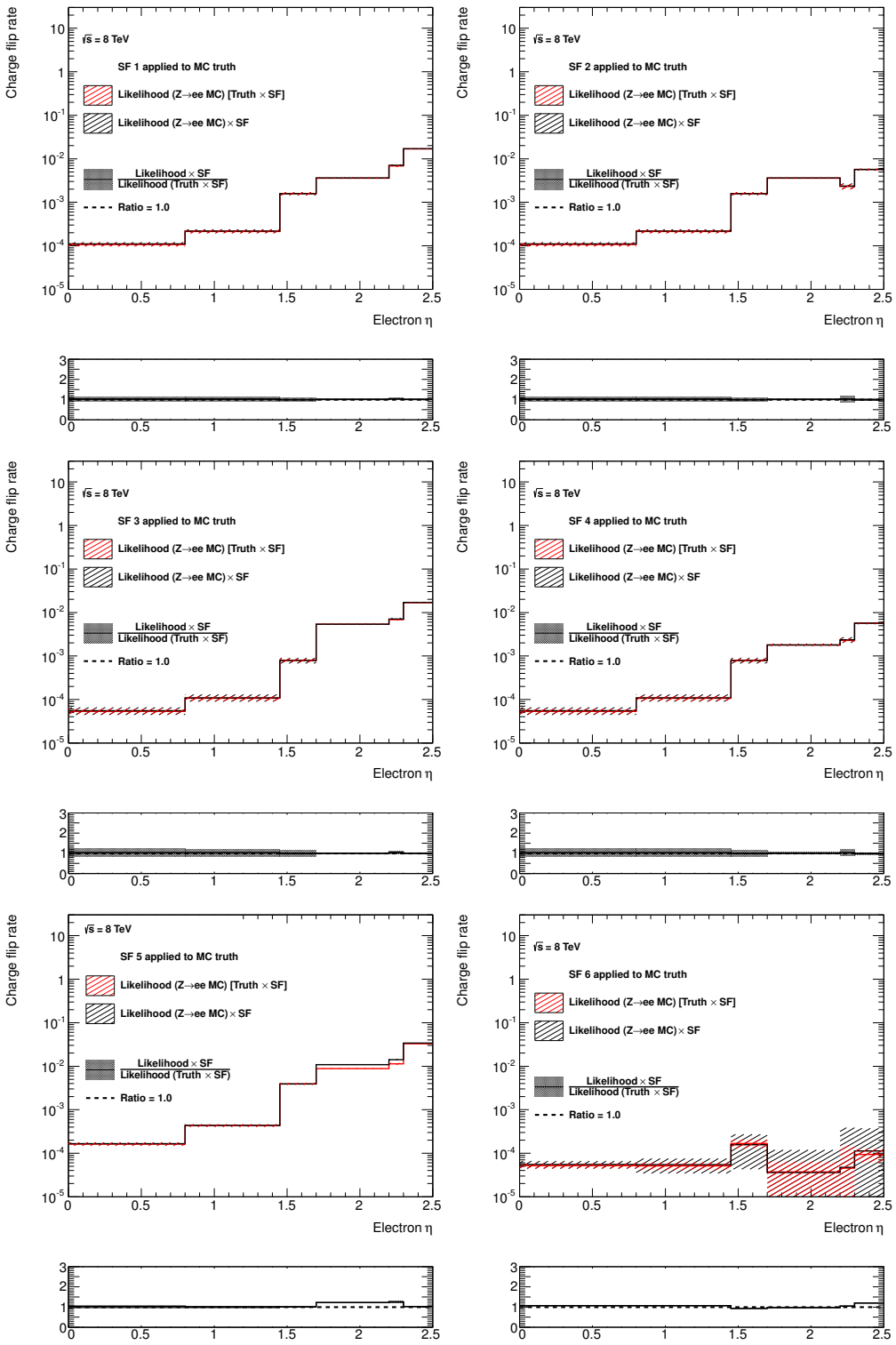

Figure 9.22: The result of applying the arbitrary scale factors in Figure 9.21 to MC before applying Likelihood Method, compared with the rate measured by using the Likelihood method with unscaled MC which then has the scale factors applied.

Measurement of the electron charge-flip rate

The charge-flip rates measured in data and MC by minimising the likelihood function L are shown in Figure 9.23. The rate measured in data includes a subtraction of non-prompt contamination in this region, measured using the method detailed in Section 9.2. The charge-flip rate measured in data is lower than in MC, although the shape of the distributions are similar. The bias that is measured in MC is shown by the red distribution in the lower-part of Figure 9.23. The charge-flip rate that is used in the analysis is applied by taking the ratio of the measurement in data and MC and applying this scale factor, shown in Figure 9.24, to MC electrons that have a charge-flip confirmed using MC truth information. The advantage of doing this, as discussed in the previous section, is that the bias produced by measuring the charge-flip rates by minimising L is cancelled and the effective charge-flip rate that is used matches the true rate in data. Additionally this implementation takes the p_T dependence of the charge-flip probability from MC, as it is otherwise ignored in this method. The blue dashed line in Figure 9.23 shows the estimated true charge-flip rate in data by applying the scale-factor to the MC truth.

Systematic uncertainties in the charge-flip scale factors are assigned to cover the statistical uncertainty in minimising L (Equation 9.7) combined with the uncertainty in modelling the non-prompt background, which changes the number of events used to measure the charge-flip rate. The relative size of the uncertainty in the charge-flip backgrounds is indicated in Figure 9.24 and also discussed in Section 10.1.

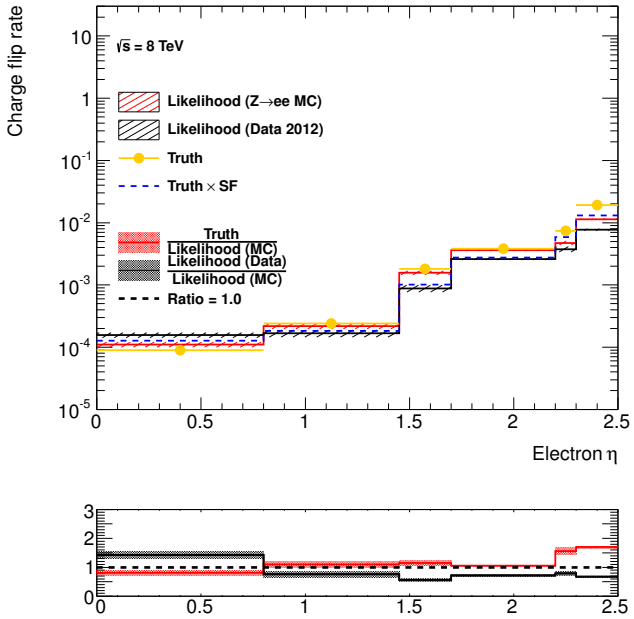

Figure 9.23: The electron charge-flip rate measured as a function of η in by minimising likelihood L in data (black) and in MC (red). The charge-flip rate as measured with MC truth is shown in yellow. The observed bias in MC is shown in the lower figure in red and the ratio between the measured rates in data and MC is shown in the lower figure in black. The blue dashed line in the upper figure is the charge-flip rate measured with MC truth scaled by the measured ratio of data to MC.

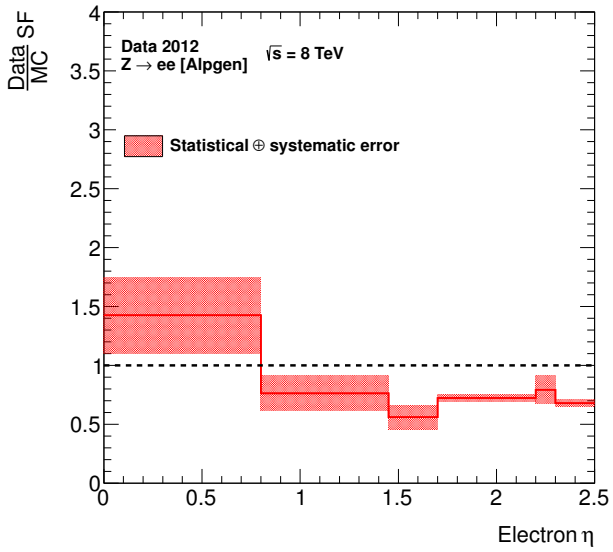

Figure 9.24: Scale factors of the electron charge-flip rate measured by minimising likelihood L as a function of electron $|\eta|$ in data and MC.

9.3.2 Muon charge-flips

Muon objects in this analysis are composed of a track combined from measurements in the ID and MS subdetectors as described in Section 7.3. In addition to the combined measurements of muon momentum, trajectory and charge, the muon objects retain the corresponding measurements determined independently using the individual MS and ID systems. As detailed in Section 7.3.1, muon objects in this analysis are required to have a charge measurement which is consistent with both of the independent ID and MS measurements:

$$q_{\mathrm{ID}} = q_{\mathrm{MS}}$$

and are otherwise rejected. Consequently only muons with a simultaneous MS and ID charge-flip will pass the SS selection. No muon objects with a charge-flip defined in this way are observed for muons in $Z \to \mu\mu$ MC so a data-driven approach is used. In this method, the independent measurements of the MS and ID charge-flip rates are fundamental to the measurement of the total muon charge-flip rate.

Events are selected with exactly two muons which satisfy the *tight* criteria, except there is no requirement for the MS and ID charge measurements to be consistent. The mass of the dimuon system is also required to satisfy the condition $|m_{\mu\mu} - m_Z| < 10$ GeV, where m_Z is the Z boson mass. The Tag-and-Probe Method, which is presented in Section 7.7.1, is used by labelling the two muons (in any order) from $Z \to \mu\mu$ events as μ_1 and μ_2 with the following conditions:

- If μ_1 has matching charges measured in the ID and MS then it is selected as a tag muon. The ID and MS tracks of μ_2, labelled μ_2^{ID} and μ_2^{MS} respectively, are now considered separately in order to measure the charge-flip rate in the ID and MS.

- In order to consider μ_2^{MS} as a probe, the charge of μ_2^{ID} is required to be opposite to μ_1. If μ_2^{MS} is a probe, then the charge-flip rate of the MS is measured with respect to μ_2^{ID}.

- In order to consider μ_2^{ID} as a probe, the charge of μ_2^{MS} is required to be

opposite to μ_1. If μ_2^{ID} is a probe, then the charge-flip rate of the ID is measured with respect to μ_2^{MS}.

The process is then repeated by switching the roles of μ_1 and μ_2. The requirement to measure the charge-flip rate of the ID track with respect to the MS kinematics (and vice-versa) is imposed as charge-flips for muons are considered to be primarily due to the resolution of the subdetectors. It therefore follows that if the charge of a muon object has been incorrectly assigned by a subdetector it is likely that the object's p_T has also been mismeasured.

The charge-flip rate in MS tracks is measured to be less than 5.0% for muons with $p_T < 400$ GeV and less than 0.1% for muons with $p_T < 100$ GeV as shown in Figure 9.25. There is no charge-flip observed in the ID so limits are set at 68% Confidence Level (CL) using a binomial approach to the statistics on the combined (MS+ID) muon charge-flip rate with a central value of zero. The measured CLs ϵ^{CL} are applied, in place of a non-zero muon charge-flip rate, to OS $Z \to \mu\mu$ muons in MC in order to provide an upper limit on the number of muon charge-flip events in the signal region. The rates are applied per event to the MC as a weight w:

$$w = \epsilon^{\mathrm{CL}}(p_T^1) + \epsilon^{\mathrm{CL}}(p_T^2) \tag{9.10}$$

where p_T^1 and p_T^2 are the transverse momenta of the two muons in the event.

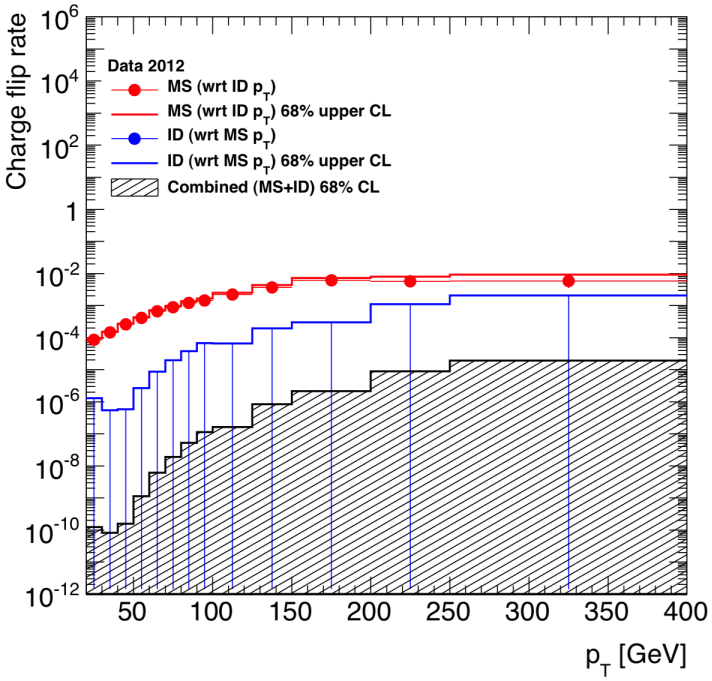

Figure 9.25: Muon charge-flip rate as a function of p_T as measured in data. Circular points indicate measured rates and horizontal solid lines indicate 68% Confidence Level limits based on data statistics. The area filled with diagonal lines represents the Confidence Level limits on the combined (MS+ID) charge-flip rate. The ID charge-flip rate is measured to be consistent with zero. The blue circles are therefore not visible on this figure.

Chapter 10

Systematic uncertainties

The sources of systematic uncertainty in the modelling of signal and background are grouped into those due to the MC simulation, signal-specific modelling uncertainties and uncertainties associated with data-driven backgrounds (charge-flip and non-prompt processes). These uncertainties are discussed in the following sections.

10.1 Uncertainties in MC simulation

Systematic uncertainties for MC are evaluated by considering the following sources:

- Lepton scale factors - presented in Section 7.7.3. For both muons and electrons these are approximately 3%.
- Muon correction factors - The momentum resolution and scale of muon tracks are corrected to match the measurements in data, as detailed in Section 7.7.2, using correction factors provided by the ATLAS MCP group [77], who also provide associated systematic uncertainties. The correction factors are varied by $\pm 1\sigma$ uncertainties for the ID and MS momentum measurements, which corresponds to a change of approximately 1% in the total background yields.
- Electron correction factors - The energy scale and resolution of electrons is corrected with factors provided by the ATLAS E/gamma Performance Group (Section 7.7.2). The correction factors are varied by

their $\pm 1\sigma$ uncertainties, which corresponds to a change of approximately 2% in the total background yields.

- Jet Energy Scale (JES) - The systematic uncertainty associated with the Jet Energy Scale is provided by the ATLAS Jet/Etmiss performance group. The group provides the JES uncertainties as a function of jet p_T and η. The uncertainties take into account the effect of pile-up on a per event basis according to the number of vertices found in the event. The uncertainty on the total number of background events is approximately 10%.

- Jet Energy Resolution (JER) - The systematic uncertainty on the Jet Energy Resolution is measured by the ATLAS Jet/Etmiss performance group. The uncertainties are applied by varying the resolution of jet p_T. The net effect on the total number of background events is approximately a 1%.

- Trigger efficiency scale factors - The lepton trigger scale factor uncertainties are applied to Monte Carlo as recommended by the ATLAS Muon Trigger group (Section 7.7.3). The uncertainty on these scale factors is applied to the MC, and the overall uncertainty on the yield in the signal region is approximately 0.1%.

- Normalisation of the diboson background - The uncertainty on the diboson contribution is calculated by comparing MC to data as discussed in Section 9.1. The total effect of the uncertainty on the total number of background events is approximately 5%.

- Normalisation of other SS background processes - The background from ttV, Higgs and SS WW production are taken from the uncertainty of cross-sections as discussed in Section 9.1.2. The total effect of these uncertainties on the expected number of background events is approximately 5%.

- MC statistical uncertainty - the total statistical uncertainty in background MC samples in the signal regions is approximately 1%.

- The uncertainty on the integrated luminosity is ±2.8%. It is derived from a preliminary calibration of the luminosity scale derived from beam-separation scans performed in November 2012 [100]. This uncertainty is applied to MC backgrounds, as they are weighted to match the luminosity measured in data.

10.2 Signal-specific modelling uncertainties

In addition to uncertainties associated with MC simulation, an uncertainty is considered for the signal MC to reflect the choice of parton shower. The nominal parton shower that is used for all signal MC samples is `Pythia`. The total number of events in the signal region using the signal MC interfaced to `Pythia` is compared to the number of events in the signal MC interfaced to `HERWIG`. The difference is measured to be approximately 5%.

A systematic uncertainty is also considered to cover the effect of using the Atlfast-II detector simulation for the signal MC rather than Geant4 which is used for all other MC samples. The efficiency to select signal events is compared between the two detector simulations. The difference in the efficiency is assigned as an uncertainty, which is approximately 4%.

10.3 Uncertainties in data-driven backgrounds

The systematic uncertainties which are applied to data-driven backgrounds are discussed here.

For the electron charge-flip measurement the limited data statistics used to evaluate the charge-flip rate are taken as one source of uncertainty. Another source of uncertainty is due to the subtraction of non-prompt background that is performed to purify the sample of SS leptons used in the method. The effect of the uncertainty on the charge-flip rate on the total background yields is approximately 6%.

For the non-prompt background estimate, the effect of the uncertainties de-

tailed in Section 9.2 on the total number of non-prompt background events is approximately 20-30%. The uncertainty due to the non-prompt background estimate on the total background is approximately 1.5%, 8% and 8% in the ee, $\mu\mu$ and $e\mu$ channels respectively. As discussed, in the electron channel the non-prompt contribution is correlated with the charge-flip estimation. This correlation is taken into account when calculating the uncertainty on the total background.

10.4 Discussion of systematic uncertainties

An overview of the systematic uncertainties in the signal region for background events is presented in Table 10.1. In the ee channel, the largest source of systematic uncertainty is due to the JES, which is also notably asymmetric. This is in part due to limited statistics, which is reflected by the large statistical uncertainty in this channel, but also because the number of events in the signal region is highly sensitive to the jet p_T due to the cut on m_{jj}. In the $\mu\mu$ channel, the largest sources of uncertainty are due to the non-prompt estimate, the MC normalisation uncertainty and the statistical uncertainty. The largest uncertainty in the $e\mu$ channel is from the non-prompt estimate.

The systematic uncertainties for signal events (with $m_N = 200$ GeV) in the signal region are presented in Table 10.2. The dominant source of uncertainty in all three channels is from the JES which reflects the sensitivity of the signal events to m_{jj} and jet p_T. There is also a considerable uncertainty due to the signal modelling from the choice of PDF, parton shower and detector simulation.

Source of uncertainty	Uncertainty on total background [%]		
	ee	$\mu\mu$	$e\mu$
Charge flip method	+ 6.61 / - 6.57	± 0.00	+ 0.61 / - 0.15
Electron ID	+ 1.30 / - 1.24	-	+ 0.37 / - 0.16
Electron Iso SF	+ 0.46 / - 0.08	-	+ 0.36 / - 0.00
Electron Reco	+ 0.87 / - 0.80	-	+ 0.34 / - 0.09
Electron Scale	+ 0.32 / - 0.00	-	+ 0.32 / - 0.00
Electron Smearing	+ 0.79 / - 0.40	-	+ 0.32 / - 0.02
Non-prompt	+ 5.85 / - 5.85	+ 12.2 / - 12.3	+ 30.2 / - 29.7
JER	± 4.30	± 2.88	± 0.95
JES	+ 8.27 / - 22.4	+ 6.80 / - 12.2	+ 2.16 / - 2.76
JVF	+ 1.58 / - 6.20	+ 4.35 / - 5.01	+ 1.37 / - 0.94
Luminosity	+ 1.70 / - 1.66	± 1.33	+ 0.54 / - 0.41
MET	+ 1.51 / - 2.76	+ 6.18 / - 3.00	+ 0.71 / - 0.49
Muon ID	-	+ 0.65 / - 2.21	+ 0.45 / - 0.12
Muon Iso SF	-	+ 1.92 / - 1.88	+ 0.45 / - 0.29
Muon Reco	-	± 0.19	+ 0.32 / - 0.04
Muon Scale	-	+ 0.00 / - 0.22	+ 0.32 / - 0.00
Normalisation	+ 2.20 / - 2.14	± 10.1	± 2.75
Statistical	± 15.2	± 11.1	± 9.65
Total Uncertainty	+ 19.5 / - 29.1	+ 21.3 / - 23.9	+ 31.9 / - 31.5

Table 10.1: Uncertainty breakdown for backgrounds in the signal region, defined as events containing two SS leptons, $E_T^{\text{miss}} < 40$ GeV and two jets satisfying $|m_{jj} - 80| < 20$ GeV. The total uncertainty is calculated by combining all uncertainties in quadrature.

Source of uncertainty	Uncertainty on signal [%]		
	ee	$\mu\mu$	$e\mu$
Electron ID	+ 1.96 / - 1.94	-	± 0.96
Electron Iso SF	+ 0.81 / - 0.24	-	+ 0.39 / - 0.09
Electron Reco	+ 1.32 / - 1.31	-	± 0.65
Electron Scale	± 0.00	-	± 0.00
Electron Smearing	+ 0.00 / - 0.61	-	+ 0.14 / - 0.00
Fast Simulation	± 5.00	± 4.00	± 3.00
JER	± 2.94	± 2.82	± 3.63
JES	± 13.1	± 13.4	± 14.8
JVF	+ 1.22 / - 1.07	+ 2.18 / - 0.00	+ 1.70 / - 0.54
MET	+ 1.22 / - 2.23	+ 1.25 / - 2.12	+ 1.15 / - 2.01
Muon ID	-	+ 0.00 / - 0.19	+ 0.04 / - 0.05
Muon Iso SF	-	+ 4.04 / - 3.96	± 2.00
Muon Reco	-	± 0.42	± 0.29
Muon Scale	-	+ 0.16 / - 0.07	+ 0.05 / - 0.09
PDF	± 4.00	± 4.00	± 4.00
Parton Shower	± 6.00	± 5.50	± 6.00
Statistical	± 3.41	± 1.80	± 2.20
Total Uncertainty	+ 16.7 / - 16.8	+ 16.6 / - 16.5	± 17.6

Table 10.2: Uncertainty breakdown on the signal ($m_N = 200$ GeV) in the signal region, defined as event containing two SS leptons, $E_T^{\text{miss}} < 40$ GeV and two jets satisfying $|m_{jj} - 80| < 20$ GeV.

Chapter 11

Background validation

The methods used to estimate the background contributions presented in Chapter 9 are validated by selecting control regions which have a composition of events that is similar to the signal region. The validation is performed by comparing the total number of events predicted and measured in the control regions, and by considering kinematic distributions in order to ensure that background processes are well modelled. There are four control regions defined in this chapter which are required to contain exactly two leptons with SS electric charge and exclude events that would satisfy the signal region selection criteria presented in Section 8.3. The control regions are briefly introduced here and described in further detail in Sections 11.1 - 11.4.

Control Regions 1, 2 and 3 are required to contain events with two SS leptons from $\{ee, \mu\mu, e\mu\}$ and to contain zero, one and two jets respectively. These control regions are similar to the signal region in terms of the composition of predicted processes. Control Region 4 is additionally defined for $\mu\mu$ events and is primarily composed of events containing non-prompt muons. With the exception of Control Region 4, which allows subleading muon $p_T > 10$ GeV, all control regions adhere to the general event selection described in Section 8.2.

Any deviation between the number of events measured in data and the predicted number of events is quantified in terms of the significance S, which is defined as:

$$S = \frac{N^{\text{data}} - N^{\text{bkg}}}{\sqrt{(\sigma^{\text{data}})^2 + (\sigma^{\text{bkg}})^2}}$$

where N^{data} and N^{bkg} are the number of data and predicted events respectively, and σ^{data} and σ^{bkg} are the statistical uncertainty on the data and the total uncertainty on the prediction respectively. A control region with $|S| < 1$ is interpreted as having good agreement between the predicted and measured number of events. Control regions with $|S| < 2$ are regarded as satisfactory, as long as the deviation is not observed across multiple control regions. Control regions measured with a deviation corresponding to $|S| > 2$ would indicate that the predicted number of events requires further understanding. One should note that the significance S is not a measure of the p-value presented in Section 12.2.1 and as such is not interpreted in the same manner.

11.1 Control Region 1

This control region contains events with two SS leptons and zero jets. The requirement for zero jets means that this control region already excludes events in the signal region without implementing additional cuts.

A comparison of the kinematics of predicted events with data in the ee channel is presented in Figure 11.1(a) and (b). The modelling of the charge-flip rate, detailed in Section 9.3.1, is parameterised in electron η which leads to an accurate description of the observed number of events as a function of η. The peak of the ee mass is shifted below m_Z due to the energy loss of electrons that have emitted a hard bremsstrahlung photon. This is shown in Figure 11.1(b), where good agreement between data and background is observed.

The modelling of the diboson background is tested most thoroughly in $\mu\mu$ events as the fraction of events in this channel from non-prompt decays is relatively small compared to the corresponding $e\mu$ events. Kinematic distributions for the $\mu\mu$ channel are shown Figures 11.1(c) and (d). Figure 11.1(d)

shows the invariant mass of the $\mu\mu$ system which peaks at $m_{\mu\mu} \approx 80$ GeV and drops smoothly towards high $m_{\mu\mu}$, as predicted in MC simulation and observed in data.

The non-prompt background prediction constitutes the largest background in the $e\mu$ channel. There is good agreement between the predicted and observed kinematic distributions in Figures 11.1(e) and (f).

The significance S in the ee, $\mu\mu$ and $e\mu$ channels is calculated to be -1.28, 0.60 and -0.22 respectively. The total prediction and data yields are given in Table 11.1. There are no large discrepancies in the kinematic distributions and the measured values of significance imply consistency between the predicted and measured yields. The systematic uncertainties on the prediction given in terms of the relative uncertainty on the total background are presented in Table 11.2. The total uncertainty on the prediction in each channel is approximately 11% to 17% with the largest contributions being due to the JES uncertainty, the charge-flip background and the non-prompt background. It should be noted that the JES uncertainty affects this control region by altering the lepton isolation efficiency and the number of jets that pass the minimum p_T requirement.

Process	Event yields ± Stat. ± Syst.		
	ee	$\mu\mu$	$e\mu$
Higgs	$0.11 \pm 0.05\ ^{+0.02}_{-0.03}$	$0.05 \pm 0.00\ ^{+0.01}_{-0.01}$	$0.07 \pm 0.01\ ^{+0.01}_{-0.01}$
Non-prompt	$526 \pm 20\ ^{+200}_{-190}$	$18.1 \pm 1.8\ ^{+5.9}_{-7.4}$	$304 \pm 12\ ^{+75}_{-71}$
SSWW	$0.40 \pm 0.13\ ^{+0.2}_{-0.21}$	$0.48 \pm 0.15\ ^{+0.27}_{-0.25}$	$1.13 \pm 0.26\ ^{+0.62}_{-0.64}$
Top	$0.88 \pm 0.5\ ^{+0.16}_{-0.57}$	$0.00 \pm 0.00\ ^{+0.00}_{-0.00}$	$0.45 \pm 0.31\ ^{+0.18}_{-0.06}$
WW	$2.65 \pm 0.39\ ^{+0.44}_{-0.52}$	$0.00 \pm 0.00\ ^{+0.00}_{-0.00}$	$4.9 \pm 0.52\ ^{+0.76}_{-0.76}$
WZ	$39.9 \pm 2.1\ ^{+6.1}_{-5.9}$	$99.5 \pm 3.4\ ^{+15.4}_{-13.3}$	$118 \pm 4\ ^{+16}_{-14}$
Z+jets	$2680 \pm 64\ ^{+300}_{-310}$	< 0.02	$6.88 \pm 4.1\ ^{+0.4}_{-0.39}$
ZZ	$12.9 \pm 0.92\ ^{+3.5}_{-1.3}$	$22.1 \pm 1.3\ ^{+3.3}_{-2.8}$	$27.7 \pm 1.4\ ^{+3.7}_{-3.3}$
ttV	$0.01 \pm 0.01\ ^{+0.00}_{-0.01}$	$0.01 \pm 0.01\ ^{+0.00}_{-0.00}$	$0.01 \pm 0.01\ ^{+0.00}_{-0.00}$
Signal MC $m_N = 120$ GeV	$1.88\ ^{+0.37}_{-0.52}$	$1.24\ ^{+0.25}_{-0.46}$	$1.18\ ^{+0.27}_{-0.43}$
Total background	$3260 \pm 67\ ^{+360}_{-370}$	$140 \pm 4\ ^{+17}_{-15}$	$462 \pm 13\ ^{+77}_{-73}$
Data	2777	153	444
Significance	-1.28	0.60	-0.22

Table 11.1: Total event yields for events with two SS leptons and zero jets. Backgrounds contributing < 0.01 events in all three channels are omitted. The number of signal events shown assumes a coupling $|V_{lN}|^2$ equal to the expected limit in the case that no signal is observed.

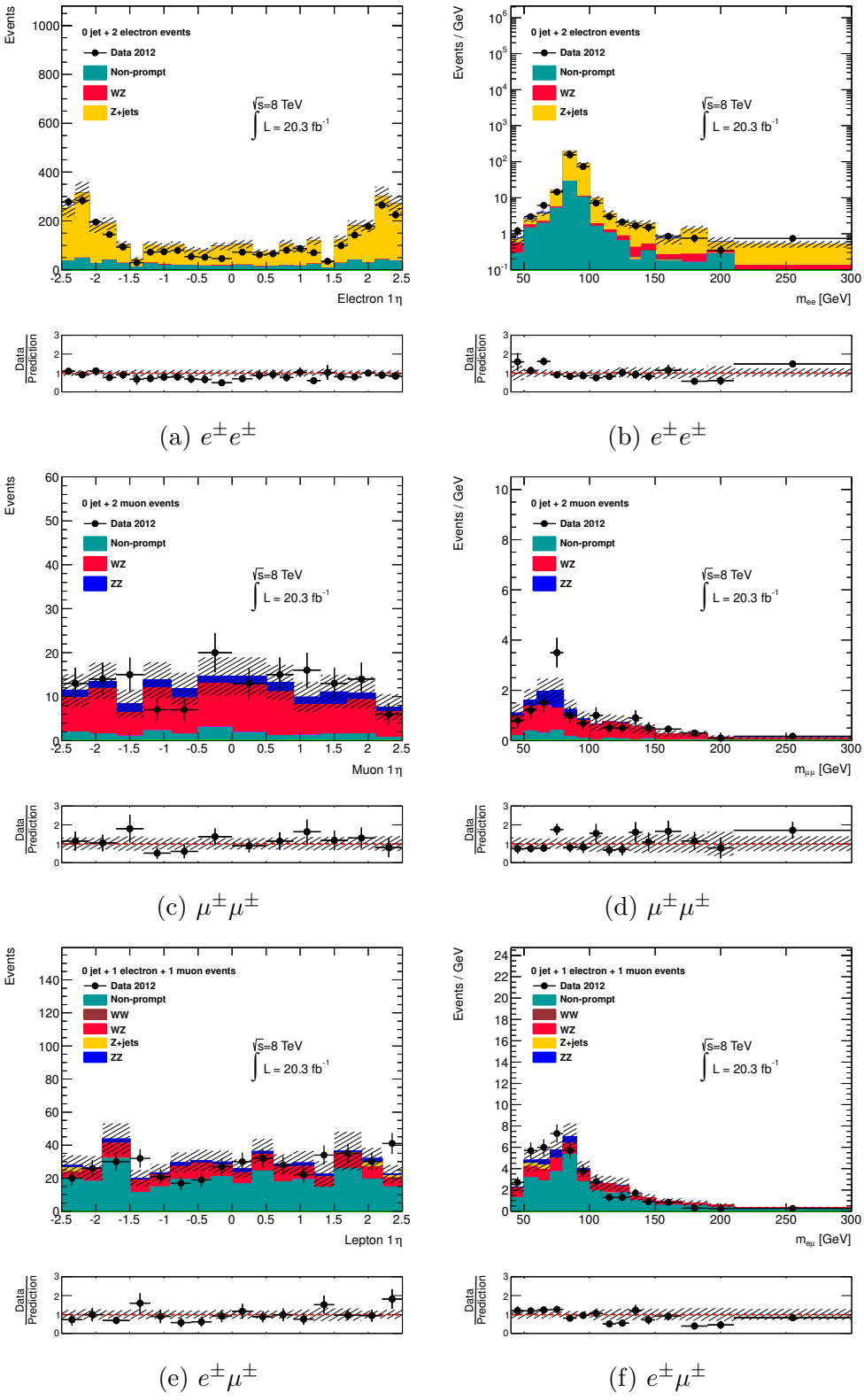

(a) $e^{\pm}e^{\pm}$ (b) $e^{\pm}e^{\pm}$

(c) $\mu^{\pm}\mu^{\pm}$ (d) $\mu^{\pm}\mu^{\pm}$

(e) $e^{\pm}\mu^{\pm}$ (f) $e^{\pm}\mu^{\pm}$

Figure 11.1: Leading lepton η distribution (left) and invariant mass of two leading leptons (right) for events with two SS leptons and zero jets (Control Region 1).

Source of uncertainty	Uncertainty on total background [%]		
	ee	$\mu\mu$	$e\mu$
Charge flip method	± 7.14	± 0.00	± 0.13
Electron ID	+ 1.81 / - 1.79	-	± 0.30
Electron Iso SF	+ 0.44 / - 0.17	-	+ 0.07 / - 0.03
Electron Reco	+ 1.1 / - 1.09	-	± 0.17
Electron Scale	+ 0.02 / - 0.00	-	± 0.00
Electron Smearing	+ 0.16 / - 0.05	-	+ 0.00 / - 0.13
Non-prompt	+ 6.27 / - 6.18	+ 4.19 / - 5.24	+ 16.2 / - 15.4
JER	± 0.04	± 0.35	± 0.44
JES	+ 4.39 / - 4.14	+ 7.73 / - 5.56	+ 2.47 / - 1.74
JVF	+ 1.19 / - 3.31	+ 3.69 / - 3.28	+ 0.82 / - 0.97
Luminosity	± 2.3	± 2.03	± 0.73
Muon ID	-	+ 0.14 / - 0.49	+ 0.01 / - 0.02
Muon Iso SF	-	+ 2.94 / - 2.88	± 0.52
Muon Reco	-	± 0.30	± 0.07
Muon Scale	-	+ 0.32 / - 0.43	± 0.00
Normalisation	± 0.10	± 6.03	± 2.17
Statistical	± 2.06	± 2.91	± 2.83
Total Uncertainty	+ 11.2 / - 11.5	+ 12.2 / - 11.3	+ 16.9 / - 16.0

Table 11.2: Uncertainty breakdown in events with two SS leptons and zero jets.

11.2 Control Region 2

Control Region 2 contains events with two SS leptons and one jet. In order to exclude events in the LRSM signal, which is described in Section 3.6, a cut on the invariant mass of the two leptons and one jet is required to satisfy $m_{\ell\ell j} < 400$ GeV.

Before considering the effect of the isolation and other selection cuts, the requirement for one jet means that Control Region 2 has fewer VV and $Z \to \ell\ell$ events due to additional QCD coupling terms in the respective interactions. Although this means that this control region provides a less statistically robust test of the background modelling than Control Region 1, events containing jets are more similar to the signal region, which contains at least two jets, so it is important that this region is well modelled.

The number of measured data events and the predicted background composition is presented in Table 11.3 and the kinematic distributions are presented in Figure 11.2. There is good agreement between the predicted and observed kinematics. The significance S in the ee, $\mu\mu$ and $e\mu$ channels is calculated to be -0.87, -0.93 and -0.88 respectively. Therefore it is interpreted that the prediction is consistent with the data. The total uncertainty on the prediction, presented in Table 11.4, is approximately 10% to 13% in the ee and $\mu\mu$ channels and approximately 20% in the $e\mu$ channel. The largest contributions to the total uncertainty come from the measurements of the charge-flip and non-prompt backgrounds and the JES.

Process	Event yields ± Stat. ± Syst.		
	ee	$\mu\mu$	$e\mu$
Higgs	$0.18 \pm 0.08\ ^{+0.04}_{-0.04}$	$0.05 \pm 0.00\ ^{+0.01}_{-0.01}$	$0.12 \pm 0.01\ ^{+0.02}_{-0.02}$
Non-prompt	$191 \pm 11\ ^{+66}_{-65}$	$15.4 \pm 1.6\ ^{+5.8}_{-5.9}$	$230 \pm 11\ ^{+81}_{-79}$
SSWW	$1.2 \pm 0.25\ ^{+0.75}_{-0.63}$	$3.65 \pm 0.44\ ^{+2.0}_{-2.0}$	$4.93 \pm 0.52\ ^{+2.6}_{-2.5}$
Top	$2.4 \pm 1.0\ ^{+1.1}_{-0.33}$	$0.00 \pm 0.00\ ^{+0.00}_{-0.00}$	$6.28 \pm 1.4\ ^{+1.2}_{-1.0}$
WW	$0.86 \pm 0.19\ ^{+0.28}_{-0.14}$	$0.00 \pm 0.00\ ^{+0.00}_{-0.00}$	$1.83 \pm 0.3\ ^{+0.3}_{-0.28}$
WZ	$40.8 \pm 2.1\ ^{+2.6}_{-3.0}$	$57.3 \pm 2.5\ ^{+4.7}_{-4.9}$	$90.7 \pm 3.2\ ^{+5.7}_{-5.9}$
Z+jets	$829 \pm 27\ ^{+120}_{-100}$	< 0.02	$2.35 \pm 1.4\ ^{+0.29}_{-0.66}$
ZZ	$9.14 \pm 0.79\ ^{+1.9}_{-0.5}$	$7.75 \pm 0.76\ ^{+0.94}_{-1.5}$	$15.8 \pm 1.1\ ^{+1.5}_{-1.1}$
ttV	$0.09 \pm 0.02\ ^{+0.06}_{-0.03}$	$0.15 \pm 0.03\ ^{+0.06}_{-0.06}$	$0.23 \pm 0.04\ ^{+0.11}_{-0.07}$
Signal MC $m_N = 120$ GeV	$11.4\ ^{+1.30}_{-2.00}$	$6.88\ ^{+0.87}_{-1.29}$	$6.95\ ^{+0.95}_{-1.14}$
Total background	$1070 \pm 29\ ^{+140}_{-120}$	$84.4 \pm 3.1\ ^{+7.7}_{-8.0}$	$352 \pm 11\ ^{+81}_{-79}$
Data	946	73	278
Significance	-0.87	-0.93	-0.88

Table 11.3: Total event yields for events with two SS leptons, one jet and $m_{lljj} < 400$ GeV. Backgrounds contributing < 0.01 events in all three channels are omitted. The number of signal events shown assumes a coupling $|V_{lN}|^2$ equal to the expected limit in the case that no signal is observed.

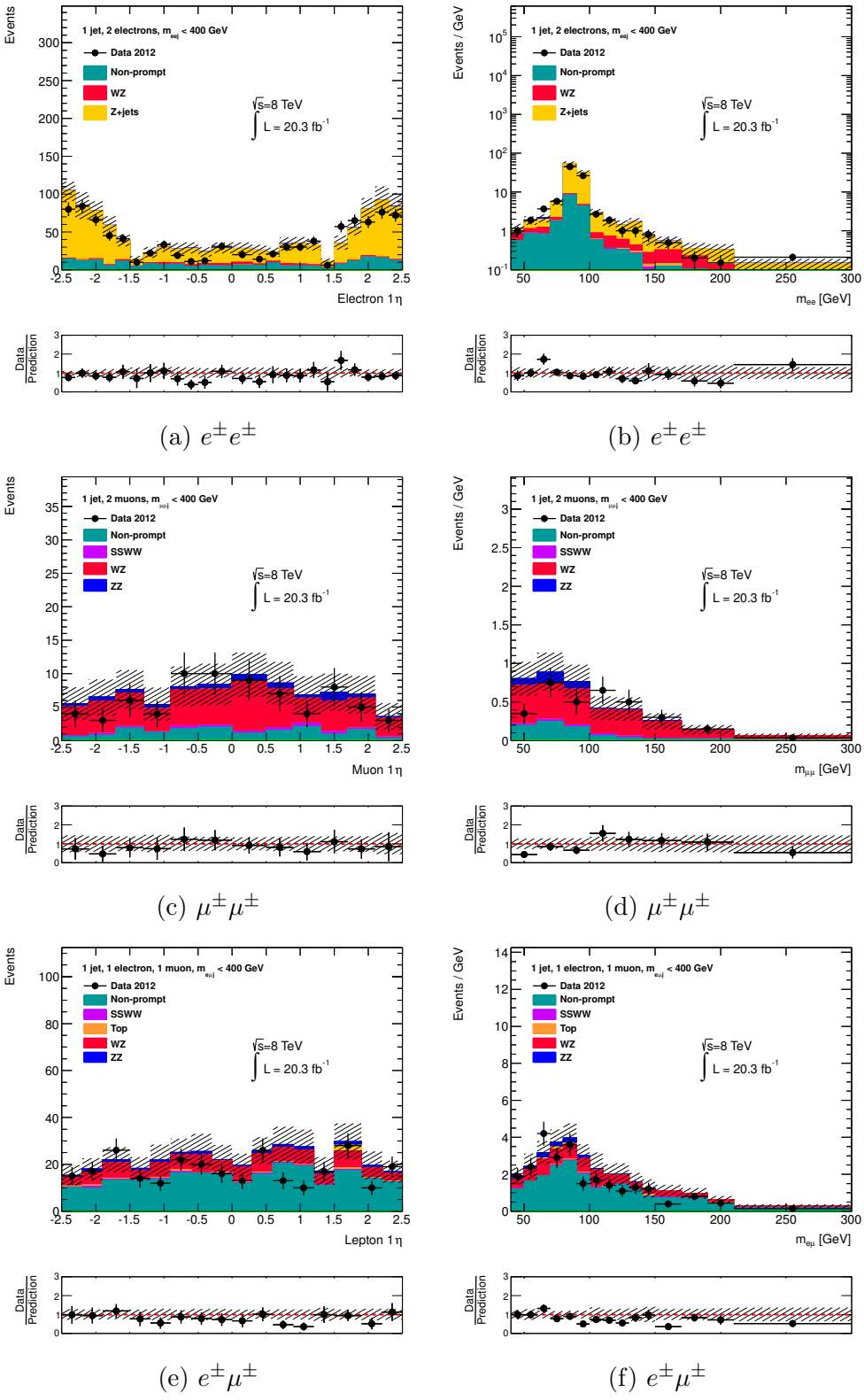

(a) $e^{\pm}e^{\pm}$ (b) $e^{\pm}e^{\pm}$

(c) $\mu^{\pm}\mu^{\pm}$ (d) $\mu^{\pm}\mu^{\pm}$

(e) $e^{\pm}\mu^{\pm}$ (f) $e^{\pm}\mu^{\pm}$

Figure 11.2: Leading lepton η distribution (left) and invariant mass of two leading leptons (right) for events with two SS leptons, one jet and $m_{lljj} < 400$ GeV (Control Region 2).

Source of uncertainty	Uncertainty on total background [%]		
	ee	$\mu\mu$	$e\mu$
Charge flip method	± 6.78	± 0.00	+ 0.30 / - 0.12
Electron ID	+ 1.73 / - 1.71	-	+ 0.31 / - 0.28
Electron Iso SF	+ 0.36 / - 0.21	-	+ 0.16 / - 0.03
Electron Reco	+ 1.03 / - 1.02	-	+ 0.22 / - 0.17
Electron Scale	+ 0.04 / - 0.00	-	+ 0.14 / - 0.00
Electron Smearing	+ 0.06 / - 0.08	-	+ 0.14 / - 0.06
Non-prompt	+ 6.36 / - 6.25	+ 6.88 / - 6.94	+ 23.0 / - 22.4
JER	± 0.33	± 1.27	± 0.35
JES	+ 5.94 / - 5.45	+ 0.69 / - 3.81	+ 0.59 / - 0.72
JVF	+ 6.23 / - 2.13	+ 3.22 / - 0.22	+ 0.27 / - 0.08
Luminosity	± 2.16	± 1.92	+ 0.75 / - 0.73
Muon ID	-	+ 0.15 / - 0.14	+ 0.21 / - 0.01
Muon Iso SF	-	+ 2.78 / - 2.72	+ 0.54 / - 0.52
Muon Reco	-	± 0.29	+ 0.16 / - 0.07
Muon Scale	-	+ 0.13 / - 0.11	+ 0.15 / - 0.02
Normalisation	± 0.19	± 3.88	± 1.44
Statistical	± 2.72	± 3.69	± 3.24
Total Uncertainty	+ 13.3 / - 11.6	+ 10.0 / - 10.2	+ 23.3 / - 22.7

Table 11.4: Uncertainty breakdown in events with two SS leptons, one jet and $m_{lljj} < 400$ GeV.

11.3 Control Region 3

Control Region 3 is defined as containing two SS leptons and two jets. In order to reject events in the LRSM signal region, as described in Section 3.6, a cut on the invariant mass of the two leptons is required such that $m_{\ell\ell} < 110$ GeV. Furthermore as events with two jets are in the signal region of this analysis it is required that the mass of the two jets satisfies $|m_{jj} - m_W| > 20$ GeV.

As there are extensive cuts in this control region, the number of predicted and measured events is small, typically less than 10% of the yields measured in Control Region 1. Because of this, it is less important to assess the shape of the kinematic distributions in this region, which are shown in Figure 11.3, and more emphasis is placed on the consistency between the total predicted and measured yields as detailed in Table 11.5. The significance S in the ee, $\mu\mu$ and $e\mu$ channels is calculated to be -1.17, -1.27 and 0.48 respectively, so it is interpreted that the predicted and measured yields are consistent.

The total uncertainty on the prediction is presented in Table 11.6, with the uncertainty on the prediction in each channel being approximately 15% to 30%. In the $\mu\mu$ channel limited statistics in the MC simulation leads to an artificially asymmetric uncertainty on the JES of approximately $+2\%/-22\%$. The limited statistics particularly affects the JES in this control region due to the cut on m_{jj} which is sensitive to fluctuations in jet energy. Other than the statistical uncertainty, the largest sources of uncertainty are due the non-prompt and charge-flip backgrounds.

Process	Event yields ± Stat. ± Syst.		
	ee	$\mu\mu$	$e\mu$
Higgs	$0.00 \pm 0.00 \,^{+0.00}_{-0.00}$	$0.00 \pm 0.00 \,^{+0.00}_{-0.00}$	$0.01 \pm 0.00 \,^{+0.00}_{-0.00}$
Non-prompt	$7.66 \pm 2.3 \,^{+3.8}_{-3.8}$	$2.07 \pm 0.61 \,^{+0.76}_{-0.74}$	$11.9 \pm 2.3 \,^{+5.0}_{-4.9}$
SSWW	$0.13 \pm 0.09 \,^{+0.12}_{-0.12}$	$0.26 \pm 0.13 \,^{+0.24}_{-0.15}$	$0.49 \pm 0.17 \,^{+0.25}_{-0.32}$
Top	$0.20 \pm 0.12 \,^{+0.03}_{-0.2}$	$0.00 \pm 0.00 \,^{+0.00}_{-0.00}$	$0.53 \pm 0.42 \,^{+0.11}_{-0.13}$
WZ	$1.56 \pm 0.42 \,^{+0.26}_{-0.56}$	$6.62 \pm 0.88 \,^{+1.1}_{-2.3}$	$5.04 \pm 0.74 \,^{+1.3}_{-0.94}$
Z+jets	$68.9 \pm 6.7 \,^{+12.8}_{-8.4}$	< 0.002	$0.27 \pm 0.27 \,^{+0.01}_{-0.01}$
ZZ	$0.41 \pm 0.19 \,^{+0.17}_{-0.33}$	$0.41 \pm 0.17 \,^{+0.24}_{-0.25}$	$1.04 \pm 0.28 \,^{+0.24}_{-0.23}$
ttV	$0.00 \pm 0.00 \,^{+0.00}_{-0.00}$	$0.07 \pm 0.02 \,^{+0.04}_{-0.04}$	$0.07 \pm 0.02 \,^{+0.04}_{-0.03}$
Signal MC $m_N = 120$ GeV	$0.89 \,^{+0.14}_{-0.17}$	$0.91 \,^{+0.25}_{-0.24}$	$0.64 \,^{+0.09}_{-0.20}$
Total background	$78.9 \pm 7.1 \,^{+13.3}_{-9.3}$	$9.46 \pm 1.1 \,^{+1.3}_{-2.4}$	$19.4 \pm 2.5 \,^{+5.2}_{-5.0}$
Data	59	5	23
Significance	-1.17	-1.27	0.48

Table 11.5: Total event yields for events with two SS leptons, two jets, $m_{lljj} < 400$ GeV and $|m_{jj} - 80| > 20$ GeV. Backgrounds contributing < 0.01 events in all three channels are omitted. The number of signal events shown assumes a coupling $|V_{lN}|^2$ equal to the expected limit in the case that no signal is observed.

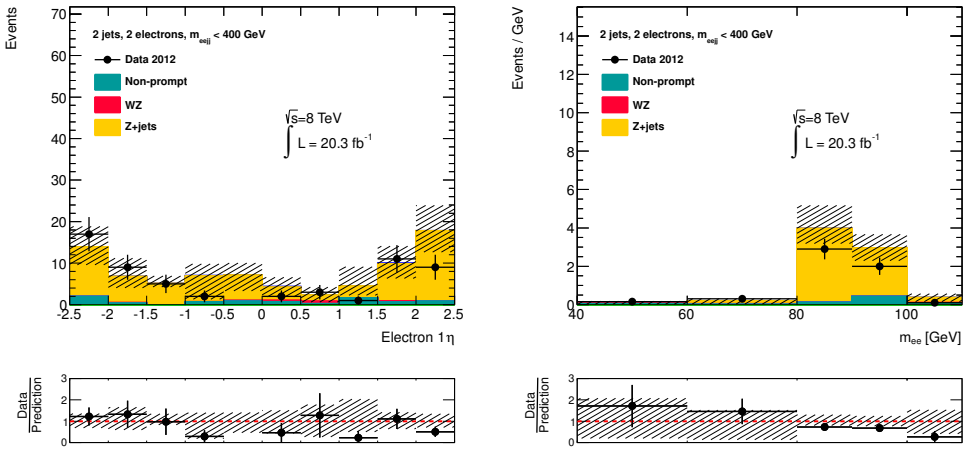

(a) $e^{\pm}e^{\pm}$

(b) $e^{\pm}e^{\pm}$

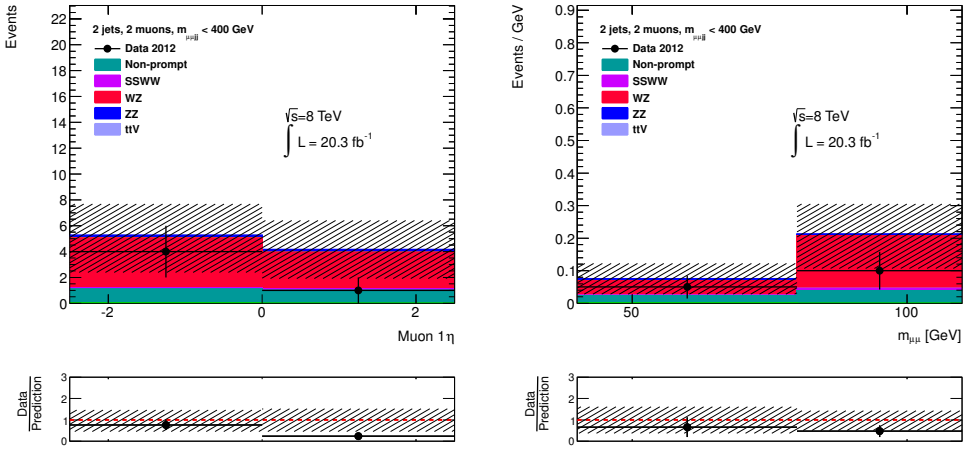

(c) $\mu^{\pm}\mu^{\pm}$

(d) $\mu^{\pm}\mu^{\pm}$

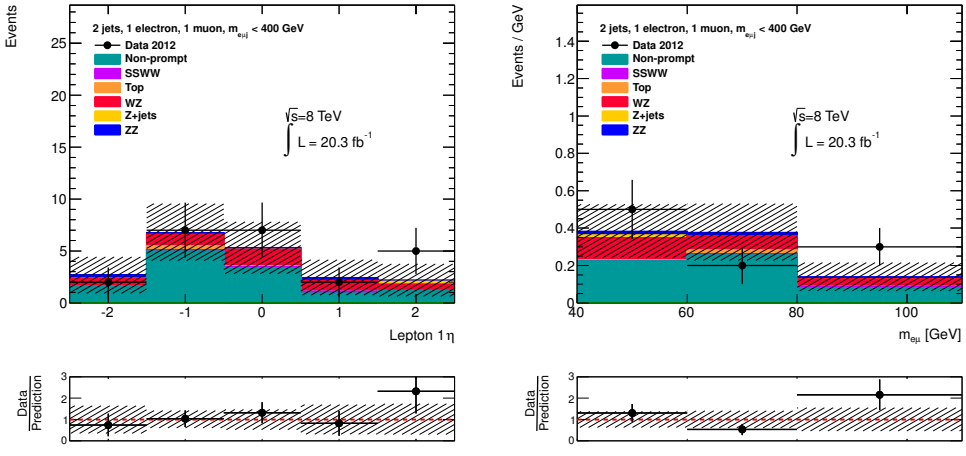

(e) $e^{\pm}\mu^{\pm}$

(f) $e^{\pm}\mu^{\pm}$

Figure 11.3: Leading lepton η distribution (left) and invariant mass of two leading leptons (right) for events with two SS leptons, two jets and $m_{lljj} < 400$ GeV (Control Region 3).

Source of uncertainty	Uncertainty on total background [%]		
	ee	$\mu\mu$	$e\mu$
Charge flip method	± 8.04	± 0.00	+ 0.65 / - 0.33
Electron ID	+ 1.94 / - 1.92	-	+ 0.39 / - 0.32
Electron Iso SF	+ 0.27 / - 0.29	-	+ 0.24 / - 0.04
Electron Reco	± 1.16	-	+ 0.28 / - 0.17
Electron Scale	+ 0.02 / - 0.00	-	+ 0.22 / - 0.00
Electron Smearing	+ 0.02 / - 0.58	-	+ 0.46 / - 0.00
Non-prompt	+ 5.24 / - 5.19	+ 8.03 / - 7.83	+ 25.8 / - 25.3
JER	± 1.17	± 9.37	± 2.49
JES	+ 0.13 / - 1.85	+ 2.13 / - 21.8	+ 0.86 / - 2.63
JVF	+ 13.4 / - 5.61	+ 8.8 / - 0.93	+ 6.15 / - 2.31
Luminosity	± 2.45	± 1.97	+ 0.79 / - 0.74
Muon ID	-	+ 0.00 / - 0.19	+ 0.44 / - 0.37
Muon Iso SF	-	+ 2.84 / - 2.78	+ 0.58 / - 0.53
Muon Reco	-	± 0.29	+ 0.24 / - 0.07
Muon Scale	-	+ 0.01 / - 0.00	+ 0.36 / - 0.37
Normalisation	± 0.21	± 6.81	± 2.85
Statistical	± 9.0	± 11.5	± 13.0
Total Uncertainty	+ 19.1 / - 14.8	+ 20.6 / - 28.6	+ 29.8 / - 28.9

Table 11.6: Uncertainty breakdown in events with two SS leptons, two jets, $m_{lljj} <$ 400 GeV and $|m_{jj} - 80| > 20$ GeV.

11.4 Control Region 4

As $\mu\mu$ events selected in this analysis may have fired the trigger `EF_mu18_tight_mu8_EFFS` (described in Section 5.3) there are events in this channel where the subleading muon satisfies $p_T \gtrsim 8$ GeV. This allows for Control Region 4 to be defined as containing two SS muons where the leading muon has $p_T > 25$ GeV and the second muon satisfies $10 < p_T$ [GeV] < 20. This region contains a high number of $\mu\mu$ events from non-prompt processes, although there is also a considerable contribution from diboson decays.

Kinematic distributions for this control region are presented in Figure 11.4, which show a good agreement in the shape of the distributions between predicted and observed events. The total predicted and observed number of data events are presented in Table 11.7. The significance S is measured to be -0.57 so the prediction is considered to be consistent with observation.

The dominant source of uncertainty in this control region is due to the non-prompt background which is approximately 25%.

Process	Event yields ± Stat. ± Syst.
	$\mu\mu$
Higgs	$0.38 \pm 0.01 \,^{+0.07}_{-0.07}$
Non-prompt	$1190 \pm 20 \,^{+390}_{-460}$
SSWW	$5.57 \pm 0.58 \,^{+2.8}_{-2.8}$
Top	$0.17 \pm 0.18 \,^{+0.01}_{-0.01}$
WZ	$327 \pm 6 \,^{+33}_{-33}$
ZZ	$56.7 \pm 2.1 \,^{+5.7}_{-5.7}$
ttV	$1.08 \pm 0.09 \,^{+0.33}_{-0.33}$
Signal MC $m_N = 120$ GeV	$0.91 \,^{+0.25}_{-0.24}$
Total background	$1580 \pm 21 \,^{+390}_{-470}$
Data	1315
Significance	-0.57

Table 11.7: Total event yields for events with two SS muons with the subleading muon p_T satisfying $10 < p_T$ [GeV] < 20. Backgrounds contributing < 0.01 events in all three channels are omitted. The number of signal events shown assumes a coupling $|V_{lN}|^2$ equal to the expected limit in the case that no signal is observed.

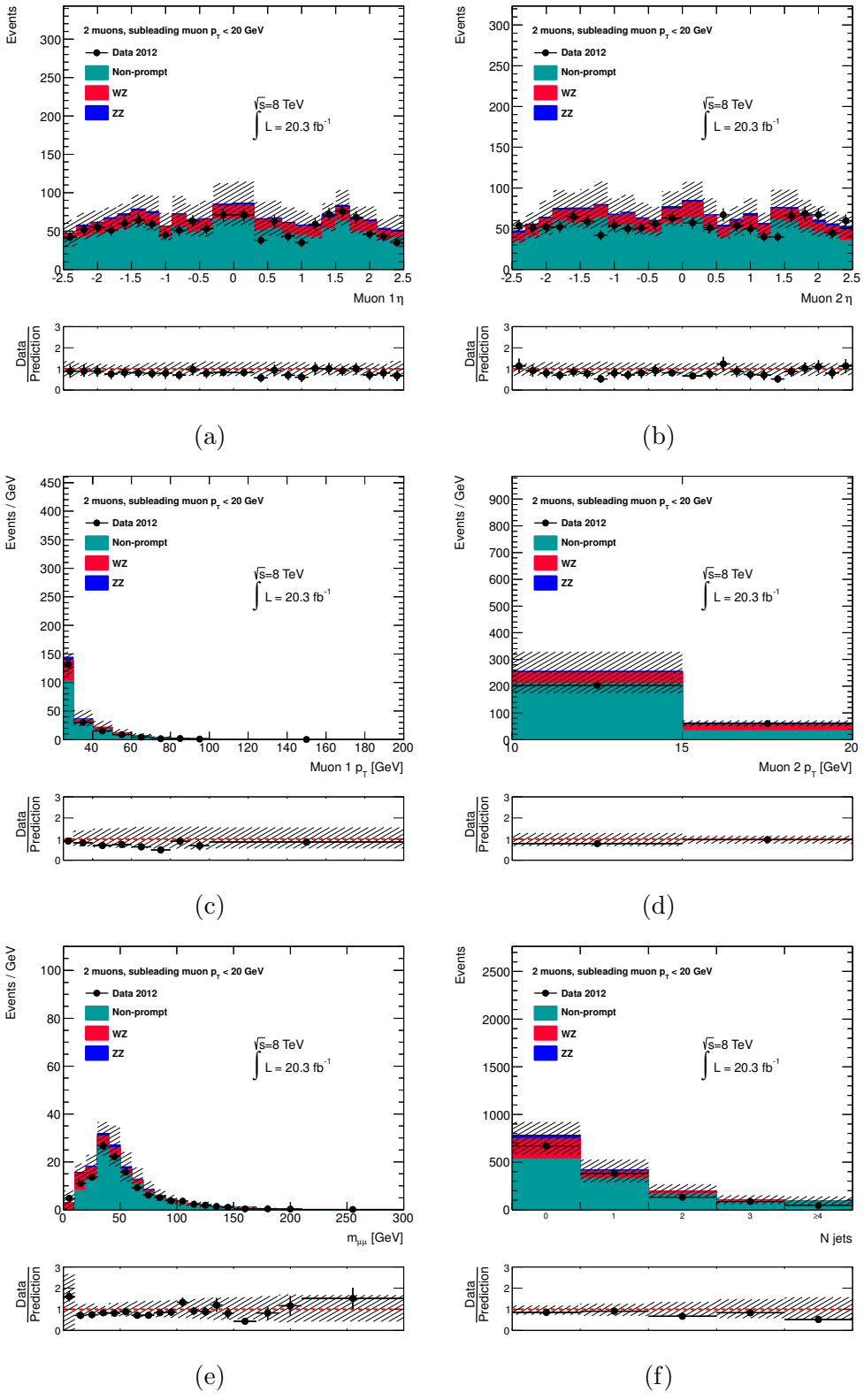

Figure 11.4: Kinematic distributions of events with two SS muons with the subleading muon p_T satisfying $10 < p_T$ [GeV] < 20 (Control Region 4).

Source of uncertainty	Uncertainty on total background [%]
Non-prompt	+ 24.4 / - 29.3
JER	± 0.04
JES	+ 0.18 / - 0.22
JVF	+ 0.26 / - 0.02
Luminosity	± 0.58
Muon ID	+ 0.00 / - 0.03
Muon Iso SF	+ 0.84 / - 0.83
Muon Reco	± 0.00
Muon Scale	+ 0.01 / - 0.04
Normalisation	± 1.83
Statistical	± 1.35
Total Uncertainty	+ 24.6 / - 29.4

Table 11.8: Uncertainty breakdown in events with two SS muons with the subleading muon p_T satisfying $10 < p_T$ [GeV] < 20.

11.5 Evaluation

The level of agreement between the predicted and observed yields and the kinematic distributions presented in Sections 11.1-11.4 is discussed here.

Control Regions 1-3 demonstrate that in the ee channel the charge-flip distribution is well modelled. In particular the electron η distribution has good agreement between data and prediction, and also the shape of the m_{ee} distribution is reproduced by the MC simulation. Furthermore the agreement is not significantly affected by the number of jets in the event.

The $\mu\mu$ and $e\mu$ channels in Control Regions 1-3 are most sensitive to the modelling of diboson and non-prompt backgrounds. The agreement in these channels is considered to be good. The kinematic distributions are well modelled and there is not any systematic dependancy on the number of jets in the event. For the $\mu\mu$ channel there is additionally Control Region 4 which predominantly probes the non-prompt muon estimate. This is also consistent within systematic uncertainties.

As there are no concerns with the predicted number of events in the control regions, it is considered that the background prediction in the signal region will be well modelled. The comparison of the background prediction with the data in the signal region is presented in Chapter 12.

Chapter 12

Results

This chapter presents the results of the search for heavy Majorana neutrino production in the signal region defined in Section 8.3. A discussion of the observed number of events and associated kinematics is given in Section 12.1 and subsequently the significance of the observed result is evaluated in Section 12.2.

12.1 Events in the signal region

ATLAS data is analysed to search for events in the signal region presented in Section 8.3. In this section, the number of observed events in data are compared to the expected number of background events with the intention of interpreting an excess of events in data in terms of a heavy Majorana neutrino decay in the interaction $pp \to N\ell^{\pm} \to \ell^{\pm}\ell^{\pm}jj$. Any excess of events is quantified in the framework discussed in Section 12.2.1.

The number of predicted and measured events as a function of subsequent selection criteria is presented in Table 12.1. For all stages of subsequent cuts in the ee, $\mu\mu$ and $e\mu$ channels, the measured number of events are within two standard deviations from the predicted number of background events. A comparison of kinematic distributions of the predicted background and of observed data events is presented in Figures 12.1, 12.2 and 12.3 for the ee, $\mu\mu$ and $e\mu$ channels respectively. The Figures 12.1a, 12.2a and 12.3a contain events which have at least two jets and exactly two SS leptons with a

		2 SS leptons	$m_{\ell\ell} > 40$ GeV	2 jets	$\lvert m_{ee} - m_Z \rvert >$ 20 GeV	$E_T^{\text{miss}} <$ 40 GeV	$\lvert m_{jj} - 80 \rvert <$ 20 GeV
ee	Data	4719	4618	639	155	82	19
	Prediction	$5234\ ^{+504}_{-500}$	5191^{+504}_{-500}	$661\ ^{+98.8}_{-94.6}$	$160^{+15.2}_{-13.3}$	$86.4^{+9.5}_{-10.2}$	$20.5^{+3.9}_{-6.0}$
	Significance	-1.01	-1.13	-0.21	-0.28	-0.32	-0.20
$\mu\mu$	Data	592	534	119	-	35	6
	Prediction	$558^{+52.6}_{-52.4}$	$507^{+48.2}_{-47.9}$	$125.7\ ^{+24.6}_{-23.2}$	-	$43.5\ ^{+9.1}_{-8.6}$	$8.7\ ^{+1.9}_{-2.0}$
	Significance	0.59	0.50	-0.25	-	-0.78	-0.83
$e\mu$	Data	1260	1098	347	-	132	25
	Prediction	1484^{+242}_{-228}	1357^{+238}_{-226}	$503^{+77.0}_{-71.3}$	-	$186^{+36.8}_{-35.2}$	$48.1^{+15.3}_{-15.1}$
	Significance	-0.92	-1.08	- 1.97	-	-1.40	-1.43

Table 12.1: The number of events predicted by background estimates and observed in data in the ee, $\mu\mu$ and $e\mu$ channels after subsequent criteria are fulfilled (from left to right). The number of data events in the signal region are indicated under the final column ('$|m_{jj} - 80| < 20$ GeV'). The $|m_{ee} - m_Z| > 20$ GeV criteria only applies to ee events. The presented uncertainty indicates the combined statistical and systematic uncertainty on the background prediction.

minimum dilepton mass $m_{\ell\ell} > 40$ GeV. Exclusively to events in the ee channel Figure 12.1b contains events in which the dilepton mass further satisfies $|m_{ee} - m_Z| > 20$ GeV. In addition to the former set of criteria, Figures 12.1c, 12.2b and 12.3b show events with $E_T^{\text{miss}} < 40$ GeV. The subsequent selection requirements, as described in Table 12.1, are indicated in each of these figures.

The dilepton mass distribution in Figure 12.1a shows that agreement between the data and prediction is good up to high values of m_{ee}. After requiring that $|m_{ee} - m_Z| > 20$ GeV, the E_T^{miss} distribution of ee events presented in Figure 12.1b shows good agreement between data and prediction. This includes the region where $E_T^{\text{miss}} < 40$ GeV, which is used in the signal region definition to suppress events from WZ decays. After applying this E_T^{miss} criteria in ee events, the mass distribution of the two p_T-leading jets is shown in Figure 12.1c to give good agreement between the measured data and background prediction up to high m_{jj}, but also values of m_{jj} close to m_W where the signal selection criteria is applied.

The E_T^{miss} distribution for SS $\mu\mu$ events is presented in Figure 12.2a and shows good agreement between data and the background prediction up to high E_T^{miss} and also in the region $E_T^{\text{miss}} < 40$ GeV. The m_{jj} distribution for the same events after applying the E_T^{miss} selection criteria is shown in Figure 12.2b which shows consistency between the observed data and prediction within systematic uncertainties.

An overprediction of the background is shown in the E_T^{miss} distribution of SS $e\mu$ events with at least two jets in Figure 12.3a, particularly in the region satisfying $40 < E_T^{\text{miss}}$ [GeV] < 60 where the local significance S, as defined in Chapter 11, is -2.13. As this level of deviation between the observed and predicted event yields is not observed across the E_T^{miss} spectrum it is concluded that this is tolerable. The m_{jj} distribution after requiring that the event satisfies $E_T^{\text{miss}} < 40$ GeV is shown in Figure 12.3b. The event yields and shape of the distribution are consistent within systematic uncertainties.

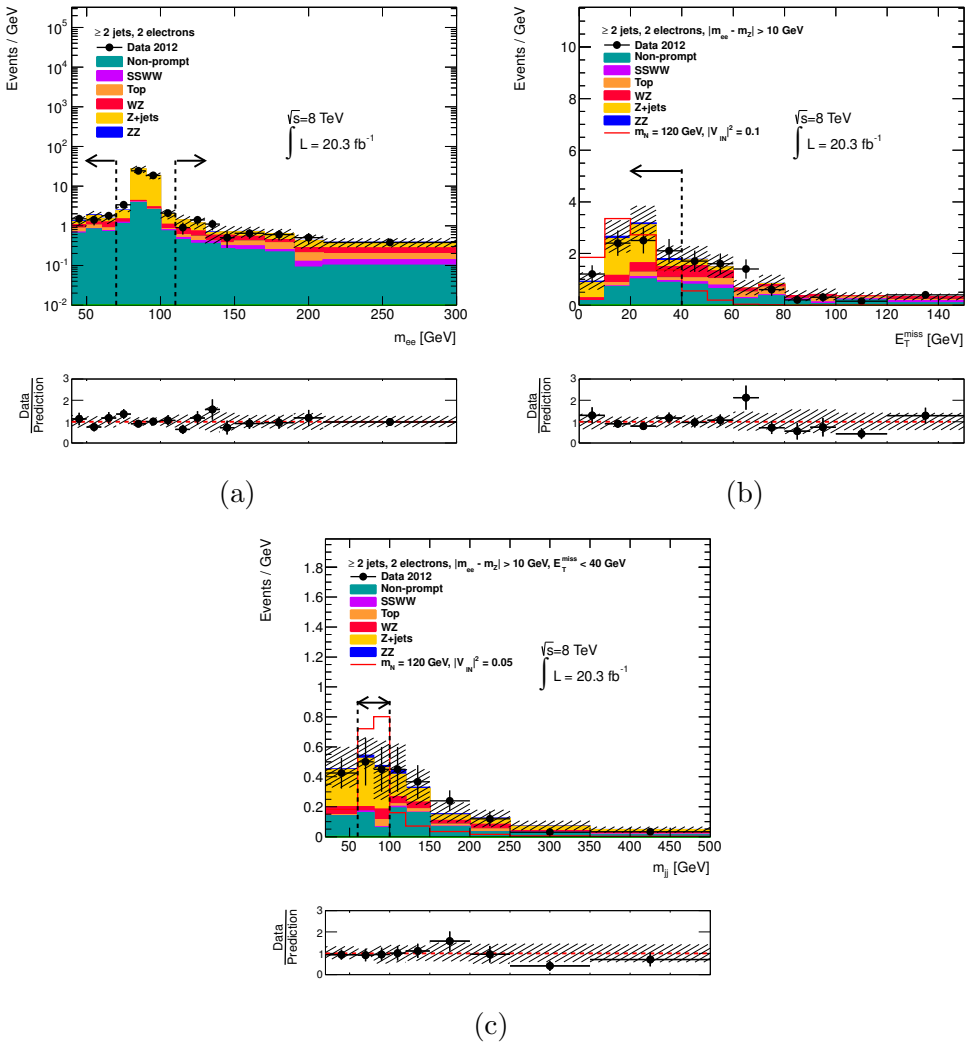

Figure 12.1: Kinematic distribution of SS ee events with at least two jets. Figure (a) shows the leading ee mass, (b) shows the E_T^{miss} distribution for events after requiring that $|m_{ee} - m_Z| > 20$ GeV and (c) shows the m_{jj} distribution for events which are further required to satisfy $E_T^{\text{miss}} < 40$ GeV. The regions indicated by the arrows are retained after the signal selection cuts are applied. The signal MC shown in figures (b) and (c) corresponds to a heavy neutrino mass of $m_N = 120$ GeV and lepton-neutrino couplings $|V_{lN}|^2 = 0.1$ and $|V_{lN}|^2 = 0.05$ respectively.

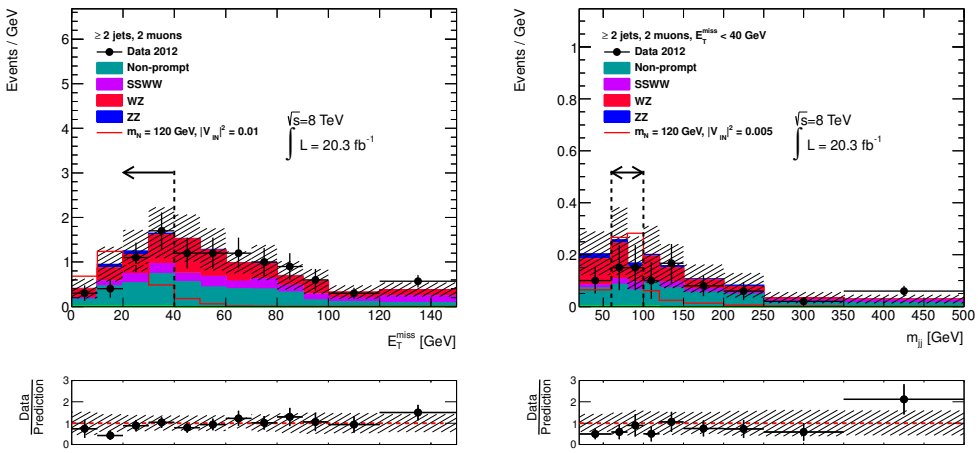

(a) (b)

Figure 12.2: Kinematic distribution of SS $\mu\mu$ events with at least two jets. Figure (a) shows the E_T^{miss} distribution and (b) shows the m_{jj} distribution for events which are required to satisfy $E_T^{\text{miss}} < 40$ GeV. The regions indicated by the arrows are retained after the signal selection cuts are applied. The signal MC shown in figures (a) and (b) corresponds to a heavy neutrino mass of $m_N = 120$ GeV and lepton-neutrino couplings $|V_{lN}|^2 = 0.01$ and $|V_{lN}|^2 = 0.005$ respectively.

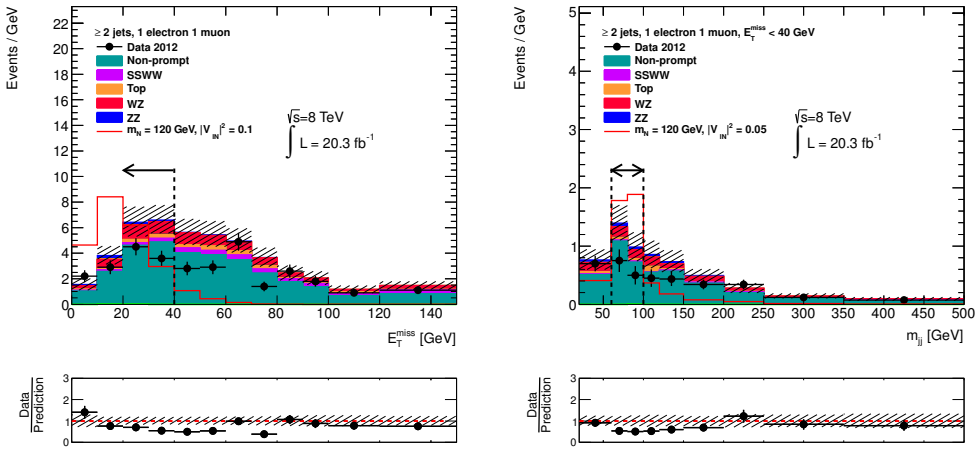

(a) (b)

Figure 12.3: Kinematic distribution of SS $e\mu$ events with at least two jets. Figure (a) shows the E_T^{miss} distribution and (b) shows the m_{jj} distribution for events which are required to satisfy $E_T^{\text{miss}} < 40$ GeV. The regions indicated by the arrows are retained after the signal selection cuts are applied. The signal MC shown in figures (a) and (b) corresponds to a heavy neutrino mass of $m_N = 120$ GeV and lepton-neutrino couplings $|V_{lN}|^2 = 0.1$ and $|V_{lN}|^2 = 0.05$ respectively.

A breakdown of the composition of the background in the signal region is presented in Table 12.2. In the ee channel the majority of the predicted background is attributed to Z+jets charge-flip events, in addition to contributions by non-prompt and diboson processes. The main contributions to the predicted background in the $\mu\mu$ signal region, which contains the fewest number of events compared to the ee and $e\mu$ channels, are from diboson, non-prompt and SS-WW decays. The predicted background in the $e\mu$ channel is dominated by non-prompt processes.

There is no excess of events observed in any of the three channels, so limits are set on the maximum allowed cross-section times branching-ratios and the heavy neutrino-lepton coupling $|V_{lN}|^2$ using the method discussed in Section 12.2.

Process	Event yields ± Stat. ± Syst.		
	ee	$\mu\mu$	$e\mu$
Higgs	$0.01 \pm 0.00\ ^{+0.00}_{-0.00}$	$0.01 \pm 0.00\ ^{+0.00}_{-0.00}$	$0.02 \pm 0.00\ ^{+0.00}_{-0.00}$
Non-prompt	$4.34 \pm 1.4\ ^{+1.2}_{-1.2}$	$2.93 \pm 0.63\ ^{+1.1}_{-1.1}$	$36.0 \pm 4.5\ ^{+14.5}_{-14.2}$
SSWW	$0.31 \pm 0.14\ ^{+0.19}_{-0.16}$	$1.05 \pm 0.25\ ^{+0.53}_{-0.6}$	$0.80 \pm 0.2\ ^{+0.45}_{-0.4}$
Top	$0.75 \pm 0.63\ ^{+0.62}_{-0.21}$	$0.00 \pm 0.00\ ^{+0.00}_{-0.00}$	$1.78 \pm 0.61\ ^{+1.4}_{-1.1}$
WW	$0.03 \pm 0.03\ ^{+0.06}_{-0.00}$	$0.00 \pm 0.00\ ^{+0.00}_{-0.00}$	$0.08 \pm 0.05\ ^{+0.01}_{-0.01}$
WZ	$2.18 \pm 0.5\ ^{+0.8}_{-0.4}$	$3.94 \pm 0.66\ ^{+0.98}_{-1.4}$	$6.57 \pm 0.82\ ^{+1.5}_{-1.8}$
Z+jets	$11.9 \pm 2.6\ ^{+2.1}_{-5.1}$	< 0.02	$0.00 \pm 0.00\ ^{+0.00}_{-0.00}$
ZZ	$0.80 \pm 0.23\ ^{+0.16}_{-0.25}$	$0.56 \pm 0.19\ ^{+0.24}_{-0.18}$	$2.35 \pm 0.42\ ^{+0.67}_{-0.78}$
ttV	$0.16 \pm 0.03\ ^{+0.05}_{-0.05}$	$0.19 \pm 0.04\ ^{+0.08}_{-0.07}$	$0.45 \pm 0.06\ ^{+0.14}_{-0.17}$
Total background	$20.5 \pm 3.1\ ^{+2.4}_{-5.1}$	$8.69 \pm 0.97\ ^{+1.6}_{-1.8}$	$48.1 \pm 4.6\ ^{+14.6}_{-14.4}$
Data	19	6	25
Significance	-0.20	-0.83	-1.43

Table 12.2: Total event yields for backgrounds in the signal region: 2 SS leptons, 2 jets and $|m_{jj} - 80| < 20$ GeV. Backgrounds contributing < 0.01 events in all three channels are omitted.

12.2 Limits on heavy neutrino production

A limit-setting procedure is required in which one can define the significance of an excess of events with respect to a background-only hypothesis and also be able to interpret the absence of a signal as a statistical limit on the allowed properties of the signal. The strategy for limit setting used in this analysis is presented in Section 12.2.1. The observed limits on heavy Majorana neutrino production, corresponding to the data discussed in Section 12.1, are presented in Section 12.2.2

12.2.1 Limit-setting procedure

It is convenient to introduce the limit-setting procedure in terms of a simple counting experiment in which the number of events n are Poisson distributed with an expectation value $E[n]$ which can be written in terms of the number of expected signal and background events. For a given signal process with cross-section σ, event selection efficiency ϵ in a dataset with integrated luminosity L_{int}, the number of predicted signal events s_0 is given by:

$$s_0 = \epsilon\sigma L_{\text{int}}. \tag{12.1}$$

Hence $E[n]$ can be written in terms of s_0 and the number of expected background events b_0 as:

$$E[n] = \mu s_0 + b_0 \tag{12.2}$$

where μ is a measure of the 'signal strength' which is to be determined. It should be noted that the effect of μ is to scale the cross-section of the signal. The distribution of n, which is broadened by systematic uncertainties, can be described by the likelihood function L:

$$L(\mu, \theta) = \frac{(\mu s + b)^n \, e^{-(\mu s+b)}}{n!} \prod_j \frac{1}{\sqrt{2\pi}} e^{-\frac{\theta_j^2}{2}} \tag{12.3}$$

where θ are nuisance parameters corresponding to the systematic uncertainties. The value of b is related to θ and the nominal expected background b_0

according to:

$$b = b_0 \prod_i (1 + S_b(\theta_i)) \tag{12.4}$$

where $S_b(\theta_i)$ is the fractional effect of systematic uncertainty i on the background and $S_b(\theta_i = 1)$ corresponds to one standard deviation. Similarly s is related to θ by:

$$s = s_0 \prod_i (1 + S_s(\theta_i)) \tag{12.5}$$

where s_0 the nominal signal expected from cross-section σ.

Prior to an experiment a hypothesis can be formulated which predicts the background to occur but no signal ($\mu = 0$) and a second hypothesis can be formulated which predicts both the signal and background to occur ($\mu > 0$). The test statistic $\tilde{q}_\mu$ is defined to discriminate between the background-only and signal-plus-background scenarios in terms of the Profile Likelihood Ratio (PLR) $\lambda(\mu)$ [101]:

$$\begin{aligned} \tilde{q}_\mu &= -2\ln(\lambda(\mu)) \\ \lambda(\mu) &= \frac{L(\mu, \hat{\hat{\theta}}(\mu))}{L(\hat{\mu}, \hat{\theta}(\mu))} \end{aligned} \tag{12.6}$$

where $\hat{\hat{\theta}}$ are the values of θ that maximise L for a given μ, and $\hat{\mu}$ and $\hat{\theta}$ maximise L given all permitted values of μ and θ. Importantly it is high values of $\tilde{q}$ that correspond to increased incompatibility between the observed result and μ.

In the fit to maximise L, $\hat{\mu}$ will be allowed to float to any value including $\hat{\mu} < 0$. In order to obtain a sensible result in this scenario the PLR is defined such that the denominator in Equation 12.6 is evaluated at $\hat{\mu} = 0$. Furthermore for $\hat{\mu} > \mu$ the test statistic offers no rejection power so $\tilde{q}$ should be defined as zero in this scenario. The test statistic $\tilde{q}$ is therefore replaced by q, which is a redefinition of $\tilde{q}$ for the following values of $\hat{\mu}$:

$$q_\mu = \begin{cases} \frac{L(\mu, \hat{\hat{\theta}}(\mu))}{L(0, \hat{\hat{\theta}}(0))} & \hat{\mu} < 0 \\ \frac{L(\mu, \hat{\hat{\theta}}(\mu))}{L(\hat{\mu}, \hat{\theta})} & 0 \leq \hat{\mu} \leq \mu \\ 0 & \hat{\mu} > \mu \end{cases} . \tag{12.7}$$

The probability of obtaining either the observed result, $q_\mu^{\rm obs}$, or a more extreme result for a given value of μ is quantified by the p-value, which is given by:

$$p_\mu = \int_{q_\mu^{\rm obs}}^{\infty} f(q_\mu|\mu) dq_\mu \tag{12.8}$$

where $f(q_\mu|\mu)$ is the Probability Density Function (pdf) of the test statistic. With a signal and background prediction it is possible to evaluate the pdf for any value of μ. Confidence Levels CL_b and CL_{s+b} are defined in terms of the p-value for the background-only hypothesis p_b and signal-plus-background hypothesis p_{s+b} respectively:

$$CL_{s+b} \equiv p_{s+b}$$
$$CL_b \equiv 1 - p_b$$

where p_b and p_{s+b} are defined as:

$$p_{s+b} = \int_{q_\mu^{\rm obs}}^{\infty} f(q_\mu|\mu \neq 0) dq_\mu$$
$$p_b = \int_{-\infty}^{q_{\mu=0}^{\rm obs}} f(q_\mu|\mu = 0) dq_{\mu=0}.$$

Values of CL_b very close to 1 indicate poor compatibility with the background-only hypothesis, favouring the signal-plus-background hypothesis. Similarly small values of CL_{s+b} indicate poor compatibility with the signal-plus-background hypothesis. The significance of an observed signal can be quantified in terms of $(1 - CL_b)$, which represents a statistical deviation from the background-only hypothesis.

One can infer the significance of observing CL_b in terms of the Gaussian standard deviation σ. It is widely accepted in the particle-physics community that CL_b values corresponding to three σ may be used to claim evidence of a new phenomena and five σ may be used to claim a discovery. This would require probabilities for observation and discovery of $CL_b = 2.7 \times 10^{-3}$ and $CL_b = 5.7 \times 10^{-7}$ respectively for observing the result if the background-only hypothesis was correct.

If no significant excess is observed over the background prediction then exclusion limits can be set with respect to values of μ at a Confidence Level of $(1-\beta)$, such that a value of μ is found to reject the signal-plus-background hypothesis if $CL_{s+b} \leq \beta$. In order to protect against the situation where the expected number of background events exceeds the observed number of events the CL_s method is used where:

$$CL_s = \frac{CL_{s+b}}{CL_b}. \tag{12.9}$$

Although CL_s does not represent a true probability, limits are set in the same manner as with CL_{s+b}. The effect of CL_b on CL_s is a reduction in the significance (when compared with CL_{s+b}) when the background and signal distributions become indistinguishable. For this reason the CL_s method is adopted by ATLAS and will also be used in this thesis.

12.2.2 Observed limits

Limits are set by counting all events observed in data and expected from background predictions after applying all the event selection cuts described in Section 8.3.

An 'expected limit', which is the limit one would expect to measure if the background hypothesis was correct, can be set without prior knowledge of the observed number of events in data. In practice this is performed by substituting the observed number of data for the predicted background. The observed and expected CL_s limits on the cross-section-times-branching for heavy Majorana neutrino production in the signal region described in Section 8.3 are shown in this section as a function of the heavy neutrino mass.

As there is no excess of events observed for any of the ee, $\mu\mu$ or $e\mu$ final states, a limit on the cross-section times branching-ratio $\{\sigma \times \mathrm{Br}\}^{\mathrm{limit}}$ is set for a given m_N in each channel using the CL_s procedure described in Section 12.2.1. In this method $\{\sigma \times \mathrm{Br}\}^{\mathrm{limit}}$ is interpreted as the signal strength by using the number of events observed in the signal region presented in Section

12.1 and the measured values of signal efficiency for a given m_N presented in Figure 8.4 in Section 8.3. All systematic uncertainties defined in Chapter 10 are included in the limit calculation. Each systematic uncertainty is assumed to be correlated between the different background sources but uncorrelated from each other source of systematic uncertainty.

The observed and expected CL_s limits on the cross-section times branching-ratio, $\{\sigma \times \mathrm{Br}\}^{\mathrm{limit}}_{\mathrm{obs}}$ and $\{\sigma \times \mathrm{Br}\}^{\mathrm{limit}}_{\mathrm{exp}}$, are shown in Figure 12.4, where the yellow and green bands indicate the expected spread of results corresponding to one and two standard deviations respectively. The limit improves for m_N in the range $100 \rightarrow 120$ GeV, and subsequently varies slowly for $m_N > 140$ GeV which directly reflects the shape of the signal acceptance distributions presented in Section 8.3. In the ee channel $\{\sigma \times \mathrm{Br}\}^{\mathrm{limit}}_{\mathrm{obs}}$ and $\{\sigma \times \mathrm{Br}\}^{\mathrm{limit}}_{\mathrm{exp}}$ match closely as the number of observed events is highly consistent with the predicted number of events. The measured limits $\{\sigma \times \mathrm{Br}\}^{\mathrm{limit}}_{\mathrm{obs}}$ in the $\mu\mu$ and $e\mu$ channels are stronger than the corresponding values of $\{\sigma \times \mathrm{Br}\}^{\mathrm{limit}}_{\mathrm{exp}}$ as there are fewer observed events than predicted events. The observed limits are however consistent with the expected limit within two standard deviations.

The theoretical cross-section depends on $|V_{Nl}|^2$ and m_N, as described in Section 3.5. It is used to interpret $\{\sigma \times \mathrm{Br}\}^{\mathrm{limit}}_{\mathrm{obs}}$as a limit on $|V_{lN}|^2$ as a function of m_N. The procedure to interpret the limit on $|V_{lN}|^2$ assumes only the lightest of the heavy neutrinos contributes to the cross-section and that the masses of the other heavy neutrino species are sufficiently high so that the effect of interference is negligible. The interpreted limit on $|V_{lN}|^2$ is shown in Figure 12.5. The limit increases in strength for m_N in the range $100 \rightarrow 120$ GeV due the increase in signal acceptance. The limit subsequently decreases for $m_N > 120$ GeV due a smaller cross-section as a function of m_N.

The limits in the $e\mu$ and $\mu\mu$ channels are comparatively stronger than the ee channel as the signal acceptance is higher, specifically at low m_N. The limits in the $\mu\mu$ search channel are stronger than in the $e\mu$ channel as the number of background processes to the final state is comparatively low. In all three channels the presented limits are the strongest direct limits set to date for $m_N > 100$ GeV. In the $\mu\mu$ channel the limits are approximately a factor of

four stronger than the same limits measured by ATLAS with pp collisions at 7 TeV in 2011 [30]. This reflects the relative size of the larger dataset collected in 2012, despite the increased pile-up conditions. Furthermore these limits are approximately by a factor of ten stronger than the limits set by the CMS collaboration in 2011 [29]. The presented limits in the ee channel are the first such measurements for ATLAS and are a factor of five stronger than the limits set by CMS in 2011. If one considers only the electron-type heavy neutrino, the presented limits are comparatively weaker by a factor of approximately 10^4 than indirect limits set from searches for neutrinoless double beta decay. The limit produced in the $e\mu$ channel is the first such measurement by an LHC experiment.

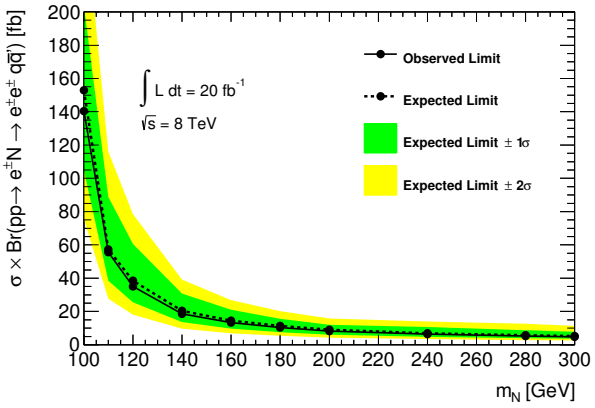

(a)

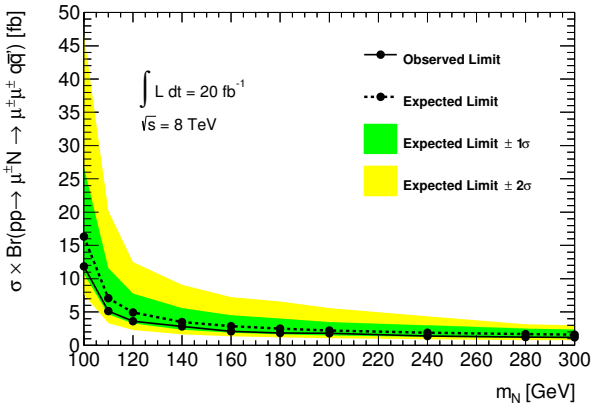

(b)

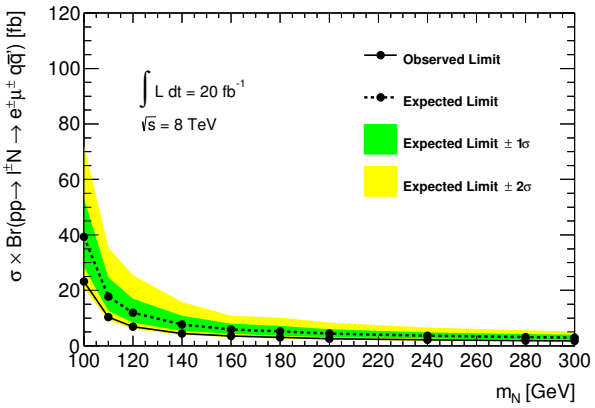

(c)

Figure 12.4: Observed and expected 95% confidence level limits on the cross section times branching ratio for the production of heavy Majorana neutrinos as a function of the heavy neutrino mass for (a) the ee channel, (b) the $\mu\mu$ channel and (c) the $e\mu$ channel.

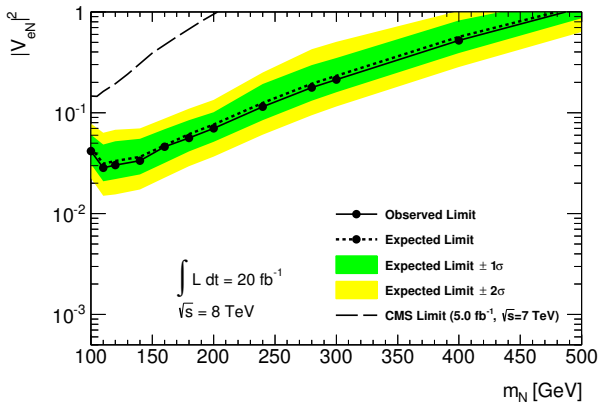

(a)

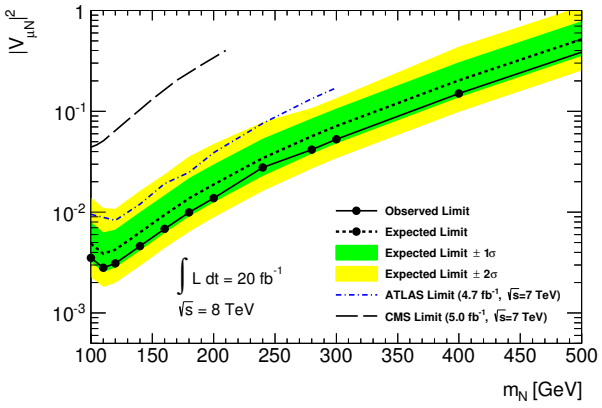

(b)

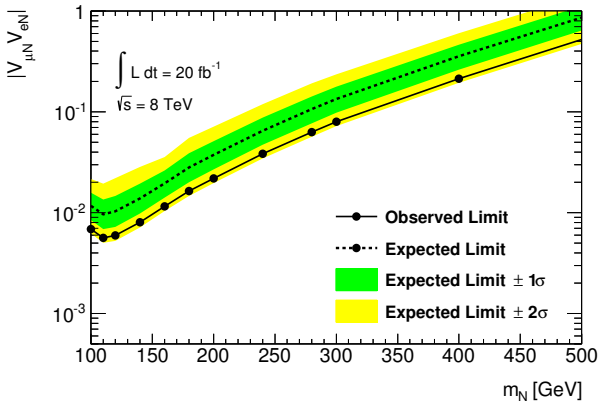

(c)

Figure 12.5: Observed and expected 95% confidence level limits on the $N - l$ coupling $|V_{Nl}|^2$ as a function of the heavy neutrino mass for (a) the ee channel, (b) the $\mu\mu$ channel and (c) the $e\mu$ channel. The procedure to extract $|V_{Nl}|^2$ from the limit of the cross section time branching ratio (Figure 12.4) assumes that only the lightest of the heavy neutrinos contributes to the cross-section and that the masses of the other heavy neutrino species are sufficiently high so that the effect of interference is negligible.

Chapter 13

Conclusion

A search has been performed for heavy Majorana neutrinos produced in $\sqrt{s} = 8$ TeV proton-proton collisions in the ATLAS detector at the CERN Large Hadron Collider, with data corresponding to an integrated luminosity of 20.3 fb^{-1}. The search is motivated by the discovery of small non-zero neutrino masses, which introduces a new mass-scale to the Standard Model which is at least six orders of magnitude below the electron mass. In the absence of a Standard Model mechanism to explain this new mass scale, one can consider the possibility that neutrinos are Majorana-type fermions. In this scenario neutrinos can acquire large Majorana-mass terms in addition to the Standard Model mass terms. The resulting mass eigenstates are sufficient to explain the mass-scale of the Standard Model neutrinos by introducing heavy neutrino states which could be produced in high energy collisions.

This thesis has presented a search for the process $pp \to W^* \to \ell N \to \ell\ell q\bar{q}$, where N is a heavy Majorana neutrino. Heavy neutrinos are considered in this analysis with a mass in the range 100 GeV to 500 GeV. Collision events collected with the ATLAS detector have been selected which contain at least two jets and one pair of leptons from ee, $\mu\mu$ and $e\mu$. The two leptons are only selected if they have the same-sign electric charge, which is permitted due to the Majorana nature of the heavy neutrino. The highest-p_T lepton is required to satisfy $p_T > 25$ GeV and the second lepton and two jets must satisfy $p_T > 20$ GeV. The W boson which is produced from the decay of the heavy neutrino is on-shell, and therefore the two p_T-leading jets are required

to have an invariant mass within 20 GeV of the W boson mass.

Additional cuts are applied to events in order to maximise signal efficiency with respect to the background. Diboson decays are suppressed by rejecting events with greater than two loosely defined lepton objects, as opposed to the two tightly defined leptons required in the analysis. The invariant mass of the lepton pair is required to be greater than 40 GeV in order to reject low mass QCD resonances from the signal region. There are no sources of E_T^{miss} from the phenomenology of the heavy neutrino decay, so the E_T^{miss} in signal events is required to be less than 40 GeV. In the ee channel, Z+jets events are suppressed by requiring that the invariant mass of electron pairs satisfy $|m_{ee} - m_Z| < 20$ GeV where m_Z is the Z boson mass.

The main sources of background in the $\mu\mu$ and $e\mu$ channels signal regions are from diboson decays and non-prompt leptons. The predicted number of events due to non-prompt leptons is calculated using a data-driven approach which assigns an event weight to pairs of leptons according to whether each lepton has passed a nominal or looser quality criteria. In the ee channel the most significant contribution to the observed background is from 'charge-flip' events, in which the charge of one lepton from a pair of leptons with opposite-sign electric charge has been incorrectly assigned. The charge-flip rate is calculated by assessing the likelihood of electron pairs from $Z \to ee$ data events to contain a charge-flip given an underlying dependency on electron η. The predicted number of events from all other backgrounds is taken from MC simulation which has been corrected to account for measured resolutions and selection efficiencies. The total diboson background prediction, which is taken from MC simulation, is controlled by isolating events containing exactly three or four leptons. The main sources of uncertainty in the background prediction are from measurements of the charge-flip and non-prompt backgrounds, and measurements of the jet energy scale.

There is no excess of events observed over the expected background. Limits have been set on the cross-section times branching-ratio and the lepton-heavy neutrino coupling as a function of the heavy neutrino mass m_N. The observed limits are consistent with a background-only hypothesis within two

Gaussian standard deviations. The strongest limits have been set in the $\mu\mu$ channel due to a relatively high signal acceptance and low number of background processes in the signal region. In this channel a 95% Confidence Level upper limit of approximately 20 fb is set on the cross-section times branching-ratio for muon-type heavy neutrinos with mass $m_N = 100$ GeV, and < 1 fb for $m_N > 300$ GeV. The observed limits in all three channels are the most stringent set to date for $m_N > 100$ GeV in a direct search for heavy Majorana neutrinos.

List of acronyms

ALICE A Large Ion Collider Experiment

ATLAS A Toroidal LHC ApparatuS

BCM Beam Conditions Monitor

BSM Beyond the Standard Model

CERN European Organisation for Nuclear Research

CKM Cabibbo-Kobayashi-Maskawa

CL Confidence Level

CMS Compact Muon Solenoid

CP Cluster Processor

CSCs Cathode Strip Chambers

CTEQ Coordinated Theoretical-Experimental project on QCD for the determination of parton distribution functions

CTP Central Trigger Processor

DSID Dataset Identification

ECal EM Calorimeter

EF Event Filter

EM Electromagnetic

EW Electroweak

FCal Forward Calorimeter

GUT Grand Unified Theory

HCal Hadronic Calorimeter

HEC Hadronic Endcap Calorimeter

HLT High Level Trigger

I_3 isospin

ID Inner Detector

IP Interaction Point

JEP Jet Energy-sum Processor

JER Jet Energy Resolution

JES Jet Energy Scale

JVF Jet Vertex Fraction

L1 Level 1

L2 Level 2

LAr Liquid Argon

LEP Large Electron Positron Collider

LINAC2 Linear Accelerator 2

LHC Large Hadron Collider

LHCb Large Hadron Collider Beauty

LO Leading Order

LRSM Left-Right Symmetric Model

LUCID LUminosity measurement using a Cherenkov Integrating Detector

LUT Look-Up-Table

MC Monte Carlo

MCP Muon Combined Performance group

MDTs Monitored Drift Tubes

MS Muon Spectrometer

NLO Next-to-Leading Order

NNLO Next-to-Next-to-Leading Order

OS opposite-sign

pdf Probability Density Function

PDF Parton Distribution Function

PLR Profile Likelihood Ratio

PMNS Pontecorvo-Maki-Nakagawa-Sakata

PS Proton Synchrotron

PSB Proton Synchrotron Booster

QCD Quantum Chromodynamics

QFT Quantum Field Theory

RF Radio Frequency

RoIs Regions of Interest

RPCs Resistive Plate Chambers

SCT Semi-Conductor Tracker

SM Standard Model of particle physics

SPS Super Proton Synchrotron

SS same-sign

TDAQ Trigger and Data Aquisition

TGCs Thin Gap Chambers

TRT Transition Radiation Tracker

References

[1] Super-Kamiokande Collaboration, Y. Fukuda *et al.*, *Evidence for oscillation of atmospheric neutrinos*, Phys. Rev. Lett. **81**, 1562 (1998).

[2] SNO Collaboration, B. Aharmim *et al.*, *Electron energy spectra, fluxes, and day-night asymmetries of ^8B solar neutrinos from measurements with NaCl dissolved in the heavy-water detector at the Sudbury Neutrino Observatory*, Phys. Rev. C **72**, 055502 (2005).

[3] M. E. Peskin and D. V. Schroeder, *An Introduction to Quantum Field Theory* (Westview Press, 1995).

[4] S. Weinberg, *A Model of Leptons*, Phys. Rev. Lett. **19**, 1264 (1967).

[5] P. Watkins, *Discovery of the W and Z bosons*, Contemp. Phys. **27**, 291 (1986).

[6] N. Cabibbo, *Unitary Symmetry and Leptonic Decays*, Phys. Rev. Lett. **10**, 531 (1963).

[7] M. Kobayashi and T. Maskawa, *CP-Violation in the Renormalizable Theory of Weak Interaction*, Progress of Theoretical Physics **49**, 652 (1973).

[8] Z. Maki, M. Nakagawa, and S. Sakata, *Remarks on the Unified Model of Elementary Particles*, Progress of Theoretical Physics **28**, 870 (1962).

[9] R. P. Feynman, *The Theory of Positrons*, Phys. Rev. **76**, 749 (1949).

[10] Particle Data Group, J. Beringer *et al.*, *Review of Particle Physics*, Phys. Rev. D **86**, 010001 (2012).

[11] H. Murayama, *Neutrino mass eigenstates*, `http://hitoshi.berkeley.edu/neutrino/`, 2013.

[12] J. Pumplin *et al.*, *New generation of parton distributions with uncertainties from global QCD analysis*, JHEP **0207**, 012 (2002).

[13] P. M. Nadolsky *et al.*, *Implications of CTEQ global analysis for collider observables*, Phys. Rev. D **78**, 013004 (2008).

[14] A.D. Martin, R.G. Roberts, W.J. Stirling, R.S. Thorne, *Uncertainties of predictions from parton distributions. I: experimental errors*, Eur. Phys. J **C28**, 455 (2003).

[15] A. Martin, W. Stirling, R. Thorne, and G. Watt, *Update of parton distributions at NNLO*, Physics Letters B **652**, 292 (2007).

[16] P. Fileviez Pérez, T. Han, and T. Li, *Testability of the type I seesaw mechanism at the CERN LHC: Revealing the existence of the $B - L$ symmetry*, Phys. Rev. D **80**, 073015 (2009).

[17] E. Papageorgiu, *Neutrino properties from maximally-predictive GUT models and the structure of the heavy Majorana sector*, Zeitschrift für Physik C Particles and Fields **65**, 135 (1995).

[18] A. Pilaftsis, *Radiatively induced neutrino masses and large Higgs neutrino couplings in the standard model with Majorana fields*, Z. Phys. **C55**, 275 (1992).

[19] A. Atre, T. Han, S. Pascoli, and B. Zhang, *The Search for Heavy Majorana Neutrinos*, JHEP **0905**, 030 (2009).

[20] J. C. Pati and A. Salam, *Lepton Number as the Fourth Color*, Phys. Rev. **D10**, 275 (1974).

[21] R. N. Mohapatra, *Unification and Supersymmetry, ISBN 0-387-95534-8*, 3rd ed. (Springer-Verlag, 2002).

[22] R. N. Mohapatra and P. B. Pal, *Massive Neutrinos in Physics and Astrophysics, ISBN 981-238-070-1*, 3rd ed. (World Scientific, 2004).

[23] R. N. Mohapatra and G. Senjanovic, *Neutrino Mass and Spontaneous Parity Violation*, Phys. Rev. Lett. **44**, 912 (1980).

[24] R. Shrock, *New Tests For, and Bounds On, Neutrino Masses and Lepton Mixing*, Phys. Lett. **B96**, 159 (1980).

[25] F. del Aguila, J. de Blas, and M. Pérez-Victoria, *Effects of new leptons in electroweak precision data*, Phys. Rev. D **78**, 013010 (2008).

[26] A. Atre, T. Han, S. Pascoli, and B. Zhang, *The search for heavy Majorana neutrinos*, JHEP **2009**, 030 (2009).

[27] P. Beneš, A. Faessler, S. Kovalenko, and F. Šimkovic, *Sterile neutrinos in neutrinoless double beta decay*, Phys. Rev. D **71**, 077901 (2005).

[28] The ATLAS Collaboration, *Search for heavy neutrinos and right-handed W bosons in events with two leptons and jets in pp collisions at* $\sqrt{s} = 7$ TeV *with the ATLAS detector*, The European Physical Journal C **72**, 1 (2012).

[29] CMS Collaboration, S. Chatrchyan *et al.*, *Search for heavy Majorana neutrinos in* $\mu^+\mu^+[\mu^-\mu^-]$ *and* $e^+e^+[e^-e^-]$ *events in pp collisions at* $\sqrt{s} = 7$ *TeV*, Phys. Lett. **B717**, 109 (2012).

[30] The ATLAS Collaboration, *Search for Majorana neutrino production in pp collisions at* $\sqrt{s} = 7$ *TeV in dimuon final states with the ATLAS detector*, CERN, ATLAS-CONF-2012-139, 2012.

[31] O. Bruning *et al.*, *LHC design report. Vol. I: The LHC main ring*, (2004), CERN-2004-003-V-1.

[32] O. Bruning *et al.*, *LHC design report. Vol. II: The LHC Infrastructure and General Services*, (2004), CERN-2004-003-V-2.

[33] M. Benedikt *et al.*, *LHC design report. Vol. III: The LHC Injector Chain*, (2004), CERN-2004-003-V-3.

[34] The LEP Collaboration, *LEP design report* (CERN, Geneva, 1984).

[35] The ALICE Collaboration, *The ALICE detector at the LHC*, Nucl. Instrum. Meth **A344**, 27 (1994).

[36] The LHCb Collaboration, *LHCb: Technical proposal*, (1998), CERN-LHCC-98-004.

[37] The CMS Collaboration, *CMS physics: Technical design report.*, (2006), CERN-LHCC-2006-001.

[38] J. A. V. Ferrer, *Higgs discovery potential with the ATLAS detector at the LHC*, Journal of Physics: Conference Series **171**, 012026 (2009).

[39] The Tevatron Collaboration, *Design report Tevatron 1 project*, (1984), FERMILAB-DESIGN-1984-01.

[40] The ATLAS Collaboration, *ATLAS Luminosity Public Results*, `https://twiki.cern.ch/twiki/bin/view/AtlasPublic/LuminosityPublicResults`, 2012.

[41] The ATLAS Collaboration, *Observation of a new particle in the search for the Standard Model Higgs boson with the ATLAS detector at the LHC*, Phys. Lett. **B716**, 1 (2012).

[42] The ATLAS Collaboration, *The ATLAS Experiment at the CERN Large Hadron Collider*, Journal of Instrumentation **3**, S08003 (2008).

[43] B. A. Petersen, *The ATLAS Trigger Performance and Evolution*, CERN, ATL-DAQ-PROC-2012-071, 2012.

[44] The ATLAS Collaboration, *ATLAS detector and physics performance: Technical Design Report 1,* (CERN, Geneva, 1999), CERN-LHCC-99-014.

[45] The ATLAS Collaboration, P. Miele and H. H. J. ten Kate, *The Superconducting Magnet System for the ATLAS Detector at CERN*, Fusion Eng. Des. **58-59**, 195 (2001).

[46] The ATLAS Collaboration, *Performance of the ATLAS Inner Detector Track and Vertex Reconstruction in the High Pile-Up LHC Environment*, CERN, ATLAS-CONF-2012-042, 2012.

[47] The ATLAS Collaboration, N. Wermes and G. Hallewel, *ATLAS pixel detector: Technical Design Report,* (CERN, Geneva, 1998), CERN-LHCC-98-013.

[48] The ATLAS Collaboration, *The silicon microstrip sensors of the ATLAS semiconductor tracker*, Nuclear Instruments and Methods in Physics Research Section A: Accelerators, Spectrometers, Detectors and Associated Equipment **578**, 98 (2007).

[49] The ATLAS Collaboration, *ATLAS calorimeter performance Technical Design Report*, (1996), CERN-LHCC-96-40.

[50] ATLAS Collaboration, *Improved Luminosity Determination in pp Collisions at $\sqrt{s} = 7$ TeV using the ATLAS Detector at the LHC*, (2012), ATLAS-CONF-2012-080, ATLAS-COM-CONF-2012-086.

[51] S. van der Meer, *Calibration of the effective beam height in the ISR*, CERN, CERN-ISR-PO-68-31. ISR-PO-68-31, 1968.

[52] C. Bernius, *The ATLAS trigger menu: Design, performance and monitoring*, in *Nuclear Science Symposium and Medical Imaging Conference (NSS/MIC), 2012 IEEE*, pp. 1382–1385, 2012.

[53] The ATLAS Collaboration, *Performance of the ATLAS Electron and Photon Trigger in p-p Collisions at $\sqrt{s} = 7$ TeV in 2011*, (2012), ATLAS-CONF-2012-048.

[54] M. H. Seymour and M. Marx, *Monte Carlo Event Generators*, MCNET-13-05 (2013).

[55] S. Agostinelli *et al.*, *Geant4 - a simulation toolkit*, Nuclear Instruments and Methods in Physics Research Section A: Accelerators, Spectrometers, Detectors and Associated Equipment **506**, 250 (2003).

[56] The ATLAS Collaboration, D. Costanzo *et al.*, *ATLAS detector simulation*, (2005), CERN-ATL-SOFT-PUB-2005-004.

[57] T. Sjstrand, S. Mrenna, and P. Skands, *A brief introduction to `PYTHIA` 8.1*, Computer Physics Communications **178**, 852 (2008).

[58] The ATLAS Collaboration, E. Richter-Was, D. Froidevaux, and L. Poggioli, *ATLFAST 2.0 a fast simulation package for ATLAS*, CERN, ATL-PHYS-98-131, 1998.

[59] F. del Aguila, J. A. Aguilar-Saavedra, and R. Pittau, *Heavy neutrino signals at large hadron colliders*, JHEP **2007**, 047 (2007).

[60] M. L. Mangano, F. Piccinini, A. D. Polosa, M. Moretti, and R. Pittau, *ALPGEN, a generator for hard multiparton processes in hadronic collisions*, JHEP **2003**, 001 (2003).

[61] F. del Aguila, J. Aguilar-Saavedra, and R. Pittau, *Neutrino physics at large colliders*, Journal of Physics: Conference Series **53**, 506 (2006).

[62] M. Bhr *et al.*, *Herwig++ physics and manual*, The European Physical Journal C **58**, 639 (2008).

[63] T. Gleisberg *et al.*, *Event generation with SHERPA 1.1*, JHEP **2009**, 007 (2009).

[64] S. Frixione and B. R. Webber, *The MC@NLO 2.0 event generator*, (2003), CAVENDISH-HEP-03-09, CERN-TH-2003-159, GEF-TH-7-2003.

[65] S. Frixione and B. R. Webber, *Matching NLO QCD computations and parton shower simulations*, JHEP **2002**, 029 (2002).

[66] The ATLAS Collaboration, *Studies to detemine the cross-section uncertainty for SS-WW production at ATLAS*, `https://twiki.cern.ch/twiki/bin/viewauth/AtlasProtected/WWjjMC12Validation#Cross_Section`, 2013.

[67] F. Maltoni and T. Stelzer, *MadEvent: automatic event generation with MadGraph*, JHEP **2003**, 027 (2003).

[68] T. Stelzer and W. Long, *Automatic generation of tree level helicity amplitudes*, Computer Physics Communications **81**, 357 (1994).

[69] P. Skands and S. Weinzierl, *Some remarks on dipole showers and the DGLAP equation*, Phys. Rev. D **79**, 074021 (2009).

[70] J. Pequenao and P. Schaffner, *A computer generated image representing how ATLAS detects particles*, CERN-EX-1301009, 2013.

[71] The ATLAS Collaboration, T. Cornelissen *et al.*, *Concepts, Design and Implementation of the ATLAS New Tracking (NEWT)*, CERN, ATL-SOFT-PUB-2007-007, ATL-COM-SOFT-2007-002, 2007.

[72] The ATLAS Collaboration, *Performance of primary vertex reconstruction in proton-proton collisions at* $\sqrt{s}$ *=7 TeV in the ATLAS experiment*, CERN, ATLAS-CONF-2010-069, 2010.

[73] The ATLAS Collaboration, *Track reconstruction in the ATLAS Muon Spectrometer with MOORE 007*, CERN, ATL-SOFT-2003-007, 2003.

[74] The ATLAS Collaboration, S. Hassani *et al.*, *A muon identification and combined reconstruction procedure for the ATLAS detector at the LHC using the (MUONBOY, STACO, MuTag) reconstruction packages*, Nuclear Instruments and Methods in Physics Research Section A: Accelerators, Spectrometers, Detectors and Associated Equipment **572**, 77 (2007), Frontier Detectors for Frontier Physics.

[75] The ATLAS Collaboration, R. Nicolaidou *et al.*, *Muon identification procedure for the ATLAS detector at the LHC using Muonboy reconstruction package and tests of its performance using cosmic rays and single beam data*, Journal of Physics: Conference Series **219**, 032052 (2010).

[76] The ATLAS Collaboration, *Defining the quality criteria for STACO muons at ATLAS*, `https://twiki.cern.ch/twiki/bin/viewauth/AtlasProtected/QualityDefinitionStaco`, 2013.

[77] The ATLAS Collaboration, *ATLAS Muon Combined Performance Guidelines*, `https://twiki.cern.ch/twiki/bin/viewauth/AtlasProtected/MCPAnalysisGuidelinesData2012`, 2012.

[78] W. Lampl *et al.*, *Calorimeter Clustering Algorithms: Description and Performance*, CERN, ATL-LARG-PUB-2008-002. ATL-COM-LARG-2008-003, 2008.

[79] The ATLAS Collaboration, *Electron and photon reconstruction and identification in ATLAS: expected performance at high energy and results at 900 GeV*, CERN, ATLAS-CONF-2010-005, 2010.

[80] The ATLAS Collaboration, *Definitions for the ATLAS electron plusplus menu*, `https://twiki.cern.ch/twiki/bin/viewauth/AtlasProtected/TechnicalitiesForMedium1`, 2013.

[81] M. Cacciari, G. P. Salam, and G. Soyez, *The anti-k_T jet clustering algorithm*, JHEP **2008**, 063 (2008).

[82] G. Salam, *Towards jetography*, The European Physical Journal C **67**, 637 (2010).

[83] The ATLAS Collaboration, D. W. Miller, A. Schwartzman, and D. Su, *Pile-up jet energy scale corrections using the jet-vertex fraction method*, CERN, ATL-PHYS-INT-2009-090, 2009.

[84] The ATLAS Collaboration, *Study of jets produced in association with a W boson in pp collisions at $\sqrt{s} = 7$ TeV with the ATLAS detector*, Phys. Rev. D **85**, 092002 (2012).

[85] The ATLAS Collaboration, *Pile-up subtraction and suppression for jets in ATLAS*, CERN, ATLAS-CONF-2013-083, 2013.

[86] The ATLAS Collaboration, J. Backus Mayes, C. Gwilliam, D. W. Miller, A. Schwartzman, and G. Zevi Della Porta, *Performance plots on the impact of pile-up on reconstructed jets and correction methods.*, CERN, ATL-COM-PHYS-2011-1639, 2011.

[87] The ATLAS Collaboration, *Performance of missing transverse momentum reconstruction in proton-proton collisions at $\sqrt{s} = 7$ TeV with ATLAS*, The European Physical Journal C **72**, 1 (2012).

[88] The ATLAS Collaboration, *Egamma Performance Group*, `https://twiki.cern.ch/twiki/bin/view/AtlasProtected/EfficiencyMeasurements`, 2013.

[89] The ATLAS Collaboration, *Preliminary results on the muon reconstruction efficiency, momentum resolution, and momentum scale in ATLAS 2012 pp collision data*, (2013), ATLAS-CONF-2013-088.

[90] The ATLAS Collaboration, *Electron performance measurements with the ATLAS detector using the 2010 LHC proton-proton collision data*, Eur. Phys. J. C **72**, 1909. 45 p (2011).

[91] The ATLAS Collaboration, *ATLAS Muon Combined Performance Trigger Guidelines*, `https://twiki.cern.ch/twiki/bin/viewauth/Atlas/MuonTriggerPhysicsTriggerRecommendations2011`, 2011.

[92] The ATLAS Collaboration, *Search for heavy Majorana neutrinos and WR/ZR gauge bosons in events with two same-sign leptons and jets in pp collisions at $\sqrt{s}$ = 8 TeV with the ATLAS detector.*, (2014), ATL-COM-PHYS-2013-810.

[93] Heinemeyer *et al.*, *Handbook of LHC Higgs Cross Sections: 3. Higgs Properties*, (2013), arXiv:1307.1347. CERN-2013-004, https://twiki.cern.ch/twiki/bin/view/LHCPhysics/CrossSections.

[94] A. Denner, S. Heinemeyer, I. Puljak, D. Rebuzzi, and M. Spira, *Standard model Higgs-boson branching ratios with uncertainties*, The European Physical Journal C **71**, 1 (2011).

[95] J. M. Campbell, R. K. Ellis, and C. Williams, *Vector boson pair production at the LHC*, JHEP **2011**, 1 (2011).

[96] M. Garzelli, A. Kardos, C. Papadopoulos, and Z. Trocsanyi, *$t\,\bar{\mathrm{t}}W^{\pm} + t\bar{\mathrm{t}}Z$ hadroproduction at NLO accuracy in QCD with Parton Shower and Hadronization effects*, JHEP **2012**, 1 (2012).

[97] The ATLAS Collaboration, *Studies to detemine the cross-section uncertainty for ttV production at ATLAS*, `https://twiki.cern.ch/twiki/bin/viewauth/AtlasProtected/SUSYSystematicUncertainties2012#Ttbar_EW`, 2013.

[98] The ATLAS Collaboration, *Studies to detemine the cross-section uncertainty for Higgs production at ATLAS*, `https://twiki.cern.ch/twiki/bin/viewauth/AtlasProtected/HiggsCrossSection#Higgs_Cross_Section_Uncertainty`, 2013.

[99] The ATLAS Collaboration, *Measurement of the b-tag Efficiency in a Sample of Jets Containing Muons with 5 fb^{-1} of Data from the ATLAS Detector*, (2012), ATLAS-CONF-2012-043.

[100] The ATLAS Collaboration, *Improved luminosity determination in pp collisions at $\sqrt{s} = 7$ TeV using the ATLAS detector at the LHC*, (2013).

[101] G. Cowan, K. Cranmer, E. Gross, and O. Vitells, *Asymptotic formulae for likelihood-based tests of new physics*, The European Physical Journal C **71**, 1 (2011).